The Influence of Instabilities on the Electron Dynamics of a Magnetic Nozzle

by

Shadrach T. Hepner

A dissertation submitted in partial fulfillment
of the requirements for the degree of
Doctor of Philosophy
(Aerospace Engineering)
in The University of Michigan
2022

Doctoral Committee:

Assistant Professor Benjamin A. Jorns, Chair
Professor John E. Foster
Professor Alec D. Gallimore
Dr. James Gilland, Glenn Research Center

Shadrach Hepner

shadrach@umich.edu

ORCID iD: 0000-0003-2727-8734

To my family.

Acknowledgements

No work truly stands on its own, and no research is made possible without the support of others. I would like to start by expressing my gratitude for Benjamin Jorns. Your advising has taught me what it means to do research and to ask the questions. I will take your first-principles mindset, your willingness to ask the tough questions, and your enjoyment of Kubb with me wherever I go. I would also like to thank James Gilland for the excellent mentorship through the NSTRF program. While I know NASA has certain expectations of a mentor, it was never in doubt that you would go beyond any of them. I have appreciated our biweekly chats, both when they pertain to important research questions and when we end up killing an hour talking about whatever else. I would further like to thank Dean Alec Gallimore and Prof. John Foster. Without Alec's initiative, none of us would be graduating from this lab. Your influence in the lab has never ceased, even after becoming the dean, and after the transition you have led this university through some hectic years with tact and pose. And Prof. Foster, I am not only grateful for the research conversations we have had, but for the devotion you showed when teaching us in your classes, even after they had gone virtual.

On the financial side, this work was primarily funded under a NASA Space Technology Research Fellowship, grant number 80NSSC17K0156. It was also partially funded by a Michigan Plasma Science and Engineering fellowship.

I would next like to thank all of my labmates who supported me through the years. Each and every one of you have taught me so many lessons over the last years

that I could fill a book, but I'll keep this as short as I can. For those of you I was able to work with, it has been an absolute pleasure. Ben and Tim, thank you for teaching me what I know about radiofrequency thrusters in my first years. Marcel and Sarah, it was a pleasure to get to know you both and learn from you both personally and professionally. I will always look forward to the next time we get beers, and I will always leave a good review for your AirBnB. Scott and Ethan, as the eternal "upper years" the two of you set the tone for what it meant to be a student here, and opened the doors kindly to us all as we entered. It is frankly a shock that the lab continued running after you left.

To the group of students who joined at the same time as me, Ben Wachs, Zach Brown, Josh Woods, and Matt Byrne. The four of you have been here since the beginning, and I am proud to be able to walk out of here at (roughly) the same time as you all. We have studied for prelims in the cage, stayed up until daylight writing papers (and watching stupid movies), gone out on the town– the list of priceless memories goes on. Needless to say, you have all seen me through a lot, and for that I will always be grateful. I truly hope I get the opportunity to work with each of you again.

And to the newer students as well. Leanne my eternal Vienna co-tourist, Chris my favorite bartender/Sanderson fan, Tate who woke up and chose violence (but we wouldn't have it any other way), Thomas the best saber-er that I know, Collin who somehow still feels older than me, Parker who will always be faster than me, and Sophia who I hope will never stop sending me memes. And Madison and Will, while I wish I could have spent more time with you both, I know enough to be confident that the lab will be in good hands for at least a few more years. I would also like to acknowledge Pete and Angela, both of whom, while only here for a few years, left an unmistakable mark on the lab as well.

These last few years have been... different. Covid-19 has impacted each of us in many different ways. We have watched the world progress from crisis to crisis on what feels like a weekly basis, but through it all a certain group of people have been there more than any other– my quarantine bubble, my roommates at 418 High: Allie, Annie, Ben (again), Tojo, Mia, and Sheeba. I feel like if you shove six people into a house together during a pandemic, they either come out of it hating each other or closer than ever. I can honestly say that the six of you were the absolute best people I could have asked for. While we bickered at times, I would not have traded that house for the world. I also owe a special thanks to Sheeba, who has been the most supportive partner that I could have asked for through an extremely stressful final year of this program.

I of course owe more thanks to my family than I could possibly do justice. You have all been there for me in so many different ways beyond just my years here. I can confidently say that, without your unending support, I would not be where I am today. Mom, words cannot express how proud of you I am. Seeing you redefine your beliefs over the past few years and stick to them even when people have shut you down as a result has been nothing short of incredible. Dad, you have always been there when I have needed someone to talk to. You were made to be a father, and I am glad I am no longer the only one who gets to experience that. Darren, while we did not start off on the best of terms, I can not think of many other people in the world who I have as much respect for as I do for you nowadays. Pupay, you have not only provided me with the world's best Thai food, but you have been excited to make sure that I always had a home and a bed whenever I come back. And, of course, Skylar. You have never known me outside of being a grad student, but I imagine you also haven't thought about it much at this point. You have the entire world ahead of you. I cherish each time I get to see you now, and I cannot wait to see the person you become.

I could drag this on for a hundred pages, but instead I will further extend one large thank you to all of my friends in Ann Arbor and around the country who have made me smile so much over these years. The SPH group (and those affiliated), my TTRPG friends, all of my other excellent roommates, the language meetups, and the so-called ”Responders.“ You have all been there for me when I needed you most (whether you necessarily knew it or not), and I would not have been able to make it here without your support.

Table of Contents

CHAPTER

List of Figures

Figure

Nomenclature

Functions and Operators

$\mathcal{F}$	Fourier transform.
C	Collision operator.
I	Modified Bessel function.
Z	Plasma dispersion function.

Physical constants

ϵ_0	Permittivity of free space.
e	Charge magnitude of an electron.

Modifiers

$< x >$	Phase average of property x
$\overline{x}$	Average quantity.
$\tilde{x}$	Oscillating component of property x.

Properties (Roman)

$\mathbf{a}$	Acceleration vector.
$\mathbf{B}$	Magnetic field vector.
$\mathbf{E}$	Electric field vector.
$\mathbf{j}$	Volumetric current
$\mathbf{k}$	Wavevector.
$\mathbf{R}_s$	Resistivity of species s.
$\mathbf{u}$	Fluid velocity.
$\mathbf{v}$	Velocity vector.

$\mathbf{x}$	Position vector.
$\mathcal{E}$	Adjusted energy of a Langmuir probe trace.
A	Magnetic nozzle area.
A_p	Probe surface area.
A_w	Area of the back wall.
c_s	Acoustic speed.
dV	Differential volume element.
f	Distribution function.
F_j	Force induced on the magnets by plasma currnts.
F_w	Force on the back wall.
I	Pixel intensity.
$I_{i,sat}$	Ion saturation current.
L	Length of discharge region.
m	Azimuthal mode.
m_s	Mass of species s
N	Number of oscillations between probes.
n_s	Number density of species s.
P	Power.
p_s	Pressure of species s.
p_s	Pressure of species s
Q_s	Heat flux of species s.
q_s	Charge of species s.
r_L	Larmor radius.
r_p	Probe radius
T	Thrust.
t	Time.
T_s	Temperature of species s.

u_B	Bohm speed.
V_B	Bias voltage.
v_D	Diamagnetic drift velocity.
v_E	$\mathbf{E} \times \mathbf{B}$ drift velocity.
$v_{th,s}$	Thermal velocity of species s.
W	Thermal energy.

Properties (Greek)

χ_s	Susceptibility of species s.
γ	Polytropic index.
λ_D	Debye length.
ν_s	Collision frequency of species s.
ω	Angular frequency.
Ω_s	Hall parameter of species s
$\Omega_{c,s}$	Gyration frequency of species s.
ϕ	Plasma potential.
ψ	Magnetic streamfunction.
ξ	Ionization rate coefficient.

ABSTRACT

The impact of instabilities on electron dynamics in a magnetic nozzle thruster is investigated. The dispersion of a primarily azimuthal mode is measured experimentally using time-resolved measurements of ion saturation current. Simultaneous measurements from multiple probes are compared using a cross-correlation technique to measure wave presence as a function of frequency and wave vector. This mode is identified as a lower hybrid drift instability with finite Larmor radius effects and field-aligned propagation. Quasi-linear theory is invoked to estimate the effective collision frequency connected to the enhanced resistivity between electrons and ions mediated by the wave. A corresponding Hall parameter is found and compared to the same value predicted by Coulomb collisions. The wave-driven effect is found to be orders of magnitude more significant, and is determined to induce a divergence loss in the thruster efficiency. The effective, field-aligned collision frequency is then found based on an assumption of continuity of the electrons and energy exchange between the plasma potential and ion population. It is used in a Fourier law to estimate its impact on inhibiting downstream heat flux. It is found to impede heat flux to an extent several orders of magnitude higher than the classical prediction. A resulting prediction for the polytropic index is developed based on a quasi-one dimensional electron energy equation. The progression of the predicted heat flux is found to predict a polytropic index based on this theory comparable to what is measured. The enhanced impedance to heat flux generated by the wave is determined to have a further deleterious effect on thruster operation. Finally, high speed imagery is taken to measure the presence of a coherent mode upstream. Two separate modes are found.

A global mode is observed at low flow rates and considered to be an ionization mode. An azimuthal mode is observed ubiquitously that decreases in frequency as the flow rate increases. This mode is determined to be an anti-drift mode driven unstable by either parallel electric field and pressure gradient or field-aligned collisions. This mode is discussed in terms of its potential impact on particle losses to the walls in the ionization region. Primary findings are summarized, and a series of experiments are outlined for future work.

CHAPTER I

Introduction

1.1 Introduction

In this section, we first introduce magnetic nozzles and discuss their operating principles and benefits in space propulsion. After discussing the magnetic nozzles that have been or are currently under development, we introduce three open research questions: The direction of azimuthal current and its relation to thrust generation, cross-field momentum transport, and downstream heat transport. We then discuss the potential influence that the onset of instabilities might have on each of these questions and possible modes that might be present. We then present previous research investigating instabilities in these systems. Finally, we outline the major goals of the current work, which involve identifying instabilities in a magnetic nozzle plasma and investigating their significance in plume expansion.

1.2 Magnetic nozzle overview

In this section, we present an overview of the magnetic nozzle. We first explain the fundamental physics of their operation and the mechanics of thermodynamic expansion. We then discuss their advantages as applied to space propulsion. We conclude this section by describing some of the many magnetic nozzles that have

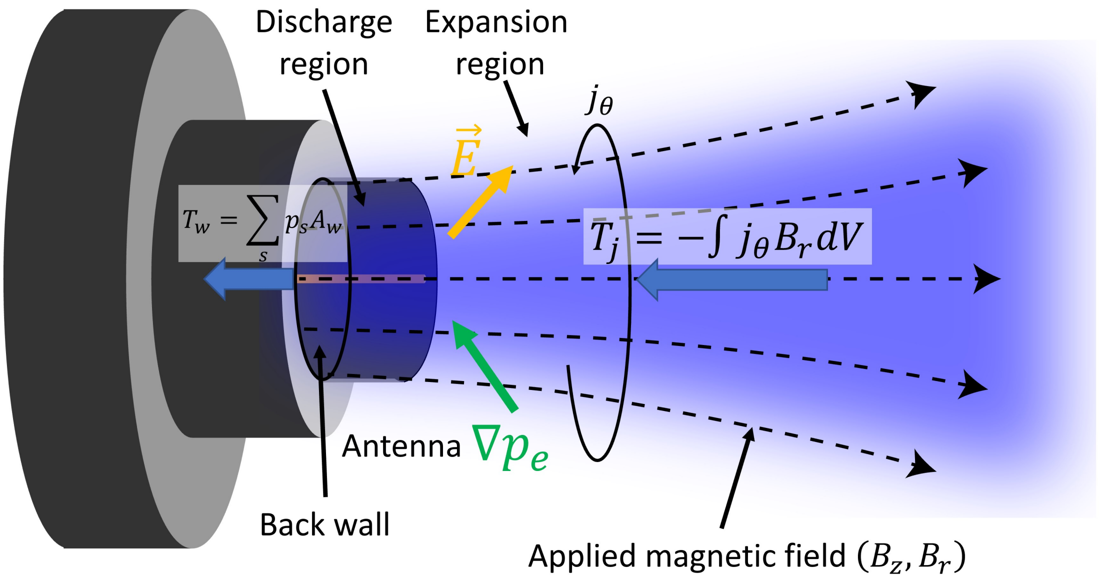

Figure 1.1: A typical magnetic nozzle geometry including the ionization and expansion regions labeled. Typical electric field and pressure gradient illustrated with nominal azimuthal current.

been designed, tested, and operated in space.

1.2.1 Principle of Operation

Fundamentally, a magnetic nozzle consists of a diverging magnetic field applied to a plasma to generate thrust (Fig. 1.1) by converting thermal energy into kinetic energy. These devices can typically be divided into two primary regions: the discharge region and the expansion region. In the discharge region, a plasma is generated in an applied magnetic field. Typically, these plasma sources are generated by radiofrequency [16] or microwave [120] antennas, but may implement a variety of ionization mechanisms. As the plasma is generated, it may induce force on the thruster by direct collisions with the back wall. This process is similar to that used by a conventional, neutral gas nozzle and can be simply described by the pressure integrated over the back wall area,

$$F_w = \sum_s p_s A_w \tag{1.1}$$

where p_s is the pressure of species s and A_w is the area of the back wall. While this interaction between the propellant and the wall continues downstream in a neutral gas nozzle, magnetic nozzles typically do not have walls in the expansion region. However, the expanding magnetic field enables a second interaction between the plasma and the thruster. This interaction arises from a volumetric Lorentz force between the applied magnet and the plasma, which is given by

$$\mathbf{F_j} = \mathbf{j} \times \mathbf{B}, \tag{1.2}$$

where $\mathbf{j}$ is the current density and $\mathbf{B}$ is the magnetic field. A magnetic nozzle thus also produces thrust by generating currents that interact with the magnetic field. The currents in the plasma arise primarily from the cross-field gradients in plasma pressure and potential. These gradients generate fluid forces on the plasma that induce azimuthal motion. This azimuthal current in turn interacts with the applied field via an axial force. As a result, the magnetic field must consist of a finite radial component to generate thrust. Figure 1.1 outlines these mechanisms for thrust generation.

1.2.2 Advantages of magnetic nozzles

There are several key aspects to magnetic nozzle operation that make them strong candidates for a variety of applications. First, their geometries imply a long potential lifetime. The magnetic field geometry may be designed such that the magnetic field is parallel to most thruster surfaces. Excepting the back wall, this feature implies that the particle flux to the wall, and thus the erosion rate, is small compared to other electric thrusters. As a result, magnetic nozzles are ideal for long-duration missions.

Moreover, these thrusters have the potential to operate on a variety of readily-available propellants inaccessible to other systems. The primary reason for this is the lack of plasma-wetted surfaces. Contrary to Hall effect or gridded ion thrusters, which rely on current-conducting surfaces to generate a plasma, the wave-based ionization typically present in a magnetic nozzle does not require direct contact between an electrode and the plasma to provide energy. As an example, one potential resource for this operation is water. While ionizing water typically results in a high quantity of oxygen that corrodes electrodes, wave-based magnetic nozzles may be designed to have no such surfaces. Water is not only abundant on earth, but may further be used in the future for missions requiring in-flight refueling. In conjunction with the lack of surface erosion, mid-mission refueling may be a crucial enabler for long duration missions.

Finally, when the applied magnetic field can be formed by permanent magnets, magnetic nozzles only require a single power supply. This fact implies a low footprint on a rocket and a simplicity of operation not universal among electric propulsion devices. This simplicity implies a low footprint on a spacecraft, which enables their use on smaller satellites.

Magnetic nozzles are thus ideal candidates for a wide array of space propulsion missions. Currently, a wide array of these devices are under development. In the following section, we provide an overview of several design.

1.2.3 Contemporary development

Contemporary interest in radiofrequency magnetic nozzles originates in the ability of similar sources to generate a high density plasma [27], which is theoretically beneficial for thrust production. Modern examples of research devices include the Chi Kung thruster [16], the Helicon Double Layer Thruster [74, 124], and the high power helicon [125].

One further example of a radiofrequency thruster is the VASIMR VX-200SS [80], currently being developed by Ad Astra. This thruster is being designed to operate at a power level of 200 kW in steady state operation. It operates by generating a plasma using a helicon source, then further heating the plasma using an ion cyclotron resonance scheme. The resulting hot plasma is exhausted through an expanding field. Ideally, VASIMR will be able to generate 5 N at 200 kW– however, the most recent steady-state tests have been at 80 kW, which maintained operation for 88 hours [2].

On the other end of the power spectrum, several radiofrequency magnetic nozzles have recently been developed and launched at low powers. The first is the Maxwell Block 1 from Phase 4, which was first launched in January of 2021 [41]. The Block 1 has been measured in ground testing to produce a thrust of 7 mN at 500 W while operating on xenon. Moreover, T4i recently launched Regulus, which is reported to operate at a nominal 50 W at a specific impulse of 550 s and .55 mN thrust. Moreover, this thruster fits into 1.5U of a cubesat. These thrusters prove the applicability of magnetic nozzles to small satellite propulsion.

However, despite their contemporary implementation in space systems, radiofrequency thrusters typically operate at relatively low efficiencies. 100 W class thrusters generally maintain $< 10\%$ total efficiency [28, 101, 25], and research is ongoing to improve this value [109]. One potential reason for this low value is the typically low electron temperatures ($\lesssim 10$ eV) present in these plasmas [69]. While radiofrequency antennas can produce high density plasmas, the electrothermal nature of these thrusters implies that acceleration depends on the thermal energy [69]. A potential way to improve magnetic nozzles over this design thus may be to increase the electron temperature.

One possible mechanism for increasing the electron temperature is implementation of electron cyclotron resonance (ECR) sources to generate plasmas for magnetic nozzles. These plasma sources have been used for over 50 years [66, 88] in expanding plasmas. ECR sources apply an electric field that oscillates with the electron gyrofrequency. In applying such a resonant field, the antenna is able to deposit energy into an individual electron continuously as it orbits, drastically increasing its temperature. Modern ECR thrusters are able to achieve electron temperatures over 30 eV [31]. Recently, interest in this type of thruster has increased significantly, largely driven by progress in development of MINOTOR at ONERA. This thruster applies microwave power to a copper antenna mounted concentrically with the thruster discharge region. It typically runs on xenon propellant, which it ionizes by resonant electron heating at a magnetic field strength of 865 Gauss. Their most recent published results indicate that they are able to operate the thruster at an operating efficiency of 16% at a 30 W condition [93], although a recent presentation claims up to 50%, a value which has historically only been found in kW-class devices. Given the promising recent results in ECR plasma development, we choose this technology for our investigation into magnetic nozzle physics.

While development of thrusters based on these geometries have progressed significantly, the physics of their operation is an area of ongoing research. The interaction of the plasma with the applied field proves complex, and decades of research have gone into attempting to understand it. In the following sections, we elaborate on two of these: cross-field transport and field-aligned heat conduction.

1.3 Open research topics

Due to their wide potential application in space propulsion, magnetic nozzles are the subject of extensive, ongoing research. Three research areas of particular note to the current work are thrust generation, cross-field transport, and heat conduction.

1.3.1 Thrust generation

We have previously shown that magnetic nozzles generate thrust at least in part by downstream interactions between an applied magnetic field and azimuthal currents. However, the direction and magnitude of these currents are not completely understood. Given Eqn. 1.2, if the net current in the plume changes sign, the imparted force will invert, and the plasma will be pulled back towards the thruster. An understanding of these currents is vital to predicting how the thruster will perform.

In this case, **j** is predominantly determined by the cross-field gradients in plasma pressure and electric field. The effective particle velocity induced from these gradients can be given by [26]

$$u_{\theta,s} = -\frac{\nabla p_s \times \mathbf{B}}{q_s n_s B^2} + \frac{\mathbf{E} \times \mathbf{B}}{B^2}, \tag{1.3}$$

where p_s is the pressure, q_s is the charge, and $\mathbf{E}$ is the electric field. A general understanding of the impact of the these drifts can be found by looking at the direction of the resulting current. We may then define the thrust in terms of this quantity by integrating the Lorentz force term throughout the entire volume of the nozzle,

$$T = \int \sum_s q_s n_s u_{\theta,s} B_r d\mathbf{V}. \tag{1.4}$$

We thus find that the magnitude of the thrust directly depends on the direction of the azimuthal current.

Alternatively, it is common to consider acceleration in these devices via a conservation of the electron magnetic moment, $\mu = \frac{m_e v_{e,\perp}^2}{2B}$ [11]. In this paradigm, the conservation of this quantity through an expanding field results in a conversion of the perpendicular velocity into parallel velocity through an equivalent conservation of kinetic energy $KE = \frac{m_e}{2}\left(v_{e,\perp}^2 + v_{e,||}^2\right)$. This field-aligned acceleration then induces the ambipolar electric field that accelerates the ions. While within a different framework, this description nonetheless produces an equivalent physical mechanism for magnetic nozzle acceleration, since $T_e \propto v_{e,\perp}^2$.

Given the direct impact of volumetric azimuthal currents in the plume, extensive research has been done in theory, simulation, and experiment to determine their magnitudes and impact on thruster performance [114, 45, 112, 40, 113]. Indeed, a common experimental method for determining the currents in the plume includes measuring the induced magnetic field using B-dot probes or diamagnetic pickup coils [94]. These experiments directly measure the plasma-induced magnetic field by integrating the signal on these probes during thruster shutdown. After having a map of this field, applying Ampere's law $\nabla \mathbf{B} = \mu_0 \mathbf{j}$ with the boundary condition that $j_\theta = 0$ on centerline provides a map of the total plasma current. Roberson performed the first such experiment, which identified a uniformly diamagnetic plume [96], indicating that the azimuthal currents were indeed thrust-producing. This informed modeling work by Ahedo and Merino, who applied the method of characteristics to determine plasma evolution through the plume [3]. They predicted that the direction of electron current depended solely on the upstream conditions, i.e. the profile of plasma potential and electron pressure generated at the source. However, further experiment revealed that this may not be the cases. Takahashi et al. performed a similar experiment as Roberson on a different plasma source and identified a mode transition— while the electrons maintained a diamagnetic drift upstream, they changed direction downstream to the paramagnetic direction [110]. The results by Takahashi et al. implied that predicting the drift direction and thrust production may be more complicated than initially believed.

One possible reason for this discrepancy is the simplifying assumptions that were made in this modeling work. As is common for laboratory plasma modeling, this work assumed a lack of resistivity or kinetic effects. However, it is now known that the reality is not as straightforward, as the presence of collisions or kinetic effects will affect the net currents [6, 89]. Indeed, more modern research into these devices has found that kinetic effects are likely present and may dominate the expansion dynamics [95, 86, 127]. However, the details of how this happens is not yet clear, and may vary between devices. For instance, research involving double layer thrusters often discusses the possibility of a high energy electron tail [1]; however, others observe the opposite, where there is a surprising dearth of high energy electrons [126]. Regardless of the details behind this potential discrepancy between simulation and experiment, the literature is conclusive that these plasmas remain not understood, and the precise mechanisms behind the direction and magnitude of the azimuthal currents remain unknown.

While the currents in the azimuthal direction determine the thrust, cross-field momentum flux in the $r - z$ plane also impacts thruster performance. In the next section, we explain this process and several theories as to how it might occur.

1.3.2 Cross-field momentum transport

The question of cross-field transport is a crucial area of research for magnetic nozzle development. This concept is often framed in terms of detachment. Since a magnetic nozzle exhibits an inherently closed field geometry, every field line that exits the plasma source will ultimately return to it. In the ideal, highly-magnetized case, a charged particle will tightly orbit a magnetic field and follow it as it bends back towards the thruster. Without a mechanism for inward cross-field transport, the plasma will follow the field back to the thruster and negate any thrust generation. While this question is of vital importance for both fully- and partially-magnetized systems, we will focus our analysis here on the partially-magnetized systems.

Outward cross-field transport can further impact thrust generation. As the plasma diverges faster than the magnetic field, more plasma is likely to impact the thruster

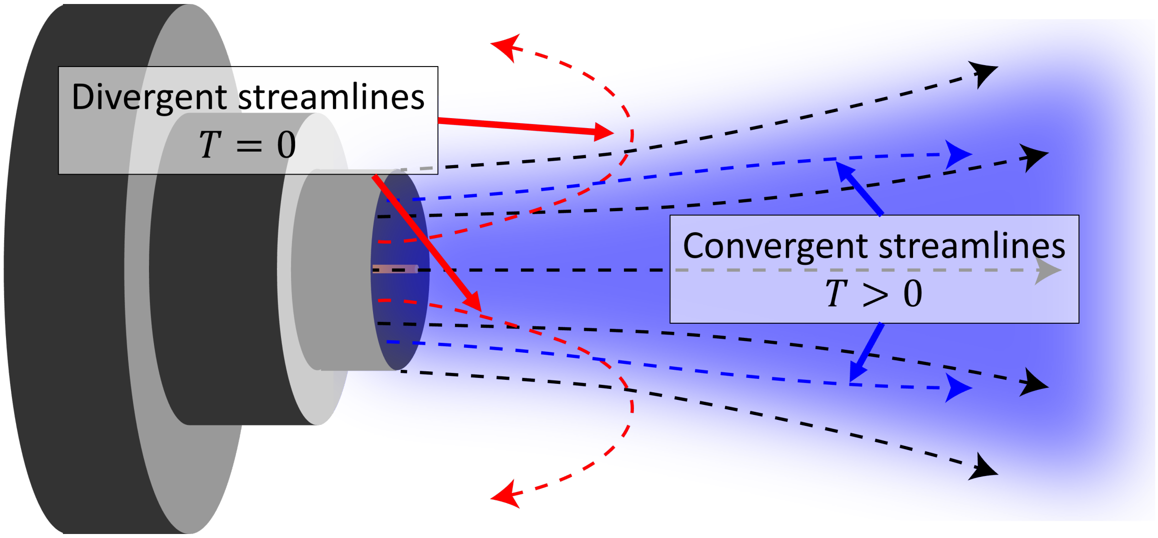

Figure 1.2: Magnetic nozzle with ion and electron streamlines representing convergent and divergent transport schemes.

(and any spacecraft equipment in the area) and, assuming an eventual inward transport mechanism, increase divergence losses. This situation may even occur in the partially magnetized case. As the electrons diverge, they will induce a radial ambipolar field that will further diverge the ions as well. Figure 1.2 presents potential electron and ion streamlines for both convergent and divergent detachment scenarios.

Previous mechanisms for cross-field transport rely on relaxing several assumptions in the momentum equation [4],

$$m_s n_s \frac{\partial \mathbf{u}}{\partial t} + m_s n_s (\mathbf{u} \cdot \nabla)\mathbf{u} = q_s n_s \left[\mathbf{E} + \mathbf{u} \times (\mathbf{B}_0 + \mathbf{B}_1)\right] - \nabla p_s + \mathbf{R}_s. \tag{1.5}$$

Here, m_s is the mass, $\mathbf{u}$ is the fluid velocity, t is time, and $\mathbf{R}_s$ is the resistive force. The left hand side represents the inertia of the species, and the three terms on the left indicate the Lorentz force, the pressure force, and the total resistivity, respectively. The Lorentz force term includes both the applied field $\mathbf{B}_0$ and the plasma-induced field $\mathbf{B}_1$.

Three assumptions are often made in analyzing this equation. First, the left hand

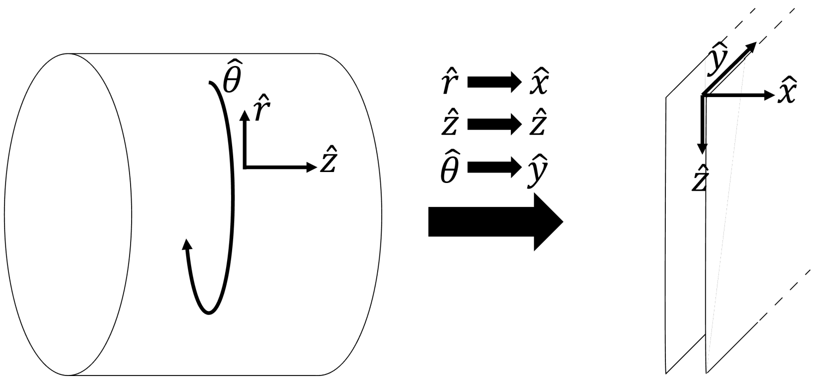

Figure 1.3: Illustration of the approximate conversion between cylindrical and slab geometry.

side is often set to zero for the electrons. This assumption is based on the fact that the electron mass is far less than the ion mass. In taking the limit of $m_e \to 0$, Eqn. 1.5 implies that the electrons will orbit magnetic field lines with a gyration radius (or "Larmor radius") of zero. The second assumption is that the induced magnetic field is zero, such that $\mathbf{B}_0 + \mathbf{B}_1 \approx \mathbf{B}_0$. Finally, the zero resistivity assumption removes the third term from the right hand side and assumes that streaming electrons do not interact with background ions or neutrals. Previous theories regarding cross-field transport rely on relaxing one of these assumptions.

The concept that resistivity can induce a cross-field transport was first put forward by Moses [89]. While he used a single-fluid model without a cross-field pressure gradient, the idea is easily applicable to the single species momentum equations. We can arrive at these equations by assuming ions and any neutrals to be motionless, which allows us to take the resistivity term as $\mathbf{R}_e = -m_e n_e \nu_e \mathbf{u}_e$. We can further take a slab geometry, implying symmetry in the y direction, gradients in the x direction, and a constant magnetic field in the z direction. This geometry is illustrated in Fig. 1.3 The resulting momentum equations for massless electrons in the x and y directions are

$$0 = \Omega_e(v_E + v_D) + u_{e,y} - u_{e,x} \tag{1.6}$$

$$0 = \Omega_e u_{e,x} + u_{e,y} \tag{1.7}$$

where we have defined the Hall parameter Ω_e to be the ratio of the electron cyclotron frequency to the collision frequency, $\Omega_e = \frac{eB_z}{m_e \nu}$. These may be readily solved for the x and y velocities, yielding

$$u_{e,x} = \frac{\Omega_e}{1 + \Omega_e}\left(v_E + v_D\right) \tag{1.8}$$

$$u_{e,y} = \frac{\Omega_e^2}{1 + \Omega_e^2}\left(v_E + v_D\right). \tag{1.9}$$

Fundamentally these relations imply that a finite collisionality slows down the electron drift and induces cross-field transport. Moreover, the direction of this transport depends entirely on the net direction of the drift motion. If we identify the cartesian coorinates (x, y, z) with the cylindrical equivalent (r, θ, z), we can then determine the direction of transport. Recalling that the pressure gradient is generally inwards and that the diamagnetic drift should be dominant for thrust production, we find that the total azimuthal velocity is in the $+\hat{y} = +\hat{\theta}$ direction. This fact in turn implies that transport in the $\hat{x} = \hat{r}$ direction is also positive, meaning that electrons cross field lines *outwardly*. Thus, full inward detachment of electrons from this mechanism requires a downstream paramagnetic population.

A second theory relaxes the assumption that the induced magnetic field is zero and instead allows the azimuthal currents to influence the total field [9, 10]. In this theory, the plasma induces a magnetic field that stretches the applied field axially. In doing so, the plasma is able to adhere to the field lines until the field becomes too small

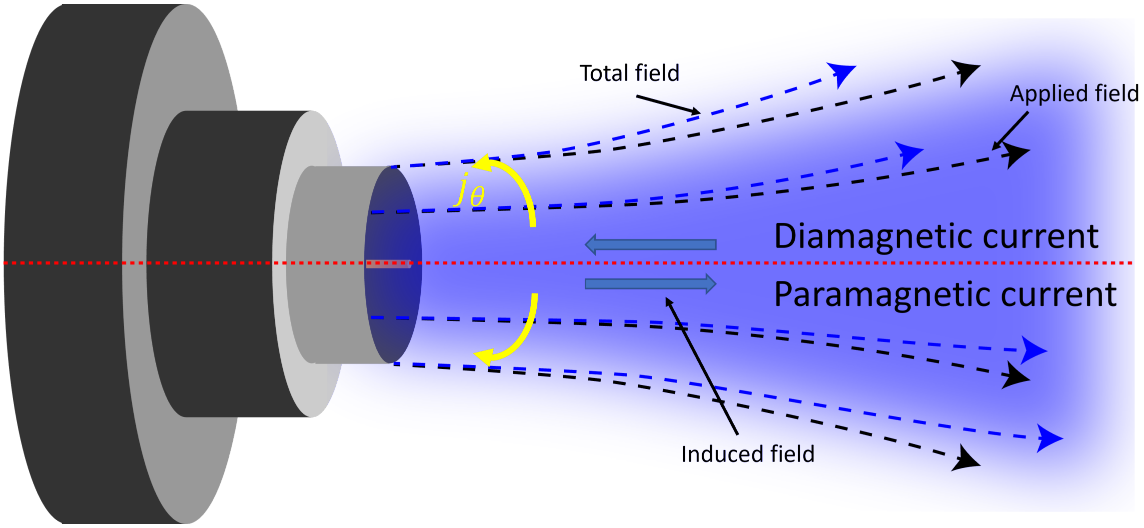

Figure 1.4: Potential influence of diamagnetic (above) and paramagnetic (below) currents on total background magnetic field.

to affect the plasma and it can be considered detached. This idea was put forward in the context of high power magnetic nozzles with attached ions and was discussed in terms of a single fluid theory. However, we may similarly discuss its implications assuming a stagnant ion population and an electron fluid. Indeed, applying a simple right-hand rule shows that the induced magnetic field from a diamagnetic drift will counter the applied field, expanding the geometry and further diverging the plasma.

A final theory relaxes the assumption of negligible electron inertia. Ahedo and Merino established this theory by solving the electron fluid equations in cylindrical coordinates [6]. Incorporating finite Larmor radius effects provided a term that depends on the direction of azimuthal electron drift. They ultimately found that the extent to which electron streamlines separated from the applied field lines scaled with $m_e u_{e,\theta}$. While this term is often neglected in similar analyses due to the vanishing mass of the electrons, they found that the magnitude of azimuthal velocity made it comparable to other terms in the fluid equations. Moreover, they found that the direction of transport depended on the sign of $u_{e,\theta}$– namely, a diamagnetic drift induced outward transport while a paramagnetic drift induced inward transport.

With all of these theories, a paramagnetic drift is required for inward transport. While a majority diamagnetic current is desirable for thrust generation, a mode transition such as that observed by Takahashi et al. [110] may be present, yielding a paramagnetic current and inward transport downstream. However, it is likely that not all plasmas depend on this transition, such as the fully magnetic plume measured by Roberson [96]. It is thus prudent to consider all of these mechanisms in terms of thruster divergence loss. However, doing so leaves open the question of eventual, inward electron detachment. One further possibility is the relatively simple concept that the electrons fully demagnetize downstream. As the magnetic field weakens, it is possible that the electron Larmor radius becomes comparable to the magnetic field gradient length $\nabla \ln(B)^{-1}$. The theories we have discussed so far do not incorporate this limit, but this lack of magnetization likely implies that the concepts of drift and transport direction fail. As the applied field continues to weaken downstream, the electrons will progress as a balance of electric field induced by charge separation with the ions and their own pressure gradient. This process would appear similar to traditional ambipolar diffusion. The concept of electron demagnetization in this way has not been thoroughly studied, but it has been theorized previously as a final scenario to detach electrons if no other mechanism succeeds [4]. This concept is not the subject of the current work, but does provide an explanation for how electrons may detach from field lines and allow magnetic nozzles to generate thrust.

1.3.3 Heat conduction

While cross-field transport mainly influences divergence losses, it does not determine the total amount of energy delivered to the ions. Electron-driven magnetic nozzles deposit energy first into the electrons, which then transfer energy into the ions. We can understand this process with the zero-inertia, field-aligned electron

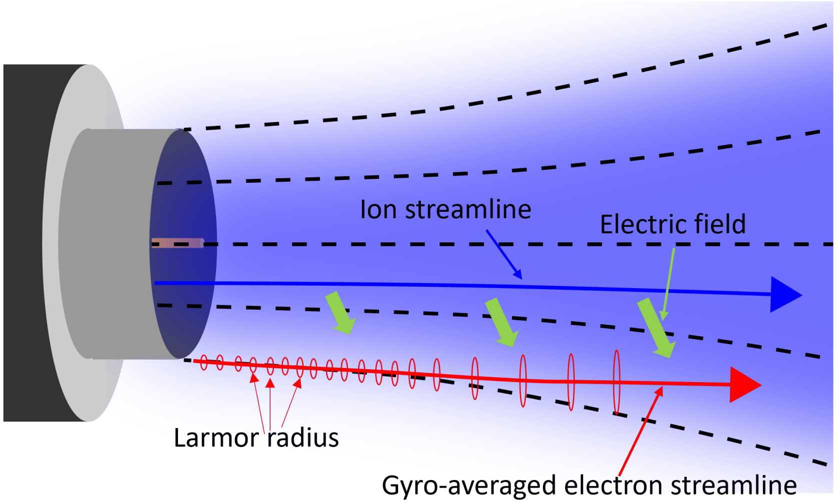

Figure 1.5: Full electron demagnetization by large Larmor radius.

momentum equation neglecting collisions:

$$0 = -en_e E_{\parallel} + \frac{\partial(n_e T_e)}{\partial \parallel}. \tag{1.10}$$

Here we find that the electric field forms as the pressure decreases. The corresponding ion momentum equation is

$$\frac{\partial u_{i,\parallel}^2}{\partial \parallel} = n_i e E_{\parallel} = \frac{\partial(n_e T_e)}{\partial \parallel} \tag{1.11}$$

implying that the ions accelerate along field lines directly at the expense of the electron thermal energy. From this simple analysis, we see that the thermodynamics governing the electron expansion is thus vital to predicting ion acceleration. Despite the connection between electron thermodynamics and ion acceleration, however, in many cases the thermodynamics governing this expansion remains poorly understood.

To facilitate modeling modeling the thermodynamics of these systems, it is common to adopt a polytropic equation of state,

$$\frac{T_e}{n_e^{\gamma-1}} = \text{const.} \tag{1.12}$$

Here, γ is referred to as the polytropic index. The justification for this assumption typically comes from the two physical limits that γ may maintain. When $\gamma = 1$, electrons are mobile enough to smooth out any temperature gradients, and Eqn. 1.12 reduces to the isothermal case of $T_e = \text{const}$. The other limit arises in the so-called adiabatic limit, where there is no heat flux in the system. In this case, γ takes a value based on the number of degrees of freedom N of the system, $\gamma = \frac{N+2}{N}$. In a three-dimensional system, this limit corresponds to $\gamma = 5/3$. While assuming that γ is constant simplifies the analysis, it does not reduce the number of free variables, as we need a further closure scheme to predict the value of γ.

One such closure may lie in the heat flux. To connect heat flux to the polytropic index and the total ion acceleration, we may follow the process explained in Ref. [84]. We begin by using a polytropic assumption Eqn. 1.12 to solve for n_e in Eqn. 1.10, which gives

$$\frac{\gamma}{\gamma-1}\frac{\partial T_e}{\partial \parallel} = eE_{\parallel}. \tag{1.13}$$

We may integrate this relation from the most upstream condition (subscript 0) to a downstream condition (subscript f), assuming full expansion and full cooling of the electrons, to give

$$\frac{\gamma}{\gamma-1}T_{e,0} = \Delta\phi \tag{1.14}$$

where $\Delta\phi$ is the total potential drop during the expansion. We may then consider the total downstream energy flux as a function of axial position by incorporating inertial ion flux, electron convection, and electron heat flux Q_e,

$$P = \dot{n}\left(\frac{m_i u_i^2}{2} + \frac{\gamma}{\gamma-1}T_{e,0}\right) + Q_e \tag{1.15}$$

where $\dot{n}$ is the total particle flow rate, which must be constant along the expansion by conservation of mass. By conservation of energy, the upstream power flux must be equal to the downstream value, where $T_e = Q_e = 0$. Equating these two limits, we find that the initial heat flux is

$$Q_{e,0} = \frac{3}{2}\dot{n}_i T_{e,0}\left(\frac{5/3-\gamma}{\gamma-1}\right). \tag{1.16}$$

Thus, if γ takes a non-adiabatic value, the heat flux must be finite. Moreover, a fully isothermal plasma is not possible– such a scenario would imply *infinite* heat flux downstream.

In practice, the measured value of γ from simulation and experiment for expanding electrons does not correspond to either of the limiting cases, rather taking an intermediate value [100, 116, 28, 75, 63, 116, 64, 83]. This suggests that the actual electron heat flux along the field lines in these systems is finite, though how this term should scale remains an open question. Given the importance of the expansion thermodynamics to modeling these systems, there is a need to better understand the the physical nature of this flux.

To this end, there have previously been several studies on the factors that govern the parallel electron heat flux–particularly in low temperature expanding plasmas [126, 7, 75, 100, 115, 118]. These previous works have been couched in terms of trying to explain the measured effective value of polytropic index, γ. One particular promising result is the work of Little and Choueiri who hypothesized that the heat flux is governed by a classical Fourier law, $\mathbf{Q}_e = \kappa \nabla T_e$, where$\kappa = \alpha \frac{n_e T_e}{\nu_e m_e}$ is the thermal conductivity. Here α is a constant of order unity and ν_e is the total electron collision frequency [75]. To evaluate this theory, they measured background plasma properties along the centerline of their radiofrequency magnetic nozzle to directly determine the polytropic index of the expansion. This work showed that assuming this form for heat flux, they were able to find marked agreement between the measured polytropic index in their experimental magnetic nozzle. However, as was noted in this work, while the scaling of the heat flux term was correct, the actual magnitude of the heat flux was unphysical. Indeed, the low level of collisions in their device led to heat flux downstream that was an order of magnitude greater than the total power actually used to create the discharge. This led the authors to conclude that there may be a source of anomalous electron collisions in the plasma in the direction of the expanding magnetic field, impeding the Fourier-driven heat flux. The source of this anomalous transport, however, remained an open question. Commonly in plasma physics, such an anomalous collision frequency may be explained by the presence of instabilities.

1.4 The role of instabilities in impacting thruster operation

Instabilities are nearly ubiquitous in plasma physics. They arise in fusion, space, and laboratory plasmas alike, although they take a wide variety of forms. In plasma-based propulsion, interest is continually growing on the detailed role that various modes take in determining plasma dynamics. Perhaps the most prominent example in contemporary propulsion research is investigations into unstable modes in the hall effect thruster. These devices apply a crossed electric and magnetic field to confine electrons and accelerate ions [59, 50]. However, experiments reveal a cross-field transport that is often orders of magnitude greater than the classical prediction. While several theories have been proposed to explain this phenomenon, one in particular that is gaining traction is the role of an electron drift instability [38, 23, 18, 70, 117]. These modes grow at the expense of the electron drift, acting as an effective resistivity that allows electrons to cross field lines. However, the exact nature of these waves depend strongly on the properties of the plasma. In this section, we will discuss three potential candidates that may be present in a magnetic nozzle— anti-drift, ionization, and lower hybrid drift moes.

1.4.1 Potential instabilities present in a magnetic nozzle

Anti-drift modes are fluid instabilities that derive energy from fluid motion. In laboratory plasmas where ions are unlikely to be magnetized, these waves are often connected to electron cross-field drifts. Typically, the dispersion relation is simplified by the neglect of electron inertia, but it may include of any combination of collisions, electric field, pressure, and propagation both perpendicular to and parallel to the applied field [98, 102, 55, 43]. As such, the details of the dispersion relations may vary. Fundamentally, however, the propagation frequency tends to scale inversely with the drift velocity (hence "anti"-drift).

These modes have been understood mathematically for decades [98, 43] and have been observed in a variety of plasmas [42, 104]. Specifically, research into various laboratory plasmas frequently discusses these modes. The hollow cathode is one such system where these waves have been identified [60, 62, 53]. These devices generate force a current through a plasma through an electrostatic field, thus generating a strong electron current. In propulsion, hollow cathodes are often used in Hall thrusters, where they are immersed in an axially expanding magnetic field akin to that of a magnetic nozzle. In these systems, the wave is driven unstable by collisions in the presence of a diamagnetic electron current and propagates primarily azimuthally, but maintains a slight character along field lines. Moreover, when the cathode is mounted on a Hall thruster, the presence of these modes has been correlated to oscillations in the discharge current [62, 53]. Namely, both high speed imagery and probe measurements have identified modes between 50 and 90 kHz in these devices. These frequency patterns were matched with those measured in the discharge current, indicating that they are at least correlated with electron transport across field lines. This link implies that the wave likely enhances cross-field transport in hollow cathodes and further provides motivation for their investigation in magnetic nozzles.

Another candidate for wave presence in a magnetic nozzle is the so-called ionization mode. These waves can typically be understood by a so-called "predator-prey" model. In this paradigm, a large presence of background neutrals ("prey") increases ionization ("predator") to start the instability. As ionization proceeds, neutrals are depleted, which then halts ionization. Finally, a new population of neutrals enters the system to restart the process. These waves tend to be coherent, low frequency oscillations on the order of ≈ 10 kHz.

Similar to anti-drift modes, ionization modes have also been observed in hollow cathodes [48], although they tend to arise when there is no applied field. In the previous work, a full theoretical model was developed and electrostatic probe measurements were taken, indicating the presence of a strong, low frequency mode that balanced an ionization process with diffusion through the plume. In cathodes, the presence of this wave drives the so-called plume mode operation and is linked to the onset of the axially-propagating ion acoustic turbulence. The resulting operation is known to enhance erosion of the cathode face. However, in the presence of a magnetic field, these modes are suppressed– an anti-drift mode is more likely to be present instead.

The lower hybrid drift instability (LHDI) is driven unstable in the presence of a strong diamagnetic drift in a partially magnetized system [68]. It is primarily observed in plasmas undergoing magnetic reconnection [12]— a process involving the apparent breaking apart and recombining of magnetic fields that induces significant plasma acceleration. In these systems, the lower hybrid mode is often found at the periphery of the system, where it enhances plasma transport into the central, reconnecting region and increases the resulting reconnection rate. The naming convention comes from the maximized growth rate of the wave at the lower hybrid frequency, typically defined in these contexts as $\omega_{LH} = \sqrt{\Omega_{c,e}\Omega_{c,i}}$, where $\Omega_{c,s} = \frac{q_s B}{m_s}$ is the gyrofrequency of species s. Furthermore, it is most unstable at a low plasma β, i.e. when the magnetic field energy is much larger than the plasma pressure. The notable presence of these waves when strong density gradients are present in low β plasmas make the LHDI a prime candidate for an instability present in a magnetic nozzle.

1.4.2 The influence of instabilities on plasma dynamics

The presence of instabilities may impact all three areas of thruster operation discussed in Sct. 1.3. As instabilities grow, they derive their energy from the surrounding plasma. In the case of drift-driven modes such as anti-drift or lower hybrid drift modes, this energy comes from the azimuthal electron drift. This interaction slows the electrons, which in turn may decrease the current that determines the thrust. In the case of a predominantly diamagnetic plume current, this phenomenon may be harmful to thrust generation.

Moreover, the same energy loss from the electron current may be modeled as an effective resistivity. Similar to the theory of cross-field transport by classical collisions, the onset of a drift-driven instability may induce electron cross-field transport. This effect will be tied to the direction of drift– in the case of a diamagnetic current, the electrons will be forced outwards, inducing a radial electric field that will accelerate the ions in the same direction and induce a divergence loss. Moreover, a diamagnetic drift-driven mode in the discharge region will further force particles towards the walls. Particles impacting the walls are most likely to recombine into a neutral particle, which will require reionization before begin accelerated by the electric field. If a significant number of particles recombine at the walls, the energy that was expended ionizing them will be lost, and thruster efficiency will suffer.

In the opposite sense, a paramagnetic current will induce inward transport. In this situation, the beam will be collimated. While this may appear to be a more ideal situation, its benefits are countered by the fact that the paramagnetic current inherently negates thrust by inducing an attractive force between the plume and the applied magnetic field.

Finally, the presence of waves may impact heat transport as well. Similar to how the effective drag induces a resistivity along field lines, waves propagating along the magnetic fields may impede heat flux [20]. Again, this effect would harm acceleration. As we discussed in Sct. 1.3.3, decreasing the downstream heat flux will restrict the total energy available to accelerate the ions, thus reducing the total momentum transport and thrust generation.

Given the potential significance of instabilities on the operation of magnetic nozzles, there has been prior investigations into their presence and possible effects.

1.4.3 Previous work investigating instabilities in magnetic nozzles

Anti-drift modes have also been observed in radiofrequency plasma sources. Work by Light et al. [73] detected their presence in a helicon discharge and linked them to enhanced plasma loss to the walls. Their findings showed that, contrary to what is typically assumed, the growth of this mode implied an eventual *loss* of plasma confinement at higher field strengths. While this work showed the onset of these modes in the source region, it is likely that such a plasma expanding into a nozzle may maintain it as well. Thus, given the link between anti-drift modes and cross-field transport and their identification in similar laboratory plasmas, we posit that they may be present and impact transport in magnetic nozzles as well.

Finally, previous work has analyzed the potential presence of such a mode in a magnetic nozzle [1]. This latter work developed a theory based on the existence of a population of electrons generated downstream and flowing upstream up the plasma potential gradient. In this paradigm, such a population was required to drive the mode unstable. However, further measurements of the electron energy distribution function on the same device revealed that no such population was necessarily present [111]. Nevertheless, this prior work involved a source that maintained different background plasma properties than the one we are considering here, and the possibility remains that a different ionization scheme may provide an environment in which an ionization mode may grow.

With these observations taken together, it is indeed possible that an ionization mode is present in a magnetic nozzle. It likely does not universally take the same characteristic as that presented by Aanesland et al. [1], but it is possible that one more akin to the theory presented by Georgin may be present in a magnetic nozzle. Chapter VI elaborates on this possibility.

In 2015, Olsen et al. developed an experiment to detect the presence of a lower hybrid drift instability in the VX-200, a 100 kW class magnetic nozzle that magnetizes both ions and electrons [92]. This device implements a helicon ionization scheme and ion cyclotron heating to further heat the plasma, which is only possible at high ($\gtrsim 1$ T) magnetic fields. They observed the onset of electrostatic turbulence downstream and theorized that it may be either a modified two stream or lower hybrid instability [91, 49]. They indeed observed an oscillating electric field in the plume and linked it to a zone where the ions undertook ballistic trajectories, which they determined as the detachment point. This work provided a vital first experimental investigation into the relation between cross-field transport and the onset of instabilities.

However, the work on the VX-200 did not directly observe the dispersion of this mode. They further did not implement the theoretical dispersion in a cross-field transport estimate, nor did they extend their observations to the lower power devices used in space today. Given their observation of an oscillation and the potential link to cross-field transport coupled to the fact that instabilities are known to induce transport in similar devices, this work further investigates the detailed roles of these modes on cross-field transport.

1.5 Primary objectives of the current research

Now that we have established the magnetic nozzle in the context of contemporary space propulsion development and research questions, we are prepared to introduce the purpose of the present work. In the rest of this thesis, we aim to answer four primary questions. First, what modes are present in the plume a partially magnetized magnetic nozzle? Second, what role do these waves play in enhancing cross-field electron transport in the plume? Third, how do these modes influence downstream heat transport? Fourth, what modes may be present in the discharge region, and how might they impact thruster performance? Throughout this work, we will attempt to answer these four questions from a theoretical and experimental standpoint.

1.6 Organization of the present work

The rest of this thesis is organized in the following way. We begin by further developing the theory to justify the hypothesis that instabilities impact cross-field transport and heat conduction in Chap. II. We next explain the experimental methods used in this work to detect and analyze waves in a magnetic nozzle in Chap. III. Chapter IV discusses our observations in the context of electron cross-field transport, and Chap. V presents their possible impact on heat conduction. We analyze the presence of a low-frequency mode that is a generalization of an anti-drift instability and an ionization wave in Chap. VI. Finally, we summarize our findings and present possibilities for future work in Chap. VII.

1.7 Conclusion

In this section, we have introduced the fundamental concepts upon which we will build this thesis. We began by introducing the idea of a magnetic nozzle and discussed their thrust generation mechanisms. We outlined their significance in the field of electric propulsion and outined their primary strengths as propulsion devices. We introduced the problems of cross-field transport and heat conduction in these plasmas and described contemporary understanding of the physics that may describe them. We then introduced the concept that the presence of instabilities may influence both of these questions and elaborated on the three modes that we will be discussing in this work- anti-drift modes, ionization modes, and the lower hybrid drift instability.

CHAPTER II

Theory

2.1 Introduction

In this chapter, we establish the fundamental theory from which we determine the impact of waves on macroscopic plasma properties. We begin by describing the fundamentals of continuum mechanics based on a kinetic description. We introduce the collision term, then present the resulting fluid equations based on a moment-taking process. We then introduce Gauss' law and explain the concept of the dispersion relation through a linear perturbation analysis. Next, we apply nonlinear theory to deduce the impact of higher order terms and describe the application of this theory with the dispersion relation in what is commonly known as quasilinear theory. This analysis reveals a wave-induced resistivity, from which we then derive an effective collision frequency. We then derive the dispersion relation for the lower hybrid drift instability, which will be used in the effective collision frequency. After describing the effective collision frequency, we discuss the prediction of the polytropic index γ using a quasi one-dimensional analysis of an expanding magnetic field. To this end, we combine a Fourier law, a polytropic assumption, and the electron energy equation. Finally, we summarize our findings and briefly discuss how we can use what we have found to analyze a magnetic nozzle.

2.2 Influence of waves on transport

In this section, we will determine the effect of waves on macroscopic plasma properties. We begin fundamentally with the collisional kinetic equation and outline the process of taking moments to arrive at the fluid equations. Throughout the process, we maintain an arbitrary collision operator. We then show how this collision operator may manifest on a steady-state distribution function in the presence of an oscillating electric field and number density at higher frequencies, and finally derive a relation between these two values based on theory underlying a lower hybrid drift instability. We next find an expression for an effective collision frequency induced by a wave in a magnetic nozzle based on observable plasma properties and number density oscillations. We then apply this concept to the fluid equations in a quasi-one dimensional model of an expanding plasma to determine its effect on electron thermodynamics.

2.2.1 Kinetic equation

While any substance can be reduced to its individual particles, a continuum can be modeled as a smooth function that describes the density of particles at a particular time, position, and velocity. This function is thus a seven-dimensional scalar function $f(t, \mathbf{x}, \mathbf{v})$, where t is time, $\mathbf{x}$ is the particle position, and $\mathbf{v}$ is particle velocity. Moreover, we may identify the link between the parameters in phase space as [26]

$$\frac{\partial \mathbf{x}}{\partial \mathbf{t}} = \mathbf{v} \tag{2.1}$$

$$\frac{\partial \mathbf{v}}{\partial t} = \mathbf{a} \tag{2.2}$$

where we have defined **a** as the acceleration term that we will define for a plasma shortly. The full derivative then takes the form

$$\begin{aligned}\frac{df}{dt} &= \frac{\partial f}{\partial t} + \frac{\partial \mathbf{x}}{\partial t} \cdot \frac{\partial f}{\partial \mathbf{x}} + \frac{\partial \mathbf{v}}{\partial t} \cdot \frac{\partial f}{\partial \mathbf{v}} \qquad (2.3)\\ &= \frac{\partial f}{\partial t} + \mathbf{v} \cdot \frac{\partial f}{\partial \mathbf{x}} + \mathbf{a} \cdot \frac{\partial f}{\partial \mathbf{v}}. \qquad (2.4)\end{aligned}$$

This description describes the change in f along its phase space trajectory. Given that f is by definition a phase-space density function, we can apply Liouville's theorem to determine how it evolves. This theorem states that, in the absence of interactions between particles, the phase-space density will be constant, $df/dt = 0$. Inter-particle interactions affect this relation in one of a variety of complex ways, so we will abstract all of them as a currently undefined collision operator $C[f]$. This term is effectively an arbitrary source/sink term that may include Coulombic interactions, ionization, or hard-sphere like collisions. We may incorporate this term in the definition to find

$$\frac{\partial f}{\partial t} + \mathbf{v} \cdot \frac{\partial f}{\partial \mathbf{x}} + \mathbf{a} \cdot \frac{\partial f}{\partial \mathbf{v}} = C[f]. \qquad (2.5)$$

The collision term can take a variety of forms. For instance, the Boltzmann collision operator, a Fokker-Planck term, and the BGK collision operator are common methods to solve the kinetic equation. We will see in Sct. 2.2.3 that plasma instabilities may induce an effective collision operator as well on certain time scales. However, we are going to allow it to remain arbitrary for this discussion.

The acceleration term can take a variety of forms, but strictly represents volumetric forces. In a neutral gas, this may be gravity or a centrifugal, effective force.

In plasmas, the dominant force acting on a species is typically the Lorentz force:

$$\mathbf{a} = \frac{q_s}{m_s}\left(\mathbf{E} + \mathbf{v} \times \mathbf{B}\right). \tag{2.6}$$

In most situations, the distribution function itself can be prohibitively difficult to measure directly. Indeed, even knowing the external fields applied and having a good model for the collision operator yields an infinite number of possible solutions. To overcome this difficulty, it is often more tractable to discuss the species in terms of its fluid equations. In the following section, we derive and explain the first three, which are the most commonly used.

2.2.2 Fluid equations

The fluid equations arise by taking moments of the kinetic equation. This process involves multiplying Eqn. 2.5 by a power of $\mathbf{v}$ and integrating over velocity space [14]. We start with the zeroth moment, which constitutes a simple integration:

$$\int \frac{\partial f}{\partial t} + \mathbf{v} \cdot \frac{\partial f}{\partial \mathbf{x}} + \mathbf{a} \cdot \frac{\partial f}{\partial \mathbf{v}} d\mathbf{v} = \int C[f] d\mathbf{v}. \tag{2.7}$$

We can take this result term by term. We begin with the time-dependent term,

$$\int \frac{\partial f}{\partial t} d\mathbf{v} = \frac{\partial}{\partial t} \int f d\mathbf{v} \tag{2.8}$$

$$= \frac{\partial n}{\partial t} \tag{2.9}$$

where we have used the fact that the time derivative and the velocity space integration commute and defined $n = \int f d\mathbf{v}$ as the particle density in space.

The second term can be similarly reduced,

$$\int \mathbf{v} \cdot \frac{\partial f}{\partial \mathbf{x}} d\mathbf{v} = \frac{\partial}{\partial \mathbf{x}} \cdot \int \mathbf{v} f d\mathbf{v} \tag{2.10}$$

$$= \frac{\partial n\mathbf{u}}{\partial \mathbf{x}}, \tag{2.11}$$

where we have used the fact that $\mathbf{v}$ and $\mathbf{x}$ are independent and defined the average velocity $u = \frac{1}{n} \int \mathbf{v} f d\mathbf{v}$. For the acceleration term, we will use the Lorentz force and integrate by parts to find

$$\frac{q}{m} \int (\mathbf{E} + \mathbf{v} \times \mathbf{B}) \cdot \frac{\partial f}{\partial \mathbf{v}} d\mathbf{v} = \frac{q}{m} \mathbf{E} \cdot \int \frac{\partial f}{\partial \mathbf{v}} d\mathbf{v} + \frac{q}{m} \int (\mathbf{v} \times \mathbf{B}) \cdot \frac{df}{d\mathbf{v}} \tag{2.12}$$

$$= 0. \tag{2.13}$$

The first term vanishes due to the fact that f approaches zero at $\pm\infty$. The second term disappears similarly since $\frac{\partial}{\partial \mathbf{v}} \cdot (\mathbf{v} \times \mathbf{B}) = 0$.

We can then manipulate the zeroth moment of the collision term as

$$\int C[f] d\mathbf{v} = \left(\frac{\partial n}{\partial t} \right)_c . \tag{2.14}$$

This shows that the only collision terms that contribute to the zeroth moment are those that change the total number of particles. The zeroth moment equation takes the form

$$\frac{\partial n}{\partial t} + \frac{\partial}{\partial \mathbf{x}} \cdot (n\mathbf{u}) = \left(\frac{\partial n}{\partial t} \right)_c . \tag{2.15}$$

Equation 2.15 is known as the continuity equation and represents the conservation of mass.

Next, we may take the first moment by multiplying the kinetic equation by $\mathbf{v}$ and integrating. We will again approach this equation term by term. The first term simply becomes

$$\int \mathbf{v}\frac{\partial f}{\partial t}d\mathbf{v} = \frac{\partial n\mathbf{u}}{\partial t}, \tag{2.16}$$

representing the time rate of change of momentum. To evaluate the second term, we will first make a substitution $\mathbf{v} = \mathbf{u} + \mathbf{v}_r$, where $\mathbf{v}_r$ is the random (i.e. zero average) component of the velocity and $\mathbf{u}$ is the bulk velocity. Note that $d\mathbf{v} = d\mathbf{v}_r$.

$$\begin{aligned}
\int \mathbf{v}\mathbf{v}\cdot\frac{\partial f}{\partial \mathbf{x}}d\mathbf{v} &= \int (\mathbf{u}+\mathbf{v}_r)(\mathbf{u}+\mathbf{v}_r)\cdot\frac{\partial f}{\partial \mathbf{x}}d\mathbf{v} && (2.17)\\
&= \frac{\partial}{\partial \mathbf{x}}\cdot(n\mathbf{u}\mathbf{u}) + \int \mathbf{v}_r\mathbf{v}_r\frac{\partial f}{\partial \mathbf{x}}d\mathbf{v} && (2.18)\\
&= \frac{\partial}{\partial \mathbf{x}}\cdot(n\mathbf{u}\mathbf{u}) + \frac{1}{m}\frac{\partial}{\partial \mathbf{x}}\cdot\mathbf{P} && (2.19)
\end{aligned}$$

where we have defined the pressure tensor as $\mathbf{P} = m\int \mathbf{v}_r\mathbf{v}_r f d\mathbf{v}$. In general, the pressure tensor accounts for varying forces exerted by a species in all directions. For our purposes, we will simplify by assuming an isotropic population with no shear. In doing so, we may replace $\mathbf{P}$ with a scalar pressure p. Since it is equal in all directions, we now redefine this value to be the pressure in *any* direction. We may thus take the total random energy and divide by the total degrees of freedom (typically 3) as

$$p = \frac{m}{3}\int \mathbf{v}_r\cdot\mathbf{v}_r f d\mathbf{v}. \tag{2.20}$$

We may evaluate the acceleration term by integration by parts,

$$\int \mathbf{v}q\left(\mathbf{E}+\mathbf{v}\times\mathbf{B}\right)\cdot\frac{\partial f}{\partial \mathbf{v}}d\mathbf{v} = -nq\left(\mathbf{E}+\mathbf{u}\times\mathbf{B}\right). \tag{2.21}$$

Finally, the collitional term integrates simply to

$$\int \mathbf{v} \left(\frac{\partial f}{\partial t} \right)_c d\mathbf{v} = \int \mathbf{v} C[f] \tag{2.22}$$

$$= \left(\frac{\partial n\mathbf{u}}{\partial t} \right)_c . \tag{2.23}$$

This term represents the volumetric momentum transfer between the species of interest and any other species (ions, neturals, waves, etc.) with which it interacts. Of course, its actual form depends on the details of $C[f]$.

Combining the above relations and multiplying by the particle mass m yields the equation for conservation of momentum,

$$nm\frac{\partial \mathbf{u}}{\partial t} + nm\mathbf{u} \cdot \frac{\partial \mathbf{u}}{\partial \mathbf{x}} = nq\left(\mathbf{E} + \mathbf{u} \times \mathbf{B}\right) - \frac{\partial p}{\partial \mathbf{x}} + \int \mathbf{v} C[f]. \tag{2.24}$$

We may further take the next moment to derive the conservation of energy law for these fluids. We again split the velocity into the random and averaged components. The first term is

$$\frac{\partial}{\partial t} \int \mathbf{v} \cdot \mathbf{v} f d\mathbf{v} = \frac{\partial}{\partial t} \left[\int \mathbf{v}_r \cdot \mathbf{v}_r f d\mathbf{v} + \mathbf{u} \cdot \int \mathbf{v}_r f d\mathbf{v}_r + \mathbf{u} \cdot \mathbf{u} \int f d\mathbf{v}_r \right] \tag{2.25}$$

$$= \frac{\partial}{\partial t} \left[\frac{3p}{m} + n\mathbf{u} \cdot \mathbf{u} \right] \tag{2.26}$$

The second moment of the spatial derivative is

$$\frac{\partial}{\partial \mathbf{x}} \cdot \int v^2 \mathbf{v} f d\mathbf{v} = \frac{\partial}{\partial \mathbf{x}} \cdot \left[\int v_r^2 \mathbf{v}_r f d\mathbf{v}_r + 3\mathbf{u} \int v_r^2 f d\mathbf{v_r} + 3u^2 \int \mathbf{v}_r f d\mathbf{v}_r + u^2 \mathbf{u} \int f d\mathbf{v}_r \right] \tag{2.27}$$

$$= \frac{\partial}{\partial \mathbf{x}} \cdot \left[\frac{2}{m} (\mathbf{Q} + \frac{5}{2} p\mathbf{u}) + nu^2 \mathbf{u} \right] \tag{2.28}$$

where we have defined the heat flux $Q = \frac{m}{2} \int v_r^2 \mathbf{v}_r f d\mathbf{v}_r$. This term determines the total flux of random, thermal energy. It is contrasted with the next term $\frac{5}{2}p\mathbf{u}$, which represents the thermal energy transported by convection. The final term is simply the bulk energy convection.

The acceleration term can again be integrated by parts. This reads

$$-\frac{q}{m}\int v^2\frac{\partial}{\partial\mathbf{v}}\cdot\left[\mathbf{E}+\mathbf{v}\times\mathbf{B}f\right]d\mathbf{v} = -\mathbf{E}\cdot\int v^2\frac{\partial f}{\partial\mathbf{v}}d\mathbf{v} \tag{2.29}$$

$$= 2\frac{qn}{m}\mathbf{E}\cdot\mathbf{u}. \tag{2.30}$$

Here again, the magnetic field term vanishes in the integration by parts due to the orthogonality of $\mathbf{v}\times\mathbf{B}$ with $\mathbf{v}$ and $\frac{\partial}{\partial\mathbf{v}}$. Here we recover a known property of magnetic fields– namely, they do not impart energy onto a charged particle. The remaining electric field term simply indicates the work done on the species by the field.

Finally, the collision term takes the form,

$$\int v^2 C[f]d\mathbf{v} \equiv -\frac{2}{m}\left(\frac{\partial W}{\partial t}\right)_c, \tag{2.31}$$

and represents the energy lost through the collision operator. We will multiply each term by $\frac{m}{2}$ to find the energy equation,

$$\frac{3}{2}\frac{\partial p}{\partial t}+\frac{\partial}{\partial t}\frac{mnu^2}{2}+\frac{\partial}{\partial\mathbf{x}}\cdot\left(n\frac{mu^2}{2}\mathbf{u}\right) = -\frac{\partial}{\partial\mathbf{x}}\cdot\left(Q+\frac{5}{2}p\right)+qn\mathbf{u}\cdot\mathbf{E}-\left(\frac{\partial W}{\partial t}\right)_c. \tag{2.32}$$

This equation can be simplified significantly by incorporating the continuity equation on the left hand side and the momentum equation to solve for $\mathbf{u}\cdot\mathbf{E}$. The resulting, final energy equation takes the form

$$\frac{3}{2}\left(\frac{\partial nT}{\partial t}+\mathbf{u}\cdot\frac{\partial nT}{\partial \mathbf{x}}\right)+\frac{5}{2}nT\frac{\partial}{\partial \mathbf{x}}\cdot\mathbf{u}=-\frac{\partial}{\partial \mathbf{x}}\cdot\mathbf{Q}+\mathbf{u}\cdot\int\frac{m}{2}\mathbf{v}C[f]d\mathbf{v}-\int\frac{m}{2}\mathbf{v}\cdot\mathbf{v}C[f]d\mathbf{v}. \tag{2.33}$$

While somewhat less intuitive, this equation involves fewer variables and is therefore easier to use. It further incorporates resistive ("ohmic") heating in the term involving the first moment of the collision operator.

While we could in theory continue into an arbitrarily high moment, a fundamental problem has emerged. Namely, given the presence of the term in the kinetic equation involving $\partial f/\partial \mathbf{v}$, each time we take a moment we introduce a term in the resulting equations that involves the *next* moment of f. The continuity equation introduces the momentum term, the momentum equation introduces the temperature, and the energy equation introduces the heat flux. This fundamental fact about the fluid equation introduces the so-called closure problem, whereby for an N-moment model of a fluid there will always be $N+1$ free macroscopic parameters. Solutions to this closure problem involve one of several processes. A convenient approach is to simply truncate the solution, neglecting the next order term entirely. While doing so is extremely convenient, there is typically no physical basis for doing so. Instead, often an external closure model may be applied to approximate the next higher moment. Often, a closure scheme is applied to the heat flux. More on this later.

The collision operator that we have defined is in truth a sum of separate collision operators. These terms may be collisions with electrons, ions, neutrals, or any other species present. We have to separate moments of the collision operator that contribute to the plasma evolution in different ways. We leave this discussion by noting that, while there may be a collision operator between a species and itself in the kinetic equation, this form of collision cannot appear in the higher moments. The simple reason is that, while collisions transfer momentum and energy between particles, they do not add or remove energy or momentum from the entire species. The second moment may be finite in the classical sense with two species present if their temperatures are different. The first moment requires a relative velocity between the two. Indeed, a typical form that this momentum exchange term may take between arbitrary species s and s' is

$$m_s \int \mathbf{v} C_{s,s'} f_s d\mathbf{v} \equiv \mathbf{R}_{s,s'} = -m_s n_s \nu_{s,s'} \left(\mathbf{u}_s - \mathbf{u}_{s'}\right), \tag{2.34}$$

where we have defined $\mathbf{R}_{s,s'}$ as the resistivity between the two species and $\nu_{s,s'}$ as the momentum loss collision frequency. We will incorporate this definition into our analysis of wave-particle interactions in the following section.

Now that we have established the fluid equations and their dependence on the collision operator, we must now determine the form that this operator takes. Typically, a Boltzmann equation or a Fokker-Planck equation is taken here to represent collisions between species. Here, however, we would like to determine an *effective* collision operator based on the presence of waves. To this end, we will break the distribution up into its steady state (or low-frequency) components and its oscillatory, high frequency components. We do so in the following section.

2.2.3 Impact of waves on fluid properties

To understand how oscillations may impact a steady-state distribution function and the derived macroscopic properties, we begin by returning to the kinetic equation and neglecting collisions entirely. This form is traditionally known as the Vlasov equation. We perturb the values $f = f_0 + \tilde{f}$ and $\mathbf{E} = \mathbf{E}_0 + \tilde{\mathbf{E}}$ to find the perturbed Vlasov equation

$$\frac{d(f_0 + \tilde{f})}{d\mathbf{t}} + \mathbf{v} \cdot \frac{d(f_0 + \tilde{f})}{d\mathbf{x}} + \frac{q}{m}\left(\mathbf{E}_0 + \tilde{\mathbf{E}} + \mathbf{v} \times \mathbf{B}\right) \cdot \frac{d(f_0 + \tilde{f})}{d\mathbf{v}} = 0. \tag{2.35}$$

where a subscript 0 indicates a time-averaged value and a tilde represents the perturbation. Assuming a periodic nature of the perturbed quantities allows us to Fourier transform the perturbation as $\left(\tilde{f}, \tilde{\mathbf{E}}\right)(\mathbf{x}, \mathbf{t}) = \int e^{-i\omega t}\left(\tilde{f}, \tilde{\mathbf{E}}\right)(\mathbf{x}, \omega) d\omega$. Here we have assumed a periodic nature in t; however, we will soon see that this value is periodic in $\mathbf{x}$ as well.

After performing this perturbative analysis, we may manipulate Eqn. 2.35 in two ways according to so-called quasilinear theory. In this paradigm, we make two separate assumptions– namely, that the wave propagates according to linear theory but influences the steady-state distribution in a nonlinear sense. To analyze this system, we will analyze the kinetic equation on both timescales. The first method that we will discuss here is taking a phase average of the result, which will allow us to determine the impact of an arbitrary wave on steady-state behavior. Since the perturbations are assumed to be periodic, a phase average negates every term of first order. However, second order terms remain, since the average of a product of two sinusoids is generally finite (but, of course, depends on the relative phase of the sinusoids). The result is

$$\frac{df_0}{dt} + \mathbf{v} \cdot \frac{df_0}{d\mathbf{x}} + \frac{q}{m}\left(\mathbf{E}_0 + \mathbf{v} \times \mathbf{B}\right) \cdot \frac{df_0}{d\mathbf{v}} = -\frac{q}{m}\langle \tilde{\mathbf{E}} \cdot \frac{d\tilde{f}}{d\mathbf{v}} \rangle. \tag{2.36}$$

This result can be correlated to Eqn. 2.5 in that the right hand side (a function solely of oscillating values) implies an effective collision term on the steady state distribution. Indeed, this term can be carried through the fluid equations to determine its impact on each macroscopic value. First, for the continuity equation, we have

$$\frac{-q}{m}\langle \tilde{\mathbf{E}} \cdot \int \frac{\partial \tilde{f}}{\partial \mathbf{v}} \rangle = 0 \tag{2.37}$$

where we have integrated by parts and incorporated the fact that the perturbed distribution function must fall to zero as $\mathbf{v} \to \infty$. Thus, unless the perturbed electric

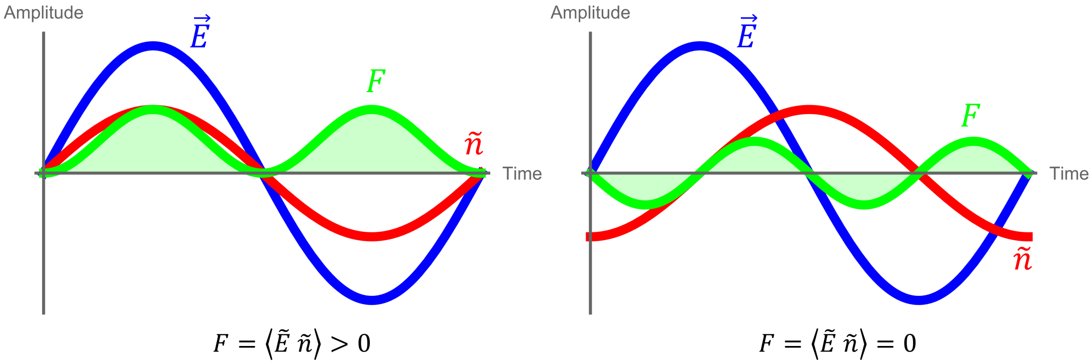

Figure 2.1: Total force imparted on a charged fluid from an oscillating electric field a) in phase and b) out of phase with a number density oscillation.

field is strong enough as to electrostatically separate atoms, the presence of a wave does not affect the total number of the species.

The impact on the momentum equation is less simple. We will return to our definition of resistivity in the preceding section to define the impact on species momentum as an effective resistivity $\mathbf{R}_{eff}$. Finding this moment results in

$$\mathbf{R}_{eff} = -\int q\mathbf{v}\langle \tilde{\mathbf{E}} \cdot \frac{\partial \tilde{f}}{\partial \mathbf{v}} \rangle d\mathbf{v} = q\langle \tilde{n}\tilde{\mathbf{E}} \rangle. \tag{2.38}$$

Equation 2.38 presents the effect of an instability on the momentum of a fluid species. We find that it is not strictly the magnitude of the electric field that influences this value, but the phase average between the electric field and number density. While we arrived at this result from a study of kinetics, there is a physical intuition that may be understood from it as well. Indeed, in the absence of other forces, an oscillating electric field will impart zero force on a single charged particle in a phase-averaged sense. However, when a wave of the same frequency is present in number density as well, the volumetric force may be finite. Figure 2.1 illustrates this principle.

We may define the phase average in either space or time, and ultimately this choice is arbitrary. Since we have already discussed the periodicity in time, we will define a temporal phase average as

$$\langle y\rangle = \lim_{T\to\infty}\frac{1}{T}\int\limits_{-T/2}^{T/2} y(t)dt. \tag{2.39}$$

We can evaluate the product in 2.38 by again assuming that $\tilde{\mathbf{E}}$ and $\tilde{n}$ vary periodically and taking their Fourier transform,

$$\langle \tilde{\mathbf{E}(t)}\tilde{n}(t)\rangle = \mathrm{Re}\left[\lim_{T\to\infty}\frac{1}{T}\int\limits_{-T/2}^{T/2}\int\limits_{-\infty}^{\infty}\tilde{\mathbf{E}}(\omega)e^{i\omega_1 t}d\omega_1\int\limits_{-\infty}^{\infty}\tilde{n}(\omega)e^{i\omega_2 t}d\omega_2 dt\right] \tag{2.40}$$

where we have defined the Fourier components $\tilde{\mathbf{E}}(\omega)$ and $\tilde{n}(\omega)$. Given the orthogonality of complex exponents,

$$\mathrm{Re}\left[\lim_{T\to\infty}\frac{1}{T}\int\limits_{-T/2}^{T/2}\tilde{a}e^{i\omega_1 t}\tilde{b}e^{i\omega_2 t}dt\right] = \frac{1}{2}\mathrm{Re}\left[\tilde{a}\tilde{b}\right]\delta(\omega_1,\omega_2) \tag{2.41}$$

we may let $\omega = \omega_1 = \omega_2$ to simplify as

$$\langle \tilde{\mathbf{E}(t)}\tilde{n}(t)\rangle = \frac{1}{4\pi}\int\limits_{-\infty}^{\infty}\tilde{\mathbf{E}}\tilde{n}d\omega \tag{2.42}$$

$$= \frac{1}{2}\int\limits_{-\infty}^{\infty}\mathrm{Re}\left[\tilde{\mathbf{E}}\tilde{n}\right]d\omega. \tag{2.43}$$

$$= \frac{q}{2}\int\limits_{-\infty}^{\infty}\mathbf{k}\mathrm{Im}\left[\tilde{\phi}\tilde{n}\right]d\omega. \tag{2.44}$$

We have thus found an equation that relates the oscillating electric field and number density present in a wave to a term in the momentum equation for the steady-state values. We may further determine the impact on energy transfer by finding the second moment. These can be found to be [20]

$$-\langle \int (\mathbf{v}\cdot\mathbf{v})\tilde{\mathbf{E}}\frac{\partial \tilde{f}}{\partial \mathbf{v}}\rangle = nq\langle \tilde{\mathbf{E}}\cdot\tilde{\mathbf{u}}\rangle + q\mathbf{u}\cdot\langle\tilde{\mathbf{E}}\tilde{n}\rangle. \tag{2.45}$$

$$= n_0 q \int_{-\infty}^{\infty} \mathbf{k}\cdot \mathrm{Im}\left[\tilde{\phi}\tilde{\mathbf{u}}\right] d\omega + \frac{q}{2}\mathbf{u}\cdot \int_{-\infty}^{\infty} \mathbf{k}\mathrm{Im}\left[\tilde{\phi}\tilde{n}\right] d\omega., \tag{2.46}$$

where we have defined $\tilde{\mathbf{u}}$ as the perturbed velocity, $\tilde{\mathbf{u}} = \int \mathbf{v}\tilde{f}d\mathbf{v}$. The final wave-driven term in the energy equation is the Ohmic heating term, which takes the form

$$\mathbf{R}_{eff}\cdot\mathbf{u} = q\mathbf{u}\cdot\langle\tilde{\mathbf{E}}\tilde{n}\rangle. \tag{2.47}$$

Taken together, the energy equation including wave terms is

$$\frac{3}{2}\left(\frac{\partial nT}{\partial t} + \mathbf{u}\cdot\frac{\partial nT}{\partial \mathbf{x}}\right) + \frac{5}{2}nT\frac{\partial}{\partial \mathbf{x}}\cdot\mathbf{u} = -\frac{\partial}{\partial \mathbf{x}}\cdot\mathbf{Q} + nq\langle\tilde{\mathbf{E}}\cdot\tilde{\mathbf{u}}\rangle \tag{2.48}$$

The values in all of these relations depend on the oscillating quantities $\tilde{n}$, $\tilde{\mathbf{u}}$ and $\tilde{\mathbf{E}}$. However, these quantities are prohibitively difficult to directly measure simultaneously. As we will see in Chap. III, however, measuring the magnitude of $\tilde{n}$ is entirely possible. Therefore, we now require a mathematical relation between $\tilde{n}$, $\tilde{\mathbf{u}}$, and $\tilde{\mathbf{E}}$ to be able to fully evaluate the effect of waves. To this end, we may return to Eqn. 2.35 but apply a different analysis. Namely, instead of taking the phase average, we will neglect higher order terms and analyze f_1 and $\mathbf{E}_1$ directly. Doing so, combined with the introduction of Gauss' law, will provide the dispersion relation and the relations we require.

2.2.4 The dispersion relation

The oscillating electric field and number density may be directly related by Gauss' law:

$$\nabla \cdot \mathbf{E} = \frac{\rho}{\epsilon_0}, \tag{2.49}$$

where $\rho = e\sum_s n_s Z_s$ is the charge density, with Z_s the charge state of species s. Next, we again perturb the number density and electric field as $n_s = n_{0,s} + \tilde{n}_s(\mathbf{x}, t)$, where n_0 is the time-averaged value. Assuming a periodic nature of the perturbed quantities allows us to Fourier transform the perturbation as $\tilde{n}(\mathbf{x}, \mathbf{t} = \int e^{-i\omega t}\tilde{n}(\mathbf{x}, \omega)d\omega$. The resulting Gauss' law becomes

$$\nabla \cdot \mathbf{E}_0 + \mathbf{k} \cdot \int e^{-i\omega t}\tilde{\mathbf{E}}(\mathbf{x}, \omega)dt = \frac{1}{\epsilon_0}\sum_s q_s \left(n_{s,0} + \int e^{i\mathbf{k}\cdot\mathbf{x}}\tilde{n}_s(\mathbf{x}, \omega)d\omega \right). \tag{2.50}$$

It is important to note that the components of the Fourier transform are orthogonal (i.e. linearly independent). This fact allows us to separate Gauss' law into an individual equation for *each* component of the integral and one for the steady state, since there are no higher order terms. Namely,

$$\nabla \cdot \mathbf{E}_0 = \frac{1}{\epsilon_0}\sum_s q_s n_{0,s} \tag{2.51}$$

$$i\mathbf{k} \cdot \tilde{\mathbf{E}}(\mathbf{x}, \omega) = \frac{1}{\epsilon_0}\sum_s q_s \tilde{n}_s(\mathbf{x}, \omega). \tag{2.52}$$

We now rearrange Eqn. 2.52 to define the dispersion relation:

$$1 - \frac{1}{\epsilon_0}\sum_s \frac{q_s \tilde{n}_s}{i\mathbf{k} \cdot \tilde{\mathbf{E}}} = 0 \tag{2.53}$$

$$1 + \sum_s \chi_s = 0, \tag{2.54}$$

where we have defined

$$\chi_s \equiv \frac{iq_s\tilde{n}_s}{\epsilon_0\mathbf{k}\cdot\tilde{\mathbf{E}}} \tag{2.55}$$

as the susceptibility of species s. Finding this value provides a relation between $\tilde{n}_s$ and $\tilde{\mathbf{E}}$, which is required to determine effective resistivity. The value of χ_s can be determined once the nature of the specific wave has been determined. Indeed, there are many different susceptibility values that depend on the details of the plasma background. To determine the value of χ_s applicable to our plasma, we must first define the expected plasma properties and find a theory that describes the waves therein.

2.2.5 Effective collision frequency

With a full description of the general properties of waves on a plasma from a quasilinear perspective, we now introduce the concept of an effective (or, commonly, "anomalous") collision frequency, following the analysis of Ref. [34]. We first assume that the plasma in question is made up solely of electrons and singly-charged ions with a dispersion relation of

$$1 + \chi_e + \chi_i = 0. \tag{2.56}$$

Since the susceptibilities are in general complex functions, we immediately find the identity

$$\mathrm{Im}(\chi_i) = -\mathrm{Im}(\chi_e). \tag{2.57}$$

We may further use the definition of the susceptibility to redefine the effective resistivity on species s as [34]

$$R_{eff,s} = \int_{-\infty}^{\infty} \mathbf{k}\epsilon_0 \tilde{E}^2 \mathrm{Im}\left[\chi_s\right] d\omega \tag{2.58}$$

$$= \frac{q^2}{\epsilon_0} \int \frac{\mathbf{k}}{k^2} \tilde{n}_s^2 \mathrm{Im}\left(\chi_s^{-1}\right) d\omega. \tag{2.59}$$

Given Eqn. 2.57, we see that the effective resistivity of the ions is the negative that of the electrons, implying that the waves act to mediate a resistivity between the two species. For this reason, we may model the resistivity with an analogy to classical effects,

$$\mathbf{R}_{eff,e} = -m_e n_{e,0} \nu_{eff} \left(\mathbf{u}_{e,0} - \mathbf{u}_{i,0}\right) \tag{2.60}$$

where we have defined an effective collision frequency ν_{eff} as the characteristic frequency of momentum transfer. Forming this definition assists the analysis in two ways. First, it enables us to compare the wave-driven effects to classical collisions more directly. Classical collisions have been studied extensively and are known to follow Spitzer scaling [105] with an electron-ion collision frequency equal to

$$\nu_{e,i} = 2.18 \times 10^{-11} \frac{n_e}{T_e^{3/2}} \tag{2.61}$$

for xenon ions, where n_e is in m^{-3} and T_e is in eV. Moreover, the definition of a collision frequency based on wave interactions justifies its use in a Fourier law of heat conduction. In the next section, we will describe how this process functions in more detail.

So far we have established a local model for how a wave may impact plasma parameters. However, the question of the thermodynamics of these systems takes on a more global character. To this end, to complete our discussion of the expansion, we

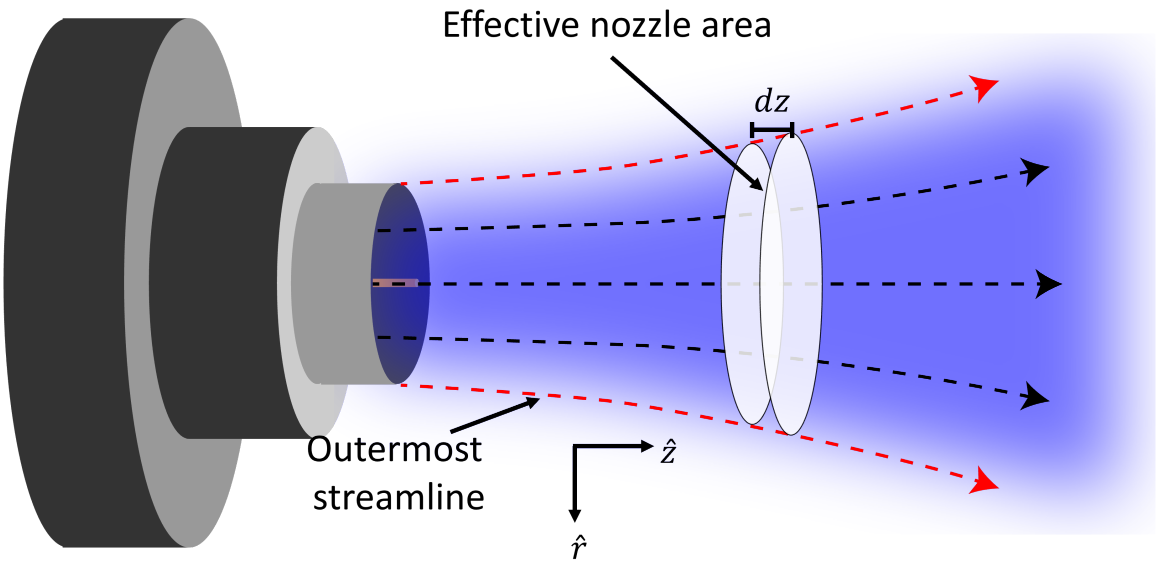

Figure 2.2: Illustration of the quasi-one dimensional magnetic nozzle model.

will transition to a quasi-one dimensional model to determine the global expansion parameters.

2.2.6 Quasi one-dimensional model

To better understand the global characteristics of the expansion process, we will first convert the fluid equations derived in the previous section to a quasi-one dimensional, or "paraxial" format. These types of models take averages over axial slices of a given area and are common in conventional nozzle physics [8]. Moreover, this analysis has been performed previously on magnetic nozzles as well with experimentally-verified results [78, 75, 103, 7]. Such a model is thus ideal for an understanding of how the plasma evolves and for better understanding the impact of waves on thruster operation.

In this paradigm, we will define the area A as the area enclosed by the outermost magnetic field lines that intersect the thruster exit plane. We are therefore assuming that electrons do not expand faster than the magnetic fields, and that this streamtube encloses all relevant particle flux. In this way, we are able to ignore any gradients in $\hat{r}$, focusing instead on the characteristics in $\hat{z}$, which are the relevant ones for thrust production. Figure. 2.2 illustrates this view.

To find the proper paraxial energy equation, we will integrate Eqn. 2.48 over a volume bounded by two nozzle areas separated by a small distance dz (c.f. Fig. 2.2). As we take the limit as $dz \to 0$, we find the corresponding substitutions $\nabla X \to X'$ and $\nabla \cdot \mathbf{X} \to (XA)'$, where the prime indicates d/dz. We further replace each plasma property with its area-averaged equivalent, $\overline{X} = \frac{1}{A}\int_A X dA'$. The steady-state continuity equation in this paradigm is

$$(\overline{n}\overline{u}A)' = 0 \tag{2.62}$$

and the energy equation is

$$0 = \frac{3}{2}\overline{u}A(\overline{n}\overline{T})' + \frac{5}{2}\overline{n}\overline{T}(\overline{u_z}A)' + (\overline{Q}A)' - q\overline{n}A\overline{\langle\tilde{\mathbf{E}}\cdot\tilde{\mathbf{u}}\rangle} \tag{2.63}$$

While these equations are generalized to an arbitrary species, we will now specify them to describe the electrons. We will understand Eqn. 2.63 by taking three simplifying limits. We will begin by taking the simplest case, where all heat flux and heating terms are zero, resulting in adiabatic flow. The resulting energy equation is

$$\begin{aligned} 0 &= uA(nT)' + \frac{5}{3}nT(uA)' && (2.64)\\ &= nT' - \frac{2}{3}n'T && (2.65)\\ & && (2.66) \end{aligned}$$

where we have used continuity to substitute $n(uA)' \to -uAn'$. We can integrate the final result from an upstream condition (subscript 0) to a final condition (subscript

f) to find

$$\frac{T_f}{n_f^{\gamma-1}} = \frac{T_0}{n_0^{\gamma-1}} \tag{2.67}$$

where we have defined the polytropic index γ to be 5/3 in the ideal case. As discussed in Chap. I, this value is the subject of ongoing research in these expanding plasmas. It is often measured in these systems using Eqn. 2.67 or the local equivalent [7],

$$\left(\frac{T_e}{n_e^{\gamma-1}}\right)' = 0. \tag{2.68}$$

However, experimental findings of this value rarely take the adiabatic value of 5/3 [28, 116, 75, 126]. In fact, it is often closer to the so-called isothermal limit of $\gamma = 1$, where any temperature gradients are instantly smoothed out. The reason for this trend is a subject of ongoing research. We will attempt to explain this phenomenon by relaxing the adiabatic assumption and including either the heat flux or the wave heating terms. First, we will discuss the possibility of a wave-driven heat flux that assumes a Fourier law.

2.2.7 Finite heat flux assuming a Fourier law

The basis for this analysis is the quasi-one dimensional energy equation ignoring only wave heating terms. This takes the form

$$0 = \frac{3}{2}uA(nT)' - \frac{5}{2}n'TuA + (QA)' \tag{2.69}$$

where we have again used the continuity equation to substitute $n(uA)' = -n'uA$. We then make a few assumptions. First, we take a Fourier law for the heat flux. The most general form of a Fourier law is

$$Q = -\kappa \nabla T \tag{2.70}$$

where κ is the thermal conductivity. This form is used extensively in physics of solids, where κ is typically an experimentally determined value for a given material. In gases, a similar form was first discovered independently by Sydney Chapman and David Enskogg [24]. This process involved perturbing the collisionless Boltzmann equation and performing an expansion on the Boltzmann collision operator in terms of Laguerre polynomials. This theory was then applied to a plasma by Braginskii [17], who found an applicable thermal conductivity invoking electron-electron collisions as

$$\kappa_{e,e} = 3.2 \frac{n_e T_e}{m_e \nu_e}. \tag{2.71}$$

Here, the coefficient 3.2 depends on the details of the derivation and the assumptions therein. For our purposes, we will abstract this parameter as a value α and leave the discussion of its value for Chap. V. Doing so yields the Fourier law that we will implement throughout this work,

$$q = -\frac{\alpha n T T'}{m \nu_{eff}}. \tag{2.72}$$

We further assume a polytropic law to substitute for number density,

$$n = n_0 \left(\frac{T}{T_0} \right)^{\frac{1}{\gamma - 1}}, \tag{2.73}$$

where we take γ to be constant. By substituting the Fourier and polytropic laws into the energy equation, we can solve directly for the value of γ that we predict:

$$\gamma = 1 + \frac{\frac{m_e u_e \nu_e}{\alpha T_e} + \frac{T_e'}{T_e}}{\frac{3}{2}\frac{m_e u_e \nu_e}{\alpha T_e} - \frac{A'}{A} - \frac{T_e'}{T_e} + \frac{\nu_e'}{\nu_e} - \frac{T_e''}{T_e'}}. \tag{2.74}$$

There are several interesting aspects to elucidate from Eqn. 2.74. First, each term except for the first in both the numerator and denominator involve the normalized rate of change of the various properties. Notably, these terms do not depend on the magnitude of each value– including the collision frequency. If we hypothetically scaled the collision frequency arbitrarily low such that the first term in both numerator and denominator vanished, the collision frequency *profile* could still be significant. It was exactly this fact that was observed in Ref. [75]. In this prior work, the magnitude of the collision frequency was assumed (and, later, measured) to be extremely low. Indeed, in a typical magnetic nozzle the classical collision frequency is often vanishing. However, the relative value of the ratio ν_c'/ν_c remained a significant, and the applied scaling (using the Spitzer scaling for Coulomb collisions, Eqn. 2.61 with Argon) predicted γ to within a few percent. However, as mentioned in Chap. I, the prediction for the heat flux magnitude was too high.

Given that the Fourier law scaling with classical collisions predicted γ accurately but that the collisions themselves were too infrequent, we posit that a Fourier law with wave-driven, effective collisions may accurately describe the electron expansion. However, it is also possible that the other terms in Eqn. 2.63 may be significant. To this end, we now proceed to discuss the values of these terms.

2.2.8 Wave heating

We now neglect the heat flux and analyze the wave heating terms in Eqn. 2.63. This method is an example of an alternative closure scheme for the fluid equations. While the Fourier law assumption provides an analytical form for the next moment (i.e. the heat flux), this method ignores it and focuses instead on the other second-moment terms.

After again replacing the number density with a polytropic law, we recover the following equation for γ:

$$n_0 \left(\gamma - \frac{5}{3}\right) A \left(\frac{T}{T_0}\right)^{\frac{1}{\gamma-1}} uT' = \frac{2}{3}\left(\gamma - 1\right)\left(-q\overline{n}A\overline{\langle\tilde{\mathbf{E}}\cdot\tilde{\mathbf{u}}\rangle} + \bar{\mathbf{u}}\cdot\overline{\langle\tilde{\mathbf{E}}\tilde{n}\rangle}\right). \qquad (2.75)$$

Here we have defined n_0 and T_0 as the initial condition for number density and temperature, which we will take in Chap. V to be the value at the most upstream measurement. Equation 2.75 presents a transcendental equation for γ that must be solved numerically. However, two important limits emerge. In this case, if wave heating is zero, γ must again take its adiabatic value of 5/3 for the left hand side to be zero. Moreover, if it heating dominates γ will approach unity. Thus, the presence of this wave heating serves to push the electron plasma away from adiabaticity.

Both of these mechanisms show possible means for waves to affect electron thermodynamics in these systems. We will explore both of these possibilities in Chap. V and further discuss in more detail their impacts on thruster performance. In the following section, we will determine the values of the phase-averaged terms determined in this section through deriving the lower hybrid drift instability.

2.2.9 Lower hybrid drift instability

To determine the values of the phase-averaged values and χ_s, we will make several assumptions to describe the plasma:

- Ions are cold and unmagnetized.
- There are negligible multiply-charged ions
- Electrons are warm and experience cross-field drifts from the pressure and plasma potential gradients.

- The Larmor radius of the electrons is comparable to the wavelengths that we are interrogating.
- The magnetic field is uniform.
- Classical collisions are insignificant.

With these assumptions, we may investigate a form of the lower hybrid drift instability (LHDI). The LHDI has been discussed in the context of a multitude of laboratory plasmas, including magnetic nozzles [92]. It is common in plasmas in which the ions are cold and unmagnetized but the electrons are warm and magnetized. When a cross-field electron pressure gradient is present, a diamagnetic current forms and may drive this mode unstable. We present here the derivation of this mode from first principles to inform our data processing in later chapters.

This derivation is based on Ref. [22]. We assume that the wave is localized, meaning that the wavelength is much smaller than the number density gradient scale length, $n_e/|\nabla n_e|$. This allows us to treat these these values as constant on this scale so that the wave does not change character over a single oscillation. We will take a slab model with gradients in x, current in y, and magnetic field in z.

We will further simplify our analysis by using the reference frame moving with the electron $E \times B$ drift, i.e. $-E_0/B_0$. In this frame, the electric field is zero. Intuitively, if there were an electric field in this frame of reference the electrons would maintain some $E \times B$ drift, which is impossible by definition. Mathematically, this results from a Lorentz transformation:

$$\mathbf{E}'_\perp = \gamma_r \left(\mathbf{E}_\perp + \mathbf{v} \times \mathbf{B} \right), \tag{2.76}$$

where γ_r is the relativistic Lorentz factor. If we let $v = -E/B$, the term in parentheses becomes zero. Thus, in this reference frame, the electrons have no net bulk velocity, but the ions move with speed $u_i = E_0/B_0$ in the $+y$ direction.

We will assume the steady-state electron distribution function to be

$$f_{e,0} = \frac{n(X)}{\pi^{3/2} v_{\mathrm{th},e}^3} \exp\left(-\frac{v_x^2 + v_y^2 + v_z^2}{v_{\mathrm{th},e}^2}\right), \tag{2.77}$$

where $X = x - \frac{v_y}{\Omega_e}$. This is a common assumption in systems with a cross-field number density gradient and fulfills the steady state Vlasov equation with an average velocity equal to the electron diamagnetic drift. Fundamentally, we are saying that $f_{e,0}$ is a Maxwellian distribution where each particle is "counted" at the center of its gyro orbit, since X is the orbital center of a particle at instantaneous position x with velocity v_y. We can Taylor expand $n(x_0 - \frac{v_y}{\omega_e})$ around x_0 as $n(x) \approx n(x_0) - \frac{\partial n}{\partial x}\frac{v_y}{\Omega_e}$. Thus, the electron distribution function can further reduced with the approximation $r_L << 1/\nabla n_e$ as

$$f_{e,0} = \frac{n_0}{\pi^{3/2} v_{th,e}^3} \exp\left(-\frac{v_\perp^2 + v_z^2}{v_{th,e^2}}\right)\left(1 - \epsilon_n \frac{v_y}{\Omega_{c,e}}\right) \tag{2.78}$$

$$= \left(1 - \epsilon_n \frac{v_y}{\Omega_{c,e}}\right), f_M \tag{2.79}$$

where $\epsilon_n = \frac{1}{n_0}\frac{\partial n}{\partial x}$ is the inverse of the density gradient scale length and we have defined the Maxwellian distribution $f_M = \frac{n_0}{\pi^{3/2} v_{th,e}^3} \exp\left(-\frac{v_x^2+v_y^2+v_z^2}{v_{th,e^2}}\right)$, with $v_{th,e} = \sqrt{2T_e/m_e}$ as the thermal speed of the electrons.

Now that we have defined a steady-state distribution function, we can move to find an expression for the number density oscillation magnitude. To this end, we will integrate along unperturbed orbits using the method of characteristics [108, 107]. This process is relatively common in kinetic wave theory with magnetized particles and involves integrating the perturbed distribution function in phase space. To do so, we need to find an expression for the total derivative of f along this unperturbed orbit. As we have previously noted, the kinetic equation defines exactly this derivative. Moreover, in a linear sense, we can apply a kinetic equation to both the perturbed and steady-state terms of f. We thus have, in the collisionless case,

$$\frac{df_0}{dt} = \frac{\partial f_0}{\partial t} + \mathbf{v} \cdot \frac{\partial f_0}{\partial \mathbf{x}} + \frac{q}{m} \left(\mathbf{v} \times \mathbf{B}\right) \cdot \frac{\partial f_0}{\partial \mathbf{v}} = 0 \tag{2.80}$$

$$\frac{df}{dt} = \frac{\partial f}{\partial t} + \mathbf{v} \cdot \frac{\partial f}{\partial \mathbf{x}} + \frac{q}{m} \left(\tilde{\mathbf{E}} + \mathbf{v} \times \mathbf{B}\right) \cdot \frac{\partial f}{\partial \mathbf{v}} = 0, \tag{2.81}$$

where we recall that these equations apply in a reference frame with zero steady-state electric field. We may consider Eqn. 2.80 an operator on an arbitrary distribution function,

$$\left.\frac{d}{dt}\right|_0 = \mathbf{v} \cdot \frac{\partial}{\partial \mathbf{x}} + \frac{q}{m} \left(\mathbf{v} \times \mathbf{B}\right) \cdot \frac{\partial}{\partial \mathbf{v}}. \tag{2.82}$$

Applying Eqn. 2.82 to the steady state distribution function results in the Vlasvo equation. However, since the Vlasov equation is by definition a derivative along the phase-space trajectory of a particle, we see that applying this operator to *any* function will take its derivative along these *unperturbed* orbits. We can thus apply this operator to the total distribution function as

$$\left.\frac{df}{dt}\right|_0 = \frac{\partial f}{\partial t} + \mathbf{v} \cdot \frac{\partial f}{\partial \mathbf{x}} + \frac{q}{m} \left(\mathbf{v} \times \mathbf{B}\right) \cdot \frac{\partial f}{\partial \mathbf{v}} \tag{2.83}$$

$$\left.\frac{d\tilde{f}}{dt}\right|_0 = -\frac{q}{m} \tilde{\mathbf{E}} \cdot \frac{\partial f_0}{\partial \mathbf{v}}, \tag{2.84}$$

where in the final step we have substituted $-\frac{q}{m}\tilde{\mathbf{E}} \cdot \frac{\partial f_0}{\partial \mathbf{v}}$ for the right hand side using Eqn. 2.81 and used the fact that $\left.\frac{df_0}{dt}\right|_0 = 0$ from Eqn. 2.80.

We now have a form for the derivative of the perturbed function along unperturbed orbits. To find a form for $\tilde{f}$, we need only integrate Eqn. 2.84 along this trajectory. To this end, we will apply the method of characteristics. We first apply the electrostatic assumption to substitute $\tilde{\mathbf{E}} = -\frac{\partial}{\partial \mathbf{x}}\tilde{\phi}$ and our assumed f_0 (Eqn. 2.79) to find

$$\tilde{f} = \frac{q}{m}\int_{-\infty}^{t} \frac{\partial \tilde{\phi}}{\partial \mathbf{x}} \cdot \frac{\partial f_0}{\partial \mathbf{v}} dt \tag{2.85}$$

$$= \frac{q}{m}\int_{-\infty}^{t} -\frac{2 f_M}{v_{t,e}^2}\mathbf{v} \cdot \frac{\partial \tilde{\phi}}{\partial \mathbf{x}} + \frac{\epsilon_n f_M}{\Omega_e}\frac{\partial \tilde{\phi}}{\partial y} dt. \tag{2.86}$$

Since the plasma potential does not depend on velocity, we may use its total derivative to substitute $\mathbf{v} \cdot \frac{\partial \tilde{\phi}}{\partial \mathbf{x}} = \frac{d\tilde{\phi}}{dt'} - \frac{\partial \tilde{\phi}}{\partial t'}$. We may then replace the spatial derivative in y with $i\mathbf{k}$. Making these substitutions gives

$$\tilde{f} = \frac{q}{m}\int_{-\infty}^{t} -2\frac{f_M}{v_{t,e}^2}\left(\frac{d\tilde{\phi}}{dt} - \frac{\partial \tilde{\phi}}{\partial t}\right) + \frac{ik_y f_M}{\Omega_e}\tilde{\phi} dt' \tag{2.87}$$

$$= -\frac{2q}{m}\frac{f_M}{v_{t,e}^2}\phi(t) + \frac{2q}{m}\frac{f_M}{v_{t,e}^2}\int_{-\infty}^{t}\frac{\partial \tilde{\phi}}{\partial t'}dt' + \frac{ik_y q \epsilon_n}{m\Omega_e} f_M \int_{-\infty}^{t} \phi dt'. \tag{2.88}$$

Here we have also assumed that $\lim_{t\to-\infty}\tilde{\phi} = 0$. We now have the problem of evaluating these two integrals. We can revisit our assumption that the perturbed quantity $\tilde{\phi}(t) = \int \tilde{\phi}(i\mathbf{k}\cdot\mathbf{x}' - i\omega t)$, with which we need only solve for the position coordinate. For this purpose, we need to define the exact unperturbed orbits in this scenario. These can be readily defined by the magnetic force acting on the particles,

$$\frac{d\mathbf{v}'}{dt} = \frac{q}{m}\mathbf{v}' \times \mathbf{B} \tag{2.89}$$

$$\frac{d\mathbf{r}'}{dt} = \mathbf{v}', \tag{2.90}$$

where the prime indicates a value in the integrand. We may then integrate these to find the position coordinates,

$$x' = \frac{v_\perp}{\Omega_e}\sin(\varphi + \Omega_e\tau) - \frac{v_\perp}{\Omega_e}\sin(\varphi) \tag{2.91}$$

$$y' = \frac{v_\perp}{\Omega_e}\cos(\varphi + \Omega_e\tau) - \frac{v_\perp}{\Omega_e}\cos\varphi \tag{2.92}$$

$$z' = -v_\parallel \tau, \tag{2.93}$$

where $\tau = t' - t$ and φ is a phase offset based on the initial position. In defining these in this way, we have arbitrarily assumed that $x(t) = y(t) = 0$, which is fine since the time derivatives operate on t', so t can be treated as a constant. These definitions can be used in the distribution function integral to find the total perturbed distribution function as

$$\tilde{f}_e = -\frac{2q\widetilde{\phi}}{m}\frac{f_{\mathrm{M}}}{v_{\mathrm{th},e}^2}\left[1 + i\left(\omega - k_y v_{D,e}\right)\right. \tag{2.94}$$

$$\times \int\limits_0^\infty d\tau \exp\left(-i\left(\frac{k_\perp v_\perp}{\Omega_e}\left(\cos\left(\varphi + \Omega_e\tau\right) - \cos\varphi\right)\right)\right. \tag{2.95}$$

$$\left. + \left(\omega - k_\parallel v_\parallel\right)\tau\right)\Big] \,. \tag{2.96}$$

We may now apply the following two identities to relate this function to Bessel functions,

$$\exp(iz\sin\varphi) = \sum_{n=-\infty}^{\infty} \exp(in\varphi) J_n(z) \tag{2.97}$$

$$\exp(iz\sin(\varphi + \Omega_e\tau)) = \sum_{n=-\infty}^{\infty} \exp(im(\varphi + \Omega_e\tau)) J_n(z), \tag{2.98}$$

where we have introduced J_n as the Bessel function of the first kind of order n. These substitutions yield the final perturbed electron distribution function

$$\begin{aligned}\tilde{f}_e = &-\frac{2q}{m}\frac{n_0}{\pi^{3/2}v_{t,e}^5}\exp\left(-\frac{v_\perp^2+v_\parallel^2}{v_{t,e}^2}\right)\tilde{\phi}\,[1-(\omega-k_y v_{D,e})\dots \\ &\times\sum_{m,n}\left(\frac{J_n(\frac{k_\theta v_\perp}{\Omega_e})J_m(\frac{k_\theta v_\perp}{\Omega_e})\exp(i(m-n)(\varphi-\pi/2))}{\omega-k_\parallel v_\parallel-m\Omega_e}\right)\Bigg].\end{aligned} \tag{2.99}$$

With Eqn. 2.99, we are finally ready to find the moments $\tilde{n}$ and $\tilde{\mathbf{v}}$, which will both be in terms of $\tilde{\phi}$. The perturbed number density is thus

$$\begin{aligned}\tilde{n} &= \int \tilde{f}_e d\mathbf{v} = \int\limits_0^\infty v_\perp \int\limits_{-\infty}^\infty \int\limits_0^{2\pi} \tilde{f}_e d\phi dv_\parallel dv_\perp \\ &= -\frac{2qn_0}{mv_{t,e}^2}\tilde{\phi}\left(1+(\omega-k_y v_{D,e})\sum_{m,n}\int\limits_0^\infty v_\perp J_n\left(\frac{k_\theta v_\perp}{\Omega_e}\right)J_m\left(\frac{k_\theta v_\perp}{\Omega_e}\right)\exp\left(-\frac{v_\perp^2}{v_{t,e}^2}\right)dv_\perp\right. \\ &\left.\times\int\limits_{-\infty}^\infty\frac{\exp\left(-\frac{v_\parallel^2}{v_{t,e}^2}\right)}{\omega-k_\parallel v_\parallel-m\Omega_e}dv_\parallel\int\limits_0^{2\pi}\exp\left[i(m-n)(\varphi-\pi/2)\right]d\varphi\right).\end{aligned} \tag{2.100}$$

The integral over phase is an average of first order sinusoids over one period, which is be zero for all $m \neq n$. We next recognize the integral in $v_\parallel$ as the plasma dispersion function, defined as [44]

$$Z(\zeta) = \pi^{-1/2}\int\limits_{-\infty}^{\infty}\frac{e^{-t^2}}{t-\zeta}dt. \tag{2.101}$$

Using this definition, the parallel integral can be simplified to

$$\int\limits_{-\infty}^{\infty}\frac{\exp\left(-\frac{v_\parallel^2}{v_{t,e}^2}\right)}{\omega-k_\parallel v_\parallel-m\Omega_e}dv_\parallel = Z\left(\frac{\omega-m\Omega_e}{k_\parallel v_{t,e}}\right). \tag{2.102}$$

To evaluate the integral in perpendicular velocity, we may use the following relation [123]:

$$\int_0^\infty x \exp(-ax^2) J_n^2(bx)\, dx = \frac{1}{2a} \exp\left(-\frac{b^2}{2a}\right) I_n\left(\frac{b^2}{2a}\right). \tag{2.103}$$

We apply this formula to the integral in perpendicular velocity, which yields

$$\int_0^\infty v_\perp J_n^2\left(\frac{k_\theta v_\perp}{\Omega_e}\right) \exp\left(-\frac{v_\perp^2}{v_{t,e}^2}\right) dv_\perp = \frac{1}{2} \exp\left(-\frac{k_\theta^2 v_{t,e}^2}{2\Omega_e^2}\right) I_n\left(\frac{k_\theta^2 v_{t,e}^2}{2\Omega_e^2}\right), \tag{2.104}$$

where I_n is a modified Bessel function of the first kind. Finally, we note that the frequencies we are seeking in the LHDI are much less than $\Omega_{c,e}$. Looking at Eqn. 2.102, we note that this is only possible if $m = 0$, so we will only keep this term in the perturbed number density. We find as the final form of the number density perturbation,

$$\tilde{n}_e = \frac{-2qn_0}{mv_{t,e}^2} \tilde{\phi} \left(1 + \frac{\omega - k_y v_{D,e}}{2k_\parallel v_{t,e}} Z\left(\frac{\omega}{k_\parallel v_{t,e}}\right) \exp\left(-\frac{k_\theta^2 v_{t,e}^2}{2\Omega_{c,e}^2}\right) I_n\left(\frac{k_\theta^2 v_{t,e}^2}{2\Omega_{c,e}^2}\right).\right) \tag{2.105}$$

We now move to evaluate the perturbed velocity. First, we will take the perturbed parallel velocity $\tilde{v}_\parallel$. We make use of the derivative of the plasma dispersion function,

$$Z'(\zeta) = -\pi^{-1/2} \int_{-\infty}^\infty \frac{2t}{t - \zeta} e^{-t^2} dt \tag{2.106}$$

to find the integral involving the parallel velocity to be

$$\int_{-\infty}^\infty \frac{v_\parallel \exp\left(-\frac{v_\parallel^2}{v_{t,e}^2}\right)}{\omega - k_\parallel v_\parallel - m\Omega_e} dv_\parallel = -\frac{1}{2} Z'\left(\frac{\omega - m\Omega_e}{k_\parallel v_{t,e}}\right). \tag{2.107}$$

The rest of the integration is the same as for $\tilde{n}_e$, giving us

$$\tilde{u}_\parallel = \frac{-2q\tilde{\phi}}{mv_{t,e}^2}\left(\frac{\omega - k_y v_{D,e}}{k_\parallel} Z'\left(\frac{\omega}{k_\parallel v_{t,e}}\right)\exp\left(-\frac{k_\theta^2 v_{t,e}^2}{2\Omega_{c,e}^2}\right) I_0\left(\frac{k_\theta^2 v_{t,e}^2}{2\Omega_{c,e}^2}\right)\right). \tag{2.108}$$

The components along v_x and v_y are zero. To understand why, we must return the perpendicular integral in Eqn. 2.105 to its equivalent integration along v_x and v_y. Taking the moment in v_x as an example, we find

$$\int_{-\infty}^{\infty}\int_{-\infty}^{\infty} v_x \exp\left(-\frac{v_x^2}{v_{t,e}^2}\right)\exp\left(-\frac{v_y^2}{v_{t,e}^2}\right) J_0^2\left(\frac{k_y}{\Omega_{c,e}}\sqrt{v_x^2+v_y^2}\right) dv_x dv_y. \tag{2.109}$$

The integrand in this case is *odd* in v_x, implying that the integral (now over negative numbers as well) is zero. The same reasoning applies for v_y.

Given the relation of perturbed velocity to heating, we may relate these results to the ways in which waves heat plasma particles. The first is Ohmic, where the effective resistivity heats up the species. The second is resonance with the perturbed species velocity along the magnetic field lines. If the electric field and the particle velocity oscillations are in phase with each other, the wave will resonate with the particle and deposit energy into it. Perpendicular to the magnetic field, however, the magnetic field stops this deposition of energy. One possible physical explanation for this stems from our assumption that the waves are much lower frequency than the magnetic field. Thus, the particle velocity perpendicular to the magnetic field is rather dominated by its gyromotion. On the timescale of the wave, the particle will oscillate back and forth many times, thus inducing a zero-average energy imparted.

Now that we have established the effect of these waves on the electron population, one more problem remains– namely, how might we relate ω to $\mathbf{k}$? For this purpose, we will further analyze the ions in a similar manner. As we have assumed that the ions are cold and unmagnetized, we may use the ion fluid equations. The perturbed momentum equation is

$$\frac{\partial \mathbf{u}}{\partial t} + \mathbf{u}_i \cdot \nabla \mathbf{u}_i = \frac{q_i}{m_i}\mathbf{E}. \tag{2.110}$$

Following the same perturbation analysis with the assumption that the steady-state does not depend on time yields

$$\tilde{\mathbf{u}}_i = -\frac{q_i}{m_i}\frac{\tilde{\mathbf{E}}}{\omega - \mathbf{k}\cdot\mathbf{u_{i,0}}}. \tag{2.111}$$

To incorporate the ion density and solve for the susceptibility, we may incorporate the ion continuity equation,

$$\nabla \cdot (n_i \mathbf{u}_i) = 0. \tag{2.112}$$

Solving the continuity equation for $\tilde{\mathbf{u}}_i$ and substituting the solution in to Eqn. 2.111 yields a final form for the perturbed density of

$$\frac{\tilde{n}_i}{n_{i,0}} = \frac{\mathbf{k}\cdot\tilde{\mathbf{u}}_i}{\omega - \mathbf{k}\cdot\mathbf{u_{i,0}}}.. \tag{2.113}$$

Finally, combining Eqn. 2.111 and 2.113 yields

$$\frac{\tilde{n}_i}{n_{i,0}} = -\frac{q_i}{m_i}\frac{\mathbf{k}\cdot\tilde{\mathbf{E}}}{\left(\omega - \mathbf{k}\cdot\mathbf{u}_{i,0}\right)^2}. \tag{2.114}$$

After determining the ion density perturbation, we are finally ready to define the dispersion relation for the LHDI (Eqn. 2.54. This equation takes the form

$$0 = 1 - \frac{\omega_{pi}^2}{\left(\omega + k_\perp v_E\right)^2} + \frac{1}{k^2\lambda_D^2}\left[1 + \frac{\omega - k_\perp v_D}{k_\parallel v_{te}} e^{-k_\perp^2 r_L^2/2} I_0\left(\frac{k_\perp^2 r_L^2}{2}\right) Z\left(\frac{\omega}{k_\parallel v_{te}}\right)\right], \tag{2.115}$$

where we have replaced $\mathbf{u}_{i,0}$ with $-v_E$ as per our coordinate shift convention. Equation 2.115 represents the dispersion relation for the LHDI under the assumptions that we have provided. Fundamentally, it represents an extra equation to relate ω to $\mathbf{k}$, thus completing our equations for the wave. We note that Eqn. 2.115 is in the still-electron frame, with the electrons moving with azimuthal velocity $u_i = -v_E$. However, a lab measurement in a partially magnetized system would not be in this frame– rather, the electrons will be rotating with velocity v_E and the ions would me mostly still. To resolve this discrepancy, we only need to perform a Doppler shift on the resulting frequency, which takes the form

$$\omega \rightarrow \omega + v_E k_y. \tag{2.116}$$

In this section, we have now fully derived a prediction for an LHDI, which is driven unstable under conditions that we may observe in a magnetic nozzle.

2.3 Conclusion

In this chapter, we have outlined from first principles two areas in which finite amplitude waves may impact electron dynamics in magnetic nozzles. We first introduced quasilinear theory in showing how their presence may induce an effective collision term in the kinetic equation for the steady-state distribution function. We then took moments of this term to show their possible impact on momentum and energy transfer. We then established the appropriate assumptions applicable to a magnetic nozzle plasma and used them in the kinetic and fluid equations with Gauss' law to derive these quantities for the LHDI. Finally, we introduced a quasi-one dimensional model for a magnetic nozzle expansion and determined the impact that waves may have on global expansion in two ways– by inhibiting heat conduction or by directly heating the plasma. In the following section, we will present the experimental methods used to evaluate this theory.

CHAPTER III

Experimental Methods

3.1 Introduction

In this chapter, we first introduce the plasma source used for the experiments in this work and the vacuum chamber used for them. We then discuss the suite of diagnostics that we employed. We first introduce the background theory behind Langmuir probes and their use in our work to determine steady-state plasma characteristics. We then discuss ion saturation probe pairs and the Beall cross-correlation technique, which we implemented to gain a better understanding of the wave propagation characteristics. We finally discuss the high-speed imagery that we used to non-invasively observe oscillations in the source region.

3.2 Electron cyclotron resonance thrusters

Electron cyclotron resonance (ECR) plasma sources rely on microwave power transmission between an antenna and a partially magnetized plasma. Fundamentally, they apply an oscillating electromagnetic wave at the electron cyclotron frequency,

$$\Omega_{c,e} = \frac{eB}{m_e}. \tag{3.1}$$

An oscillating electric field in phase with the electron orbit will indefinitely en-

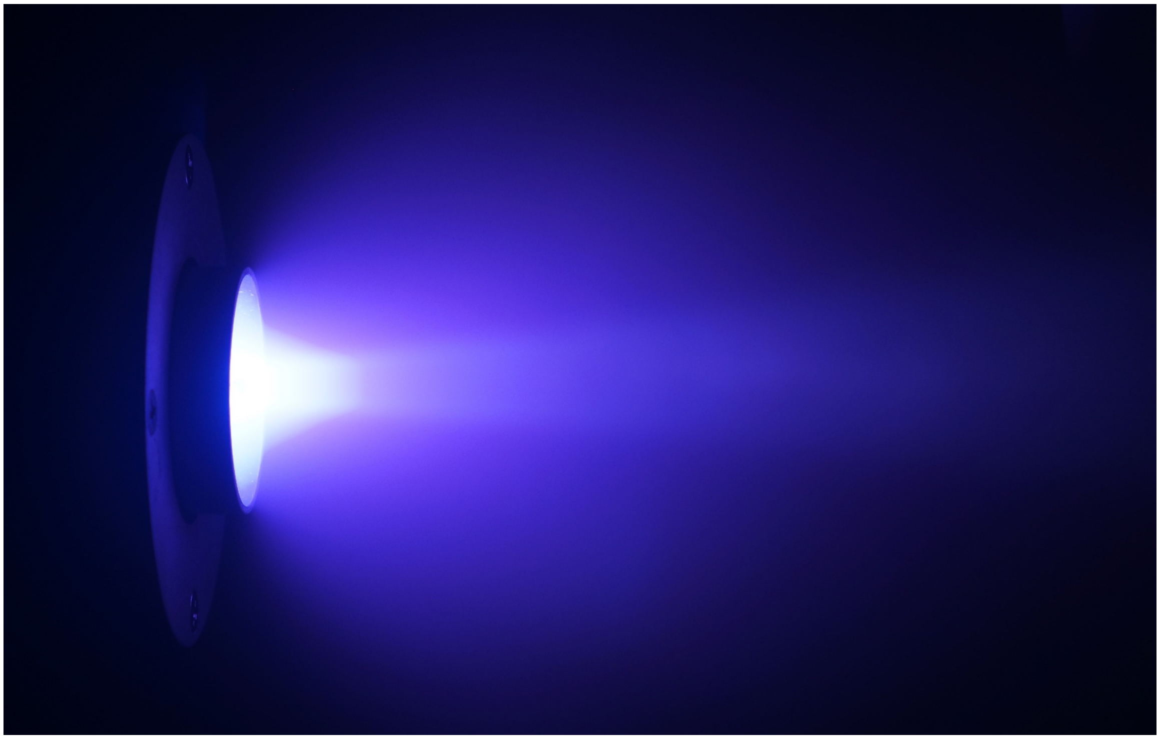

Figure 3.1: ECR thruster firing at 30 W forward power and 10 sccm-Xe flow. Photo credit: Benjamin Wachs.

ergize the particle. In this way, these sources are able to produce a plasma with a high electron temperature. Such a plasma is ideal for a magnetic nozzle. Given the conversion from thermal to bulk energy, a high temperature implies that more energy is available per ion, which yields an increased specific impulse.

During this work, we operated on two separate iterations of a single ECR thruster. The first prototype consisted of a set of annular, permanent magnets made from neodymium mounted internally to the thruster behind the chamber. It also had a single inlet for propellant flow into an intermediate chamber. This chamber was connected to the main discharge by 12 holes spaced symmetrically around the back of the discharge chamber. The walls were made of aluminum, but a ceramic plate was used on the back wall to separate the connection it from the plasma. This plate had a radius that was one half of the total back wall radius. Both the diameter and the

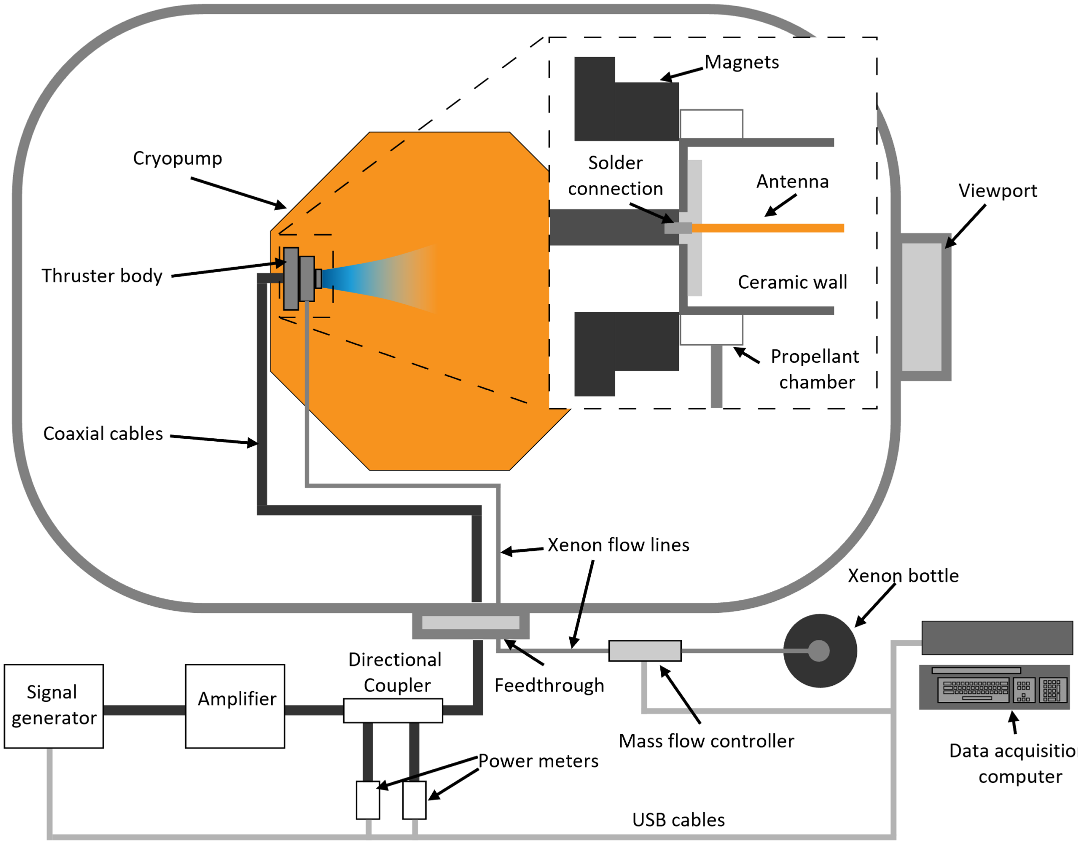

Figure 3.2: Schematic of thruster operating in Junior with coaxial power cables, flexible gas flow lines, external hardware, data acquisition, and thruster body cutout.

length of the discharge region was 25 mm. A 1mm diameter antenna was mounted internally on centerline and was made of copper. It was connected to a TNC feed with solder. We operated the antenna at 2.45 GHz, which corresponds to a resonant frequency of 875 Gauss.

The thruster used in Chap. VI was similar to the first, but had several changes. First, we replaced the copper antenna with graphite to lower sputter losses. We also modified the connection between the antenna and the power feed so that the antenna was threaded onto the back wall. This design allowed us to operate more reliably at higher powers. Finally, we replaced the neodymium magnets with samarium cobalt.

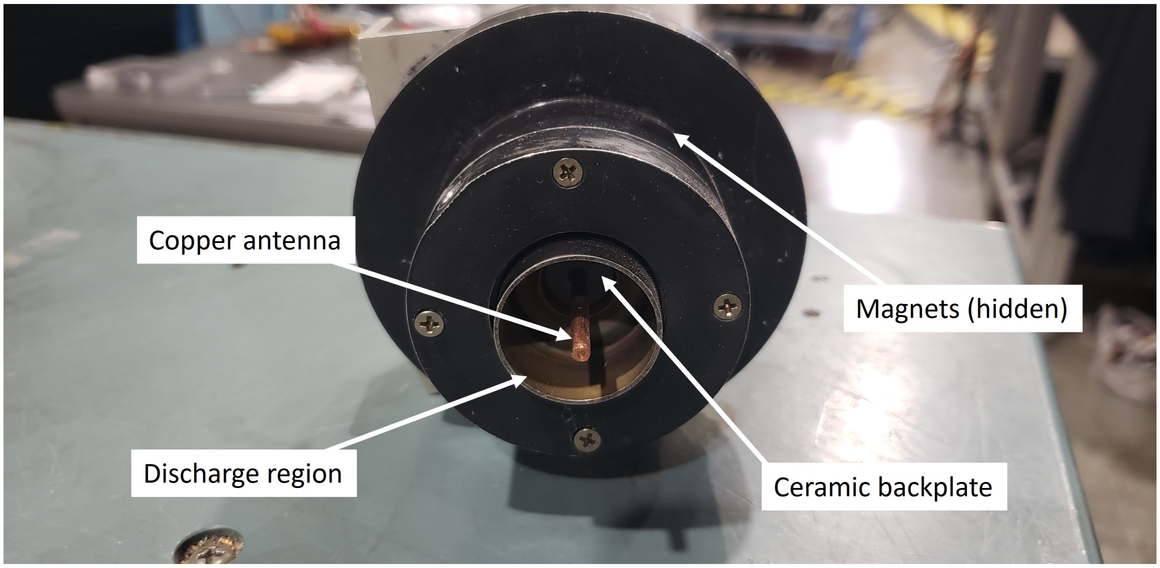

Figure 3.3: Close up image of the thruster used in Chaps. IV and V. Note that the version pictured is after we painted it black in an attempt to maintain lower operating temperatures.

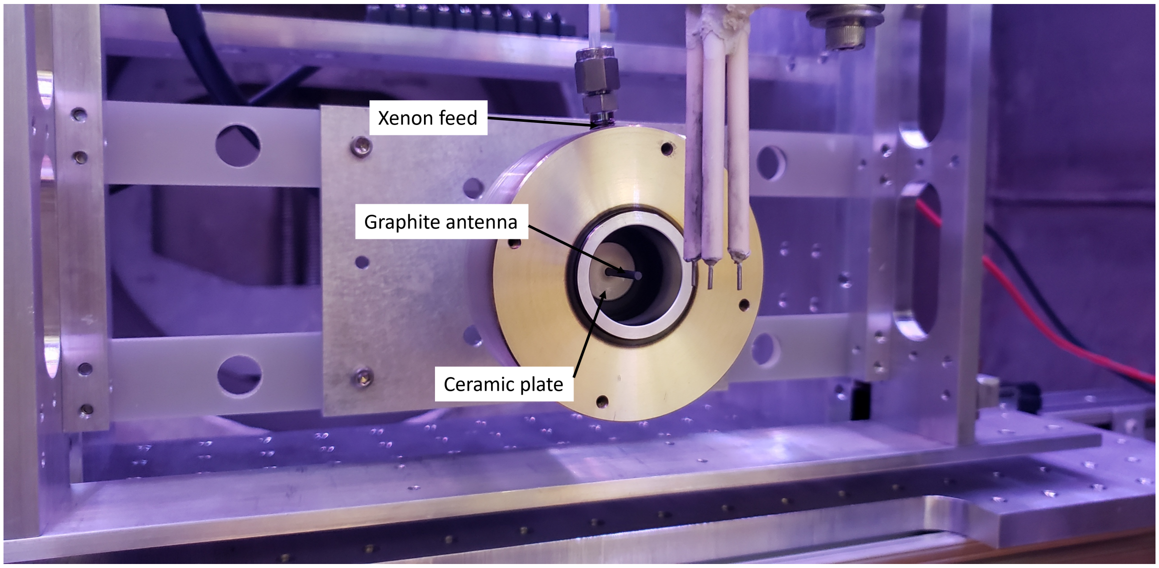

Figure 3.4: Close up image of the thruster used in Chap. VI. Also pictured here is the thrust stand that it was mounted on, which is not the subject of this work.

3.3 Junior vacuum facility

We conducted all of these experiments in the Junior vacuum facility at the University of Michigan. Junior is a 1m diameter by 3m length, cylindrical vacuum chamber

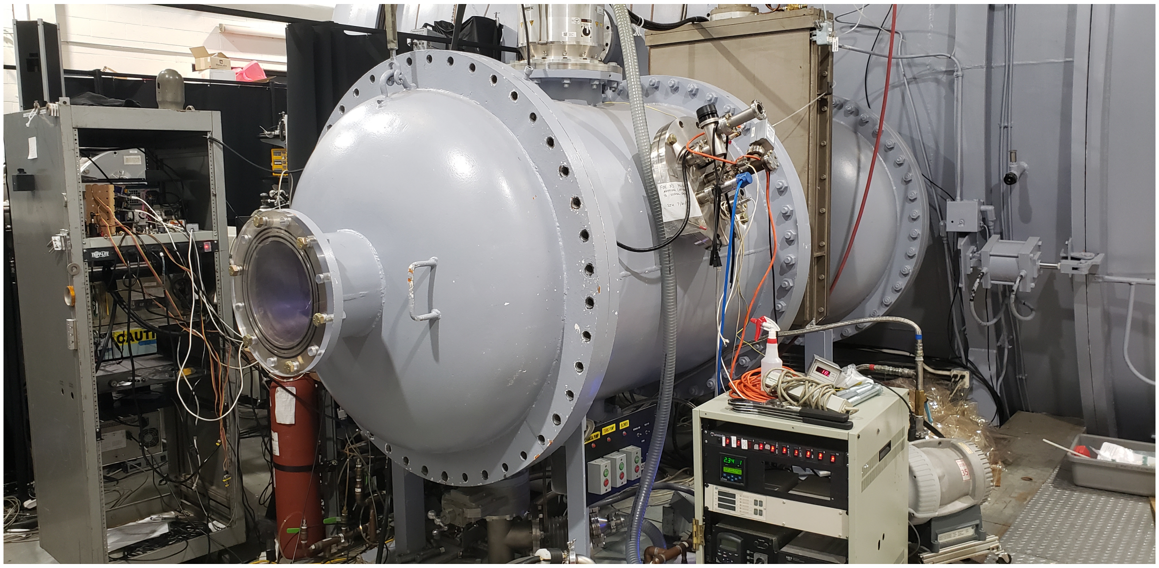

Figure 3.5: The Junior vacuum chamber.

depicted in Fig. 3.5. The primary pumping mechanism for the chamber is a cryogenic plate mounted underneath the thruster. This pump is fueled by chilled helium and maintains a pumping speed of 32,000 L/s on xenon.

While operating the thruster in Junior, we performed several sets of diagnostic tests. The first of these is the Langmuir probe, which we used to determine background plasma measurements.

3.4 Langmuir probe diagnostic

Langmuir probes have been extensively used in plasma physics for almost a century [71]. The fundamental process is relatively simple– we may understand various local parameters about a plasma from applying a voltage to a conducting metal immersed in the plasma and reading its current. However, the details of this analysis vary depending on the plasma and probe characteristics.

Langmuir probes operate on the principle of accelerating ions or electrons down a sheath potential. The total current drawn is a direct function of the voltage applied.

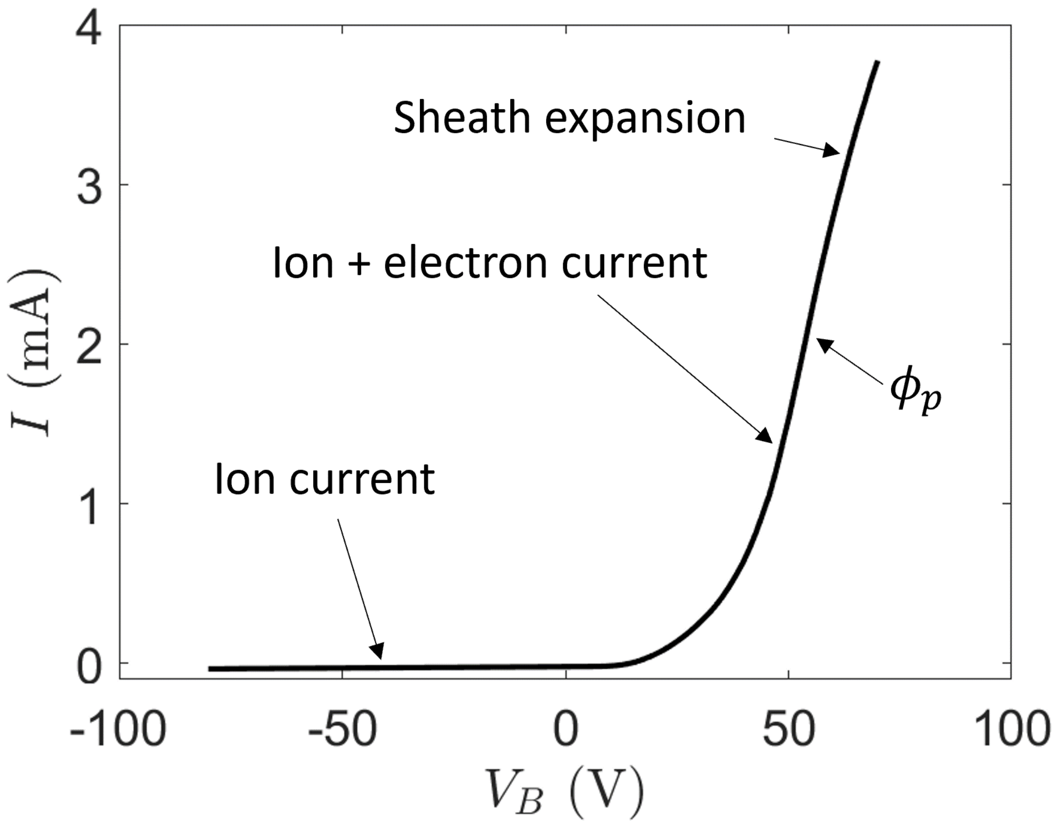

Figure 3.6: Example Langmuir probe trace from this experiment taken at $(r, z) = (30, 45)$ mm with primary current regions and plasma potential ϕ_p labeled.

In general, the current drawn is a balance between electrons and ions fluxing to the probe, with the bias itself repelling portions of either species. Performing such a sweep determines a current-voltage (I-V) characteristic, an example of which we show in Fig. 3.6. This trace consists of three primary areas defined by two extremes.

In the first extreme, a strong negative bias will repel any electrons, and any current collected is made up of only the ions. In an ideal sense, ions accelerate to such a barrier at the Bohm speed,

$$u_B = \sqrt{\frac{T_e}{m_i}}. \tag{3.2}$$

Assuming this limit and neglecting higher charge states yields an equation for the ion number density,

$$n_i = \frac{I_{i,sat}}{A_p e u_B} \tag{3.3}$$

where A_p is the total area of the probe. While this is a useful approximation, the assumptions embedded in its derivation may be prohibitive. The most important one is the so-called thin-sheath approximation. This approximation states that the characteristic length of the probe (the diameter for a cylindrical probe) is much less than the Debye length, which is defined as

$$\lambda_D \equiv \sqrt{\frac{\epsilon_0 T_e}{n_e e^2}} \tag{3.4}$$

and characterizes the length of the sheath. When $\lambda_D << r_p$, approximating the current from the Bohm speed is generally accurate. However, for the plasmas used in this study, implementing a probe large enough to fulfill this criterion downstream would have drawn a significant portion of the total electrons present in the plume. We thus implemented probes that had a diameter on the same order as λ_D. In this regime, we must turn to a more complicated theory to accurately characterize the plasma.

When the sheath and probe are of comparable lengths, it is recommended to apply orbital motion limited (OML) theory [79]. In this paradigm, there is a chance that an ion entering the sheath may "fly-by" the probe without being collected. In this regime, the ion current does not saturate at low biases, but rather continually increases as V_B is driven more negative. The ion saturation current as a function of V_B is then

$$I_{i,sat} = \frac{e n_i A_p}{\pi} \sqrt{\frac{2e(V_B - \phi_p)}{m_i}}. \tag{3.5}$$

Once we know ϕ_p, we may apply linear regression on $I_{i,sat}(V_B)$ to find n_i.

When not in the ion saturation regime, the finite electron current can be approximated as an exponential,

$$I_e = I_{e,sat} \exp\left(\frac{V_B - \phi_p}{T_e}\right) \tag{3.6}$$

where $I_{e,sat} = en_e A_p \sqrt{\frac{eT_e}{2\pi m_e}}$ is the electron saturation current. This value arises as a result of space charge limitation, which is a fundamental limit that appears in plasma current across a potential drop. Above the electron saturation current, this idealized theory predicts a constant value. As a result, the current draw at $V_b = \phi_p$ is predicted to be non-differentiable at ϕ_p.

In practice, however, the probe current continually increases past ϕ_p. This trend results from the fact that the collection area is not strictly the area of the probe–rather, the area defined by the sheath may be a more accurate value (although, as we will see, even the validity of this assumption is limited). Continually increasing the bias expands the sheath, increasing the current collected. However, this process typically maintains a current draw trend that is slower than exponential. The result is a relatively clear cutoff between the two regions, as indicated by the ϕ_p label in Fig. 3.6.

Practically, the cutoff point may be specified by finding the maximum of the first derivative of the I-V characteristic. This point represents the upper limit of the exponential trend, before which the graph begins to flatten. As such, we define ϕ_p for these experiments as the bias voltage at which the derivative in the current trace is maximized. For these measurements, we first applied a LOESS (locally estimated scatterplot smoothing) algorithm to the data. This method implements a local second order polynomial to find fit parameters throughout the domain, and resulted in a single maximum value of the derivative for every case.

The final parameter that we find from an I-V characteristic is the electron temperature. While there are multiple ways to determine the temperature, they typically rely on the assumption that the electron energy distribution function is Maxwellian, which results from a dominant collision processes. However, it has been observed that the electrons in magnetic nozzles are not necessarily in equilibrium, so this assumption may not be useful [32, 126, 16]. For this reason, we instead apply the Druyvesteyn technique [37] to analyze the electron energy distribution function directly and define the temperature based on its second moment.

This process makes no assumptions about the distribution function of the electrons, but instead uses the I-V characteristic to analyze the electron energy distribution directly. Druyvesteyn showed that the EEPF could be found from the second derivative of the I-V characteristic as

$$f\left(\mathcal{E}\right) = \frac{2}{e^2 A_p}\left(2 m_e e \mathcal{E}\right)^{1/2} \frac{d^2 I_e}{d\mathcal{E}^2} \tag{3.7}$$

where $\mathcal{E} = \phi_p - V_B$. Once we have measured the electron distribution function, we may take its second moment to derive the temperature. This value is then given by

$$T_e = \frac{2}{3n_e}\int_0^\infty \mathcal{E} f(\mathcal{E}) \mathrm{d}\mathcal{E}. \tag{3.8}$$

To find the second derivative of the I-V characteristic, we applied a FLOESS technique to smooth the data enough to find a reliable value. Figure 3.8 shows an example probability function found through this analysis.

For this work, we used tungsten probes with a length of 5 mm and a diameter of 1 mm. We used a Keithley 2400 sourcemeter to bias the probes from -70 to 70 V and read the current to determine the I-V characteristic. This device measured current at each point for .2 s and returned the average value recorded. We connected the sourcemeter to a data acquisition computer, with which we commanded

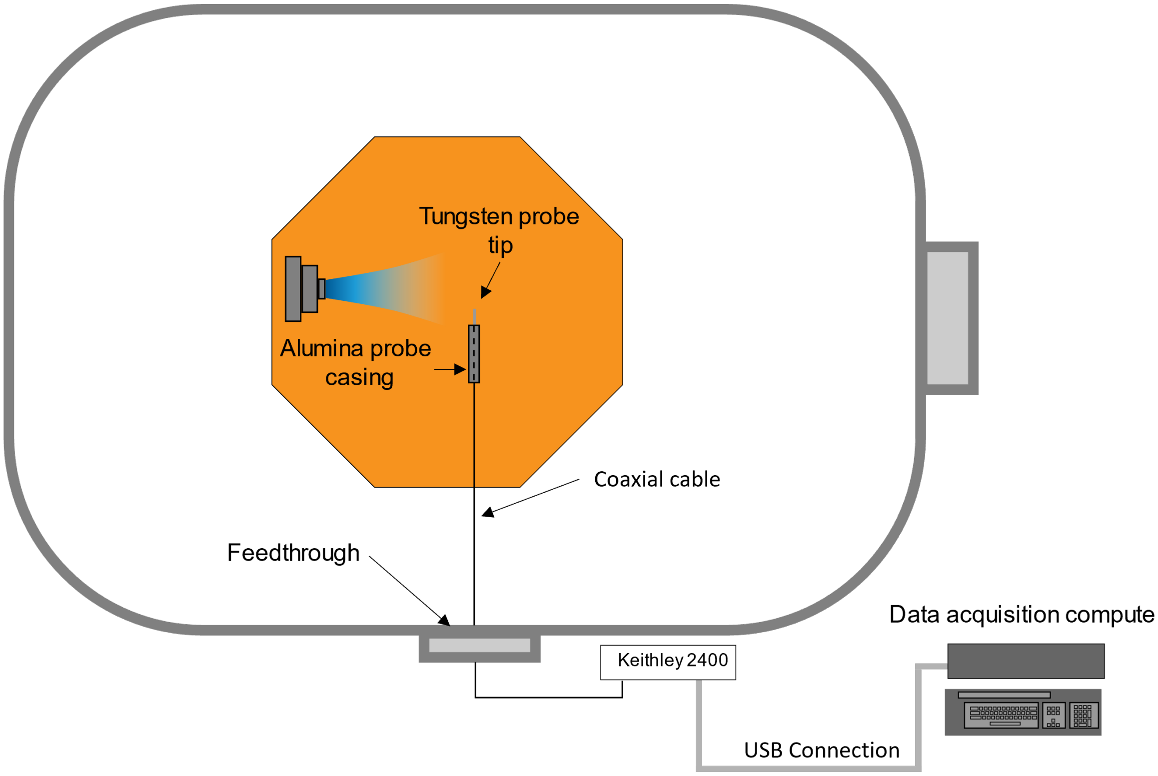

Figure 3.7: Schematic of the Langmuir probe diagnostic as used in this work.

the sourcemeter through a LabView program. Figure 3.7 presents the schematic of connections used in this test.

A possible shortcoming of the Langmuir probe diagnostics is its lack of observation of the temperature in the direction perpendicular to the magnetic field. We note that it is likely that the measured temperatures are in the *parallel* direction, given that the fields likely reduce electron current in the perpendicular direction. As described in Chap. I, ECR plasma sources operate by energizing the electron translational modes perpendicular to the magnetic field, and it is the perpendicular modes that determine thrust and provide energy for drift-driven instabilities. Since most of the energy deposited into the plasma is in the perpendicular direction, some mechanism must be present to convert this energy into the parallel direction for these measurements to be meaningful.

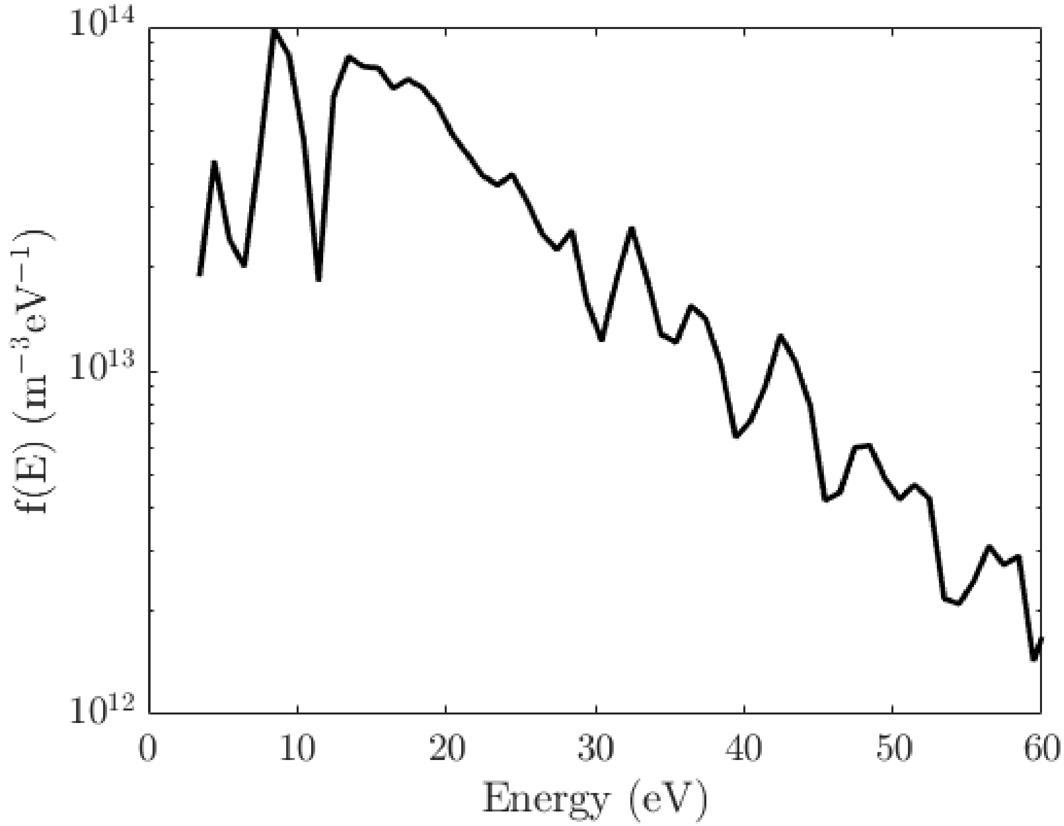

Figure 3.8: Example electron energy probability function. To generate this graph, a LOESS technique was applied to the raw electron current to find its second derivative.

One such mechanism is the conservation of magnetic moment [26]. The general idea behind this concept is that, in addition to energy, a particle traveling along an slowly-varying magnetic field must also exhibit conservation of magnetic moment, defined as

$$\mu = \frac{mv_{\perp}^2}{2B}. \tag{3.9}$$

Thus, in an expanding (i.e. decreasing) magnetic field, the perpendicular velocity of the particle will decrease. However, given the fundamental nature of the conservation of energy,

$$\frac{m}{2}(v_\perp^2 + v_\parallel^2) = \text{const}, \tag{3.10}$$

this energy must be translated into the parallel mode. We may perform a cursory analysis by assuming a particle has perpendicular velocity $v_{\perp,0}$ at magnetic field B_0 and zero parallel velocity. We may then combine Eqns. 3.9 and 3.10 to find the moment of isotropy, $v_\perp = v_\parallel$ at $B = B_0/2$. Assuming the ECR value of $B_0 = 865$ Gauss, we find that isotropy occurs at $B = 432.5$ Gauss. The maximum magnetic field in the downstream measurement domain is ≈ 300 Gauss (Fig. 3.10), implying that this point has already been reached everywhere we have taken probe measurements.

Given that the perpendicular energy should have been mostly converted into parallel energy in the downstream measurements presented in this work, it may appear that our field-aligned measurements are ignoring the perpendicular component of temperature entirely. However, it is likely that these temperatures are in fact comparable. While the magnetic moment conservation analysis neglects electron collisions, we see through our measurements that the electrons are Maxwellian to a good approximation (Fig. 3.8). This type of distribution requires an effective collisionality to generate, implying that we may have such a source in the plasma. While classical collisions are unlikely to be present in high value, it may be that the waves discussed in Chaps. IV and V induce an effective collisionality that drives the electrons towards such an equilibrium state [39]. Such an analysis is outside of the scope of this work. However, taken together, the facts that the measurement domain is downstream of the isotropy point and the generally Maxwellian nature of the electrons imply that we may assume that the parallel (measured) temperature is the same as the perpendicular value.

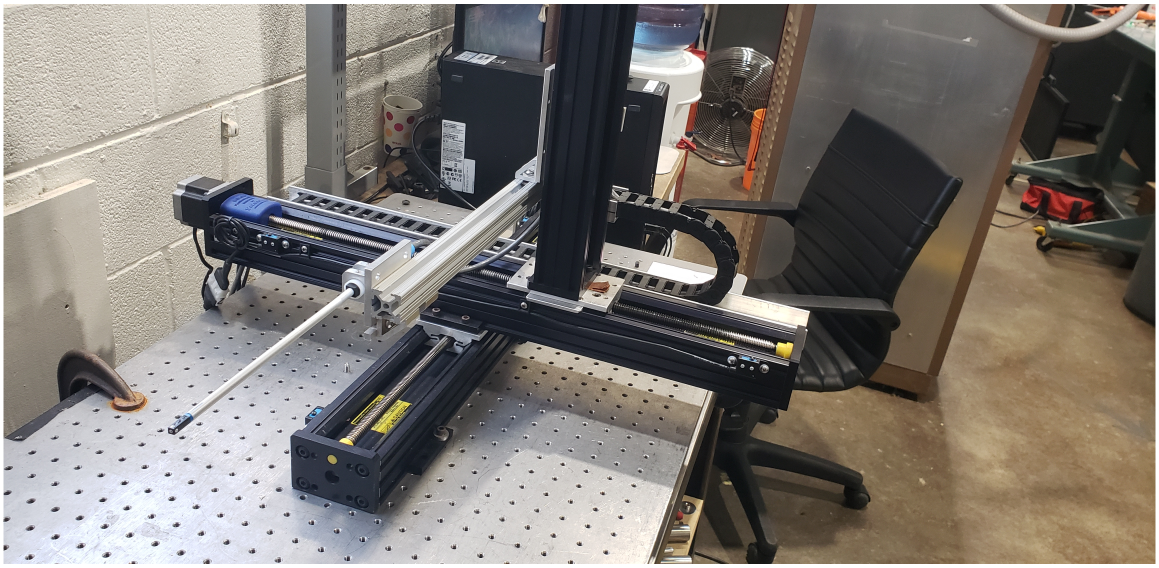

Figure 3.9: Image of Hall probe setup on three-axis motion stages.

3.5 Magnetic field measurement

We characterized the applied magnetic field strength by using a Lakeshore 460 3-axis Gaussmeter and a 3-axis Hall probe. We mounted the hall probe on a set of orthogonal motion stages outside the chamber at atmosphere and measured the magnetic field in 5 mm increments. We then repeated the measurement over the same area with the thruster absent to determine the earth's magnetic field directly and subtracted the earth field from the applied field. We present the results from this test in Fig. 3.10a, where we represent the magnitude of the field in the contour plot and the direction by the overlaying streamlines. We further present a picture of the Hall probe used on the motion stages in Fig. 3.9.

After understanding the background plasma properties and magnetic field, we next applied a cross-correlation technique to determine the frequencies and wavevectors of wave propagation in the plume. This theory is based on the ion saturation portion of the Langmuir probe I-V characteristic.

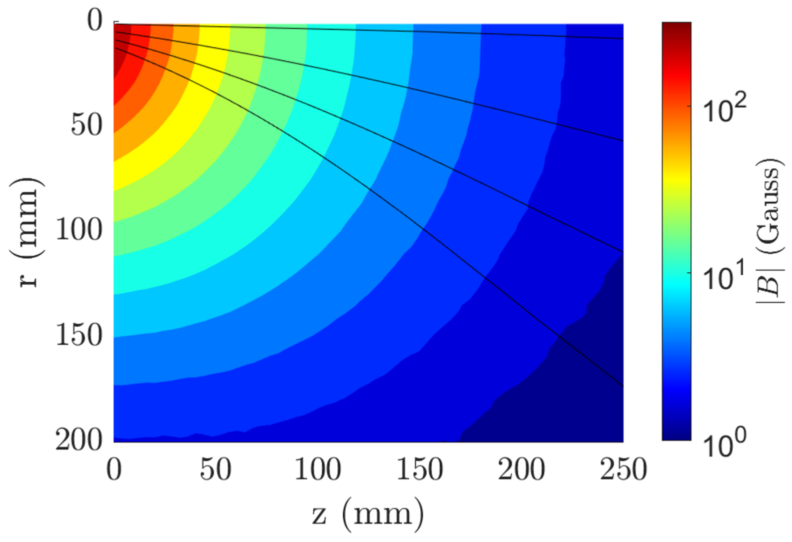

Figure 3.10: Map of the measured magnetic field with magnetic field line overlay.

3.6 Ion saturation probes

To measure the presence of waves, we implement time-resolved readings of Langmuir probes in the ion saturation limit based on the method of Beall [13]. Standard Langmuir probe theory relates the measurement of ion saturation current to the number density as $i_{sat} \propto n_i\sqrt{T_e}$. Assuming quasineutrality on the timescale of a wavqe oscillation $\tilde{n}_i \approx \tilde{n}_e$ allows us to relate the oscillations in these readings to oscillations in electron number density. We must finally assume isothermality of the electrons to let $\tilde{T}_e = 0$.

While isothermality is fundamentally an assumption, we may crudely justify its use by returning to the polytropic equation of state,

$$\frac{T_e}{n^{\gamma-1}} = \text{const.} \tag{3.11}$$

We may use the polytropic assumption to estimate the relative contributions on ion saturation current from number density and electron temperature contributions.

This can be seen by detailing the relative fluctuation in ion saturation current by

$$\frac{1}{i_{sat}}\frac{dI_{sat}}{dt} = \frac{d\ln i_{sat}}{dt} = \frac{d\ln n}{dt} + \frac{1}{2}\frac{d\ln T_e}{dt} \tag{3.12}$$

$$= \frac{d\ln n}{dt} + \frac{\gamma - 1}{2}\frac{d\ln n}{dt}. \tag{3.13}$$

We identify the first and second terms on the right hand side of Eqn. 3.13 as the contribution from number density and temperature, respectively. The polytropic index γ, as discussed in Chap. II, takes limits of 1 and 5/3. Within these limits, we see the relative contribution from the electron temperature is at most 1/3 of the contribution of the number density fluctuations. Thus, even in the fully adiabatic limit, the electron temperature fluctuations are likely less than the number density oscillations. For these purposes, we will neglect oscillations in temperature in this analysis.

Given the lesser significance of the temperature fluctuations in ion saturation current measurements, we approximate the measurements as

$$\frac{\tilde{i}_{sat}}{i_{sat}} \approx \frac{\tilde{n}_e}{n_e}. \tag{3.14}$$

In doing so, we may perform Fourier analysis on a time-resolved single-probe measurements to find the dominant frequency modes in the plasma. However, we would like to measure the dispersion itself. The Beall technique does so by taking simultaneous measurements from two probes with a known spatial separation Δx. Assuming that a number density oscillation at frequency ω and wavenumber k_x maintains coherency between the two probes, its value will propagate as

$$\frac{\tilde{n}_e(x,t)}{n_e} = \frac{\tilde{n}_e}{n_e}(\omega)\exp(-i\omega t + ik_x x). \tag{3.15}$$

Taking simultaneous measurements of i_{sat} at x_1 and x_2 provides

$$\frac{\tilde{i}_{sat,1}}{i_{sat,1}} = \frac{\tilde{n}_e(\omega, k_x)}{n_e} \exp(-i\omega t + k_x x_1) \tag{3.16}$$

$$\frac{\tilde{i}_{sat,2}}{i_{sat,2}} = \frac{\tilde{n}_e(\omega, k_x)}{n_e} \exp(-i\omega t + ik_x x_2). \tag{3.17}$$

Assuming the wave maintains the same frequency and amplitude, we may determine the wavenumber directly by the phase difference as measured by each probe:

$$k_x = \frac{\Delta\theta}{\Delta x} \tag{3.18}$$

where $\Delta\theta$ is the phase difference as measured by each probe. We may apply a Fourier transform to the probe reading to get $\mathcal{F}(\tilde{n}/n)$. We may in turn use this value to determine the magnitude and argument of both probe readings. Knowing ω, x_1, and x_2 will then allow us to determine k_x. First, we have, for any complex number $\tilde{s} = e^{i\theta}$,

$$\theta = \tan^{-1}\left(\frac{\mathrm{Im}(\tilde{s})}{\mathrm{Re}(\tilde{s})}\right). \tag{3.19}$$

We may then use the fact that

$$\frac{\mathcal{F}(s_2)}{\mathcal{F}(s_1)} = e^{i(\theta_2 - \theta_1)} \tag{3.20}$$

to find an expression for the phase difference,

$$\theta_2 - \theta_1 = \tan^{-1}\left(\frac{\mathrm{Im}\left(\mathcal{F}^*(s_1)\mathcal{F}(s_2)\right)}{\mathrm{Re}\left(\mathcal{F}(s_1)\mathcal{F}^*(s_2)\right)}\right) \tag{3.21}$$

where an asterisk indicates a complex conjugate. With this expression, we are able to determine the phase difference in a wave at frequency ω provided only that we know the distance between the probes. Figure 3.11 illustrates this process.

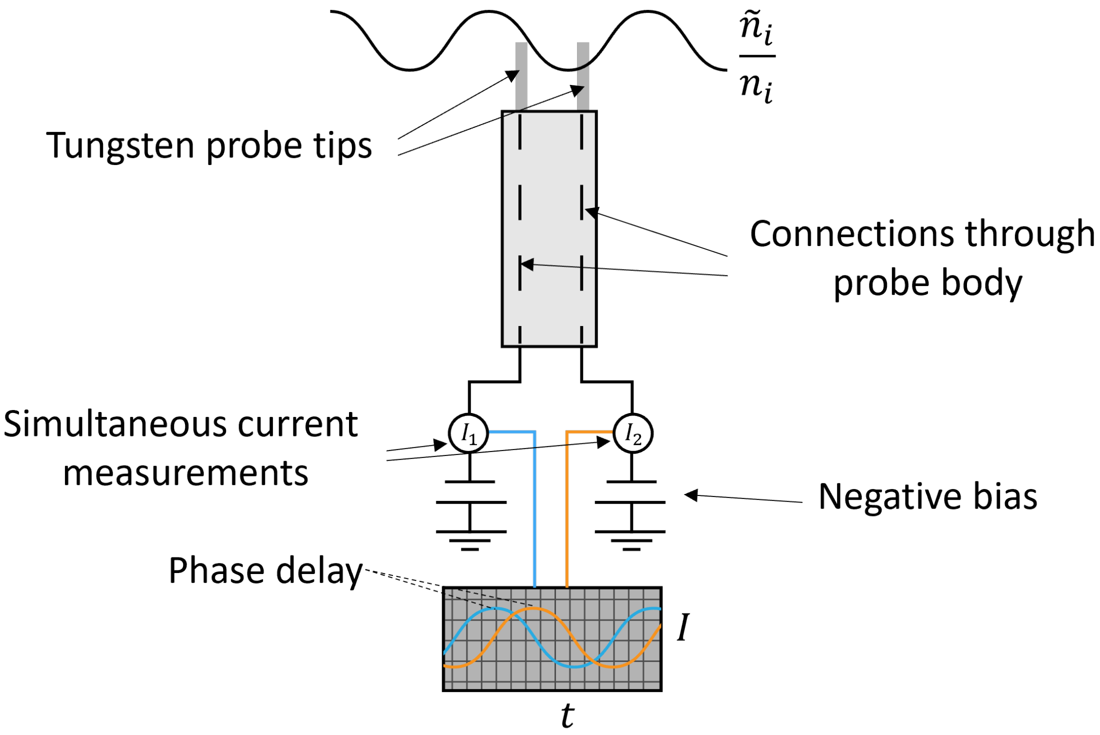

Figure 3.11: Illustration of wave probe schematic.

One important issue arises with this understanding of phase difference. Namely, there is a fundamental upper limit in the wavenumbers that we are able to resolve. Since $\Delta\theta$ exists in the range $-\pi < \Delta\theta < \pi$, we fundamentally have a maximum wavenumber of

$$k_{max} = \frac{\pi}{\Delta x}. \tag{3.22}$$

This relation states that any wave that performs more than a full oscillation between the probes will be resolved at a different wavenumber,

$$k_{resolved} = k - \frac{2\pi N}{\delta x} \tag{3.23}$$

where N is the number of oscillations that the wave has undergone. If we have a reason to believe this to be the case, we may alias the resulting wavenumber by

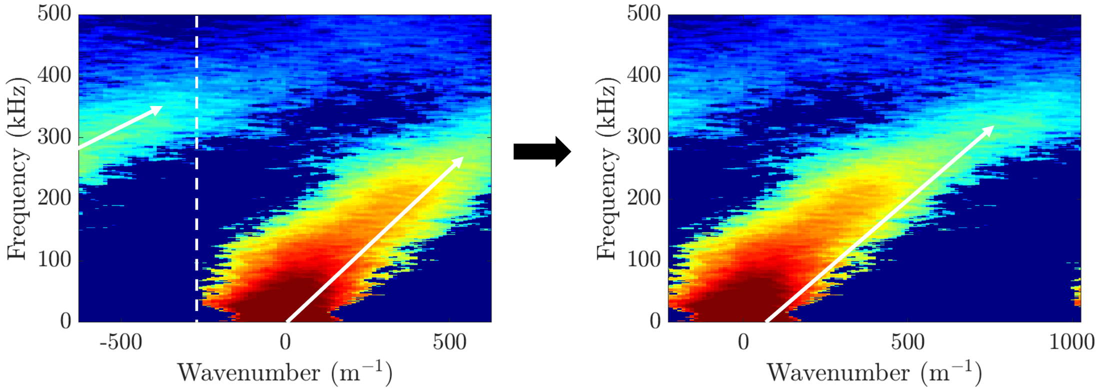

Figure 3.12: Aliasing of an example dataset from ion saturation probes.

shifting the measured value per Eqn. 3.23. We illustrate this process in Fig. 3.12.

In this work, we mounted a total of five probes to a set of three-axis motion stages, as illustrated in Fig. 3.13. These were arranged in two sets. The first set consisted of a pair of probes separated vertically and pointed in the $-r$ direction. We used these to measure azimuthal propagation. The other set had three probes pointed downwards in an “L” shape, which we used to measure propagation in the r and z directions. We biased each probe to -45 V to ensure that the collection was within the ion saturation regime of the plasma and could approximate ion number density. We separated the azimuthal probes by 5 mm and the $r - z$ probes by 7 mm.

We connected the probes to a 100 Ohm high speed resistor and measured the voltage across it using an oscilloscope at a rate of 5 MHz, providing a maximum resolvable (Nyquist) frequency of 2.5 MHz. We read data at each point for 1 s. Doing so allowed us to repeat the analysis multiple times, resulting in a statistical spread of intensities at each frequency.

To complete the Beall analysis, we represent the intensities in a two-dimensional plot in (ω, k) space. Each point will take an intensity given by the average power present at the small point in the ranges $[\omega, \omega + \Delta\omega]$ and $[k, k + \Delta k]$. The resolution $\Delta\omega$ is determined by the time resolution and temporal bin size to be 50 Hz. We

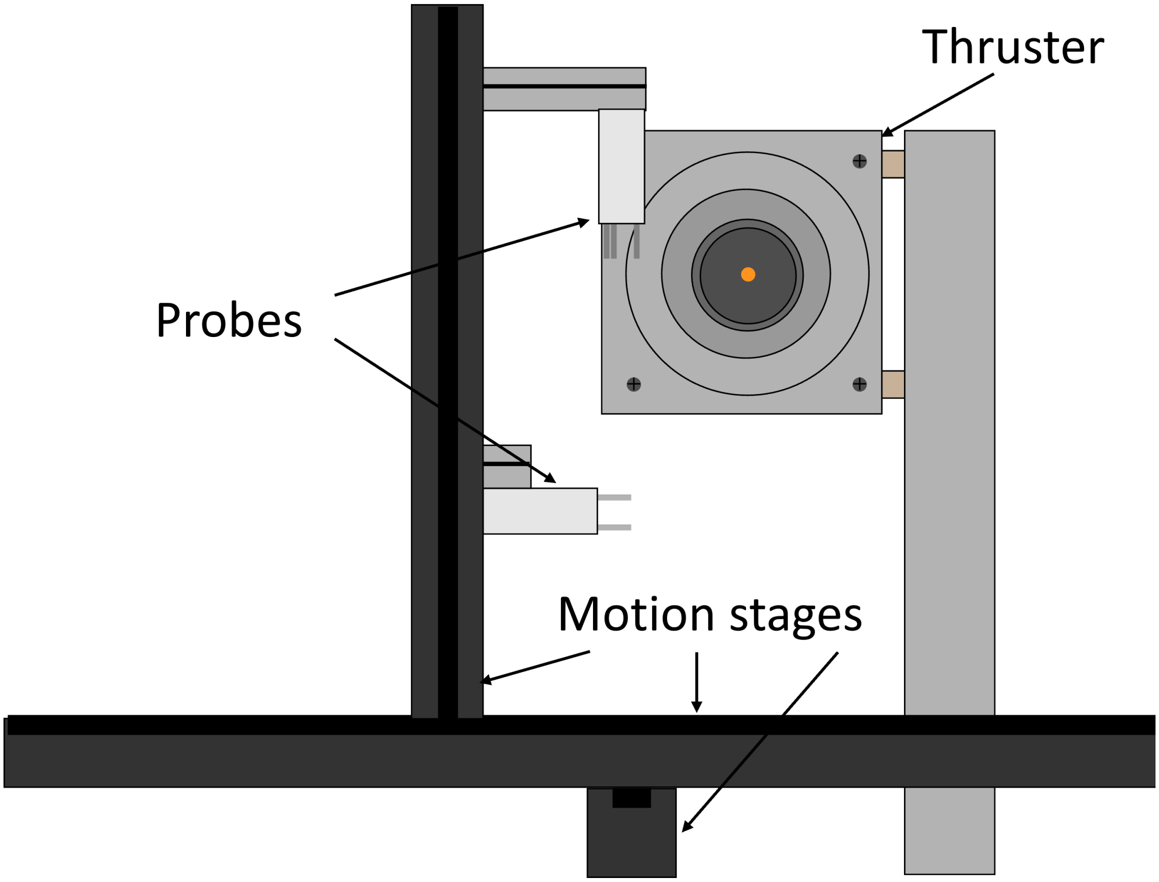

Figure 3.13: Drawing of primary components of the experimental setup.

further binned the wavenumber axis in 100 equally-spaced bins for each dataset. Performing this binning technique allowed a statistical spread of the measurements, which provides the finite width of the measurement seen in Fig. 3.12.

3.7 Error analysis of probe-based measurements

Throughout this work, we will encounter two forms of uncertainty on both of the above probe-based measurements: statistical and systematic. Statistical uncertainty stems from the fact that we may never be fully confident about any direct measurement. For example, if we are slightly uncertain about the probe dimensions, it may propagate into an error source in the measurement. To account for this discrepancy, we must assume that these measurements were wrong by a small amount. Once we have uncertainty in the probe dimensions, the voltage we were applying, and the current that was being drawn, we may propagate these values through the formulae for the Langmuir probe analysis to arrive at final uncertainties for the measured values [79]:

$$\frac{\partial A_p}{A_p} \approx \frac{2\pi}{A_p}\sqrt{\left(L + r_p\right)^2 \partial r_p^2 + r_p^2 \partial L^2} \tag{3.24}$$

$$\frac{\partial T_e}{T_e} \approx \sqrt{2\left(\frac{\partial V_B}{\Delta V_B}\right)^2 + 2\left(\frac{\partial I_{e,\mathrm{sat}}}{I_{e,\mathrm{sat}}} \cdot \frac{T_e}{\Delta V_B}\right)^2} \tag{3.25}$$

$$\frac{\partial n_e}{n_e} \approx \sqrt{\left(\frac{\partial I_{e,\mathrm{sat}}}{I_{e,\mathrm{sat}}}\right)^2 + \left(\frac{\partial A_p}{A_p}\right)^2 + \left(\frac{\partial T_e}{2T_e}\right)^2} \tag{3.26}$$

where ∂ indicates absolute uncertainty in a value, V_b is the bias voltage, $I_{e,sat}$ is the electron saturation current, L is the length of a cylindrical probe, r_p is its radius, and A_p is the total probe surface area. For the purposes of this work, we take the uncertainty in both probe dimensions to be 5%, and the uncertainty in the current measured to be 1%. The voltage step size was $\Delta V_B = 1$ V.

In results derived from these values, it is not always as simple to propagate these uncertainties by standard techniques. For example, our calculation of γ in Chap. V will require solving a complex equation of area-averaged plasma properties and their derivatives. Moreover, such a calculation is fundamentally limited by values of 1 and 5/3. Standard propagation techniques may result in a bound that is outside of physical possibility.

To get around these issues, we implement a technique known as "bootstrapping." This process involves randomly sampling the background parameters a large number of times, solving for the required quantity, then generating a distribution of the results. The error bars may then be defined by the 5th and 95th percentiles of the resulting distribution. We apply this method to calculate γ in Chap. V and the anomalous collision frequency ν_{an} in Chaps. IV and V, which requires a statistical average of an integrated quantity $(\tilde{n}/n)$.

3.8 High speed imagery

Our final diagnostic involved high speed imagery of the plasma. This method allows noninvasive observation of plasma oscillations. The fundamental assumption that enables this process is the relative equivalence of pixel intensity to number density,

$$\frac{\tilde{I}}{\bar{\bar{I}}} \propto \frac{\tilde{n}_e}{n_e} \tag{3.27}$$

where I represents a pixel intensity. This assumption is predicated on the concept that the light emission by a plasma is due to electron impact collisions with either ions or neutrals. This method has been used successfully to observe waves in Hall thruster channels [81, 82] and hollow cathodes [60, 53]. In making this assumption, we may treat the pixel readings similarly to the ion saturation probe measurements in the previous section. Namely, for each pixel p, we will define the intensity $|\mathcal{F}(I_p(t))|$ and the phase $\arg\left(\mathcal{F}(I_p(t))\right)$ to determine the primary propagation characteristics of this mode.

It is important to note that the readings from this measurement will be *line integrated.* This trait implies that it will measure values from every point in a line that is within a certain region from the focal point, which we chose to be the end of the antenna. Previous work has shown that this fact will lessen the total oscillation magnitude (compare magnitudes from Refs. [60] and [62]). For this reason, this measurement system will not provide us with a reliable measure of the wave-induced collision frequency, since the oscillation magnitude will likely be damped. However, it will prove useful in analyzing the global modes present in the system.

To this end, we will again analyze the results in two ways. We will first record the data and store it in an $m \times n \times l$ array, where the image height is m pixels, the width is n pixels, and the length is l frames. We will first divide out the mean from each pixel, such that the resulting intensity is

$$\tilde{I}_{i,j}(t) = T \frac{I_{i,j}(t)}{\int I_{i,j}(t')dt'} - 1. \tag{3.28}$$

where T is the timespan of the measurement. In so averaging the immediate results, we normalize the values to ensure uniform scaling on any oscillations present. As a result of this normalization, we are also able to more directly analyze the *relative* fluctuations in intensity, which we take as a proxy for oscillations in number density. Next, we again apply Fourier analysis to convert the intensity into frequency space,

$$I_{i,j}(\omega) = \mathcal{F}(I_{i,j}(t)). \tag{3.29}$$

We understand the results from the Fourier analysis in two ways. First, we may look at the magnitude of the oscillations $|I_{i,j}(\omega)|^2$, which provides the power spectral density. We will look at the amplitude measurement both integrated over the entire image and by the individual pixel. While we cannot take this as an absolute value, it still proves useful to determine where in the plasma any oscillations are occurring.

The second analysis method will involve the phase of the Fourier transform. Similar to the wave probe analysis, we will use this characteristic to determine the propagation characteristics of the wave. One advantage of the high-speed imagery is that we are now able to directly observe *global* oscillations. In particular, we will discuss these results in terms of azimuthal modes. Since we are unable to resolve axial propagation, we will assume a wave character that takes the form

$$I_{j,k}(\omega) = A(r)e^{im\theta}. \tag{3.30}$$

Here, $A(r)$ is the amplitude of the wave, which we will assume to vary only with radius r. The mode is m, which is a nonnegative integer. The phase then varies with $m\theta$, where θ is the azimuthal coordinate. In applying this method, we may visually observe global oscillations in the plume.

For this experiment, we used a Fastcam SA5 with a variable lens with focal lengths between 18 and 135 mm to observe the plasma in the discharge, as depicted in Fig. 3.15. We took 1 s measurements at 300,000 fps to analyze the presence of any low frequency modes. This framerate allowed us to take 64×256 pixel imagery. In Chap. VI, we will present these results and discuss their implications for wave presence in magnetic nozzles. Figure 3.14 shows a schematic of how this experiment was arranged in Junior, and Fig. 3.15 shows a picture of the Fastcam mounted outside of the chamber.

3.9 Conclusion

In this section, we have introduced the experimental methods we used for this work. We first described the thruster, an ECR source that we operated in the Junior vacuum facility. We then discussed the Langmuir probe techniques that we used to determine the steady-state plasma values and the cross-correlation technique we applied to observe wave presence. We finally explained how we used high-speed imagery to determine global characteristics of the low-frequency mode in a noninvasive way. In the next chapter, we present and discuss the results of the Langmuir probe and wave probe tests as they relate to cross-field transport of the electrons.

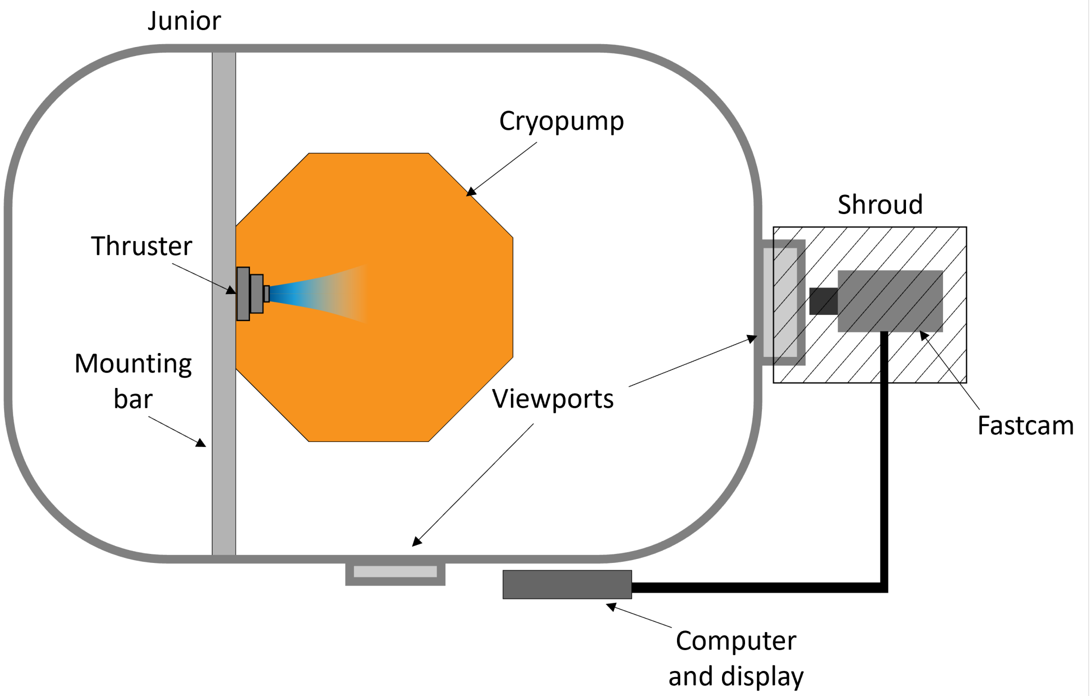

Figure 3.14: Arrangement of high speed imagery experiment (not to scale).

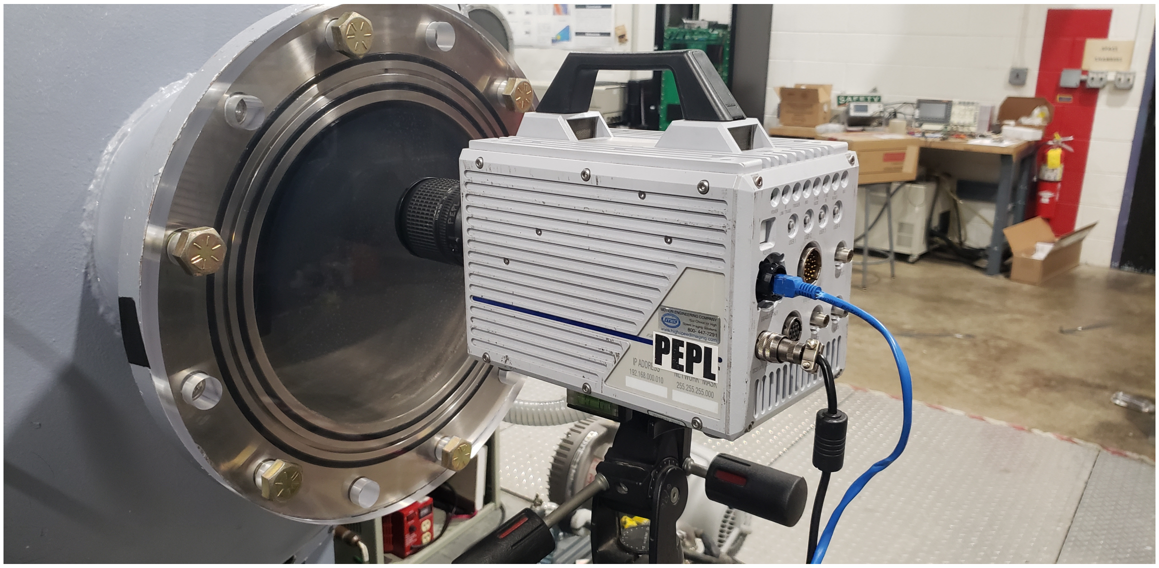

Figure 3.15: Picture of the high-speed camera mounted on a tripod outside of Junior with attached lens.

CHAPTER IV

Cross-Field Momentum Transport from a Lower Hybrid Drift Instability

4.1 Introduction

In this chapter, we present the results of the probe-based measurements of both waves and steady-state plasma parameters and determine to what extent they influence electron cross-field transport. We first present the details of the measurement, including the magnetic field and the measurement domain. We analyze in turn the steady-state Langmuir probe measurements and use them in conjunction with wave measurements to determine the effective collision frequency in the plume. We find that the transport induced by waves is likely significant in the evolution of the plasma and further determine that they have a detrimental impact on thruster performance by contributing to divergence of the ions.

4.2 Experimental methods

For this work, we mounted a set of probes downstream as described in Chap. III to measure time-resolved ion density and relate their oscillation magnitudes to effective wavenumbers. We further used one probe on the azimuthal arm to take steady state measurements as per Chap. III. We measured half of the plume beginning 3 cm

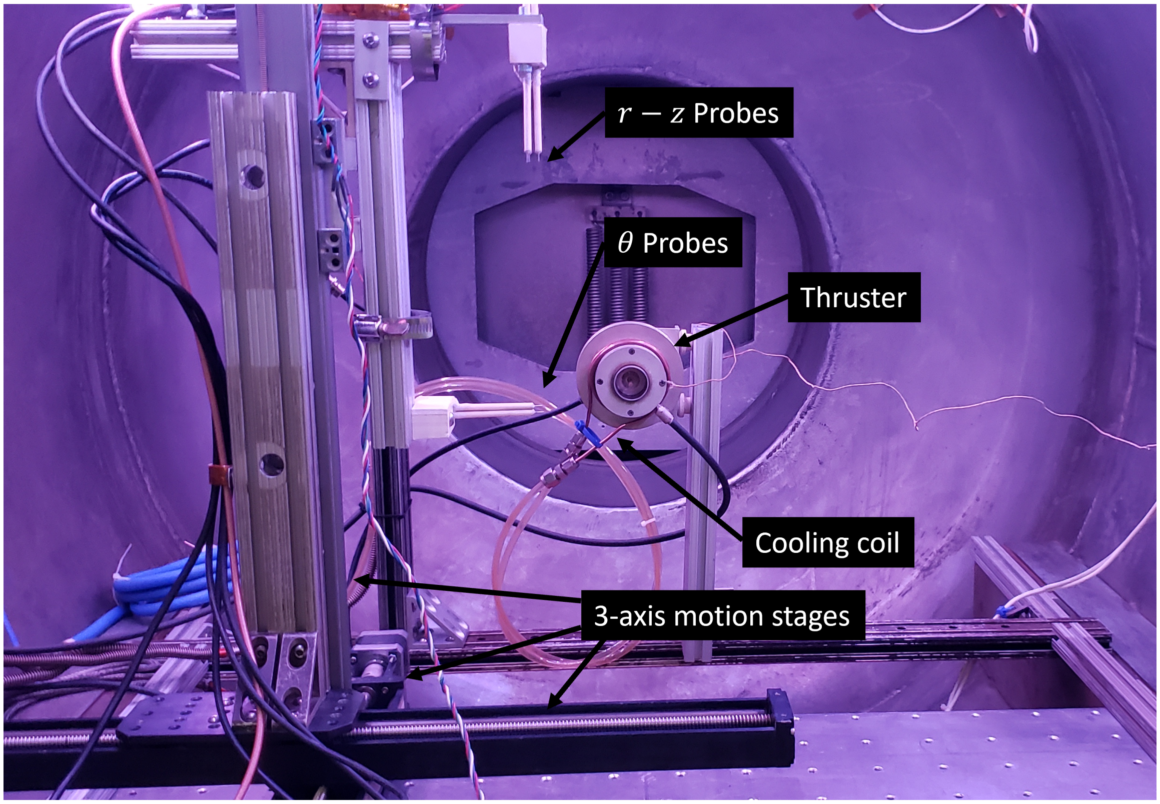

Figure 4.1: Image fo the thruster in Junior with probes mounted on three-axis motion stages and cooling lines.

downstream of the thruster exit and extending to 14 cm downstream with a tapered boundary in the r direction, as illustrated in Fig. 4.2b. We cooled the thruster body by flowing water through a copper coil wrapped around the thruster body. Figure 4.1 shows an image of this setup.

Figure 4.2b shows the microwave-driven plasma source we used for this study that was described in more detail in Chap. III as well as the magnetic field topology and coordinate conventions. We operated the thruster at 17 W delivered power and 2 sccm-Xe flow. During this test, we operated the thruster in Junior, which provided an operating backpressure of 4.3×10^{-6} Torr measured at the wall by a Stabil ion gauge during thruster operation. We employed two sets of translating probes to measure the time-varying and steady-state plume properties in the MN as shown in

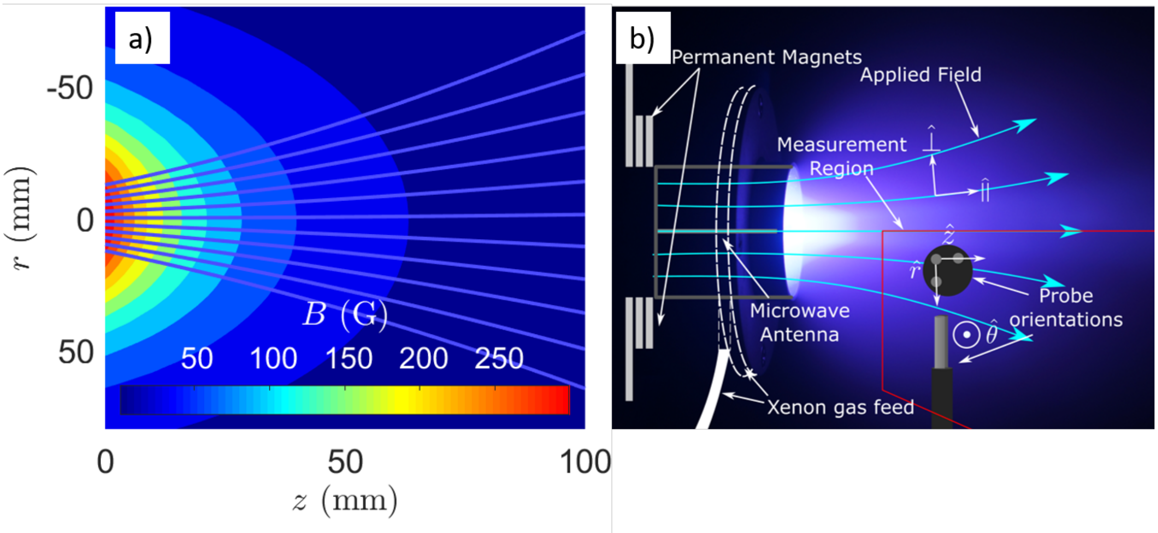

Figure 4.2: (a) Magnetic field contours, $\vec{B}$, and strength B of the applied field, and (b) Image of the MN operating on xenon along with notional probe orientations (not to scale) and coordinate conventions. The probes were operated in two orientations. In the first, their axis of symmetry was in the $\hat{\theta}$ direction (out of the page). In the second, it was in the -$\hat{r}$ direction (towards centerline). The thruster has a diameter of 25 mm at the exit plane ($z = 0$).

Fig. 4.2b, which provided steady-state values as per the analysis in Sct. 3.4 and wave measurements using the analysis technique described in Sct. 3.6. We separated these probes by 7 mm in the r and z direction and 5 mm in the θ direction.

4.3 Results

Figure 4.3 shows the measured ion density, plasma potential, and electron temperature in the plume. As indicated in Fig. 4.3b, the monotonic decrease in density downstream of the source is an indication of the expansion of the plume. The potential profiles follow a similar trend, decreasing monotonically in magnitude from the source. This potential profile is the consequence of an ambipolar field established between ions and electrons and is responsible for ion acceleration. Similar plasma property distributions have been observed in previous work [76, 31], and we therefore

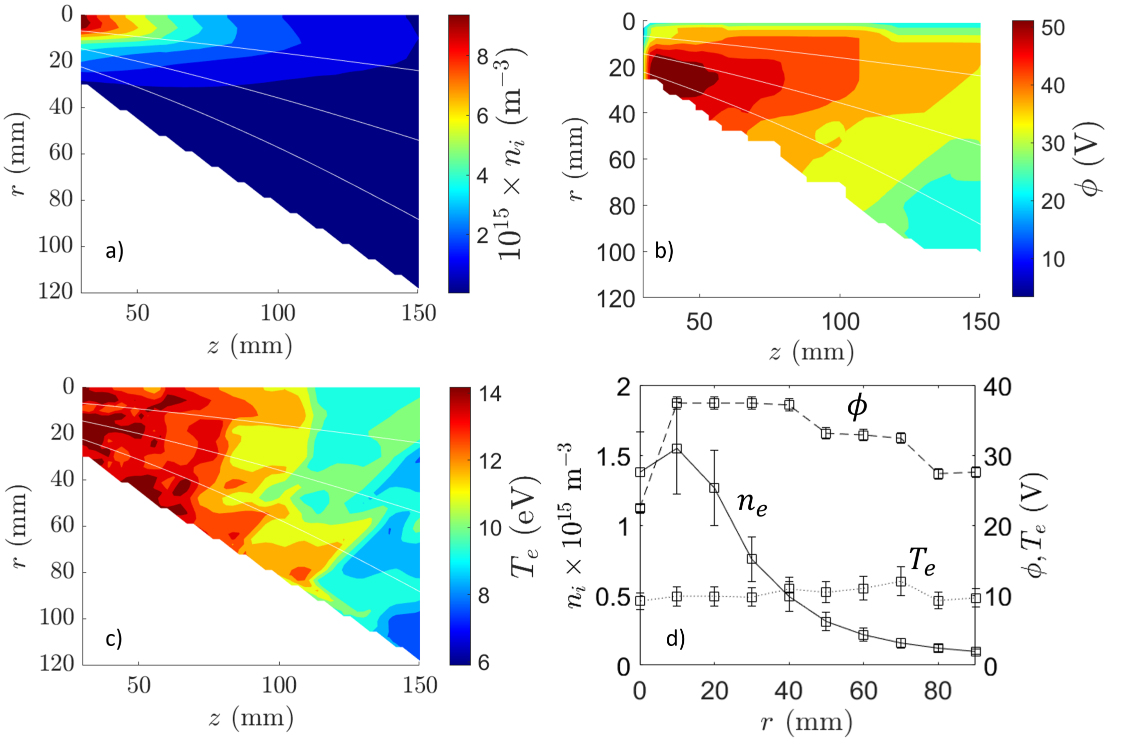

Figure 4.3: Two-dimensional maps of (a) ion density n_i, (b) plasma potential ϕ, and (c) electron temperature T_e at an operating condition of 17 W power and 2 sccm xenon flow rate. The axial origin ($z = 0$) is defined to be at the exit of the discharge chamber. (d) Radial profiles of each parameter at an axial slice $z = 120$ mm.

expect trends similar to what we have observed.

While our trends in plasma properties match various previous works, we also measure a departure from one recent work from Little and Choueiri [77]. The prior work observed a potential well appearing off-axis. The authors discussed this characteristic as evidence of electron attachment to field lines. The physical reasoning therein was that as electrons adhere to field lines but massive ions do not, the ions are free to flux across the field at a greater rate. This process is then fundamentally limited by the extent to which electrons are attached and the temperature of the ions, which dictates their diffusion rate. The reason for this discrepancy may be that the electrons in our device are more likely to diffuse across field lines and may exhibit a more upstream detachment point than the previous work, potentially as a result of the instabilities that we are investigating. In this case, electrons would quickly follow them to nullify any potential drop.

The potential instead decreases monotonically in the radial direction outside of $r \approx 20$ mm, with the exception of a small dip that appears closest to the the MN exit plane. This latter feature may be a consequence of the presence of the central conducting pin obstructing the plasma. According to this reference text, the formation of the potential peak off center may be a response to upstream ions diffusing faster than the more magnetized electrons due to a finite ion temperature. For the purpose of this study, however, the most salient feature is the existence of strong density and potential gradients off centerline and across the confining magnetic field topology. These gradients drive the azimuthal drifts that can serve as the energy source for the onset of instabilities. As we discussed in Chap. I, the dominant drifts in these devices are the electron $\mathbf{E} \times \mathbf{B}$ and diamagnetic drifts given by

$$v_D = \frac{\nabla p_e \times \mathbf{B}}{e n_e B} \tag{4.1}$$

$$v_E = \frac{\mathbf{E} \times \mathbf{B}}{B}. \tag{4.2}$$

We may calculate these velocities by taking the gradient of the data presented in Fig. 4.3 and further using the magnetic field vector shown in Fig. 4.2. We present the resulting values of these two drifts in Fig. 4.4.

Through the results in Fig. 4.4, we see that the diamagnetic drift is uniformly in the θ direction, whereas the $E \times B$ drift changes direction, as illustrated by the dashed line. Upstream and close to centerline, it is positive as well, resulting from the potential well on centerline (c.f. Fig. 3.6b). Progressing outwards or downstream yields a transition into a negative value. However, the magnitude of this drift is

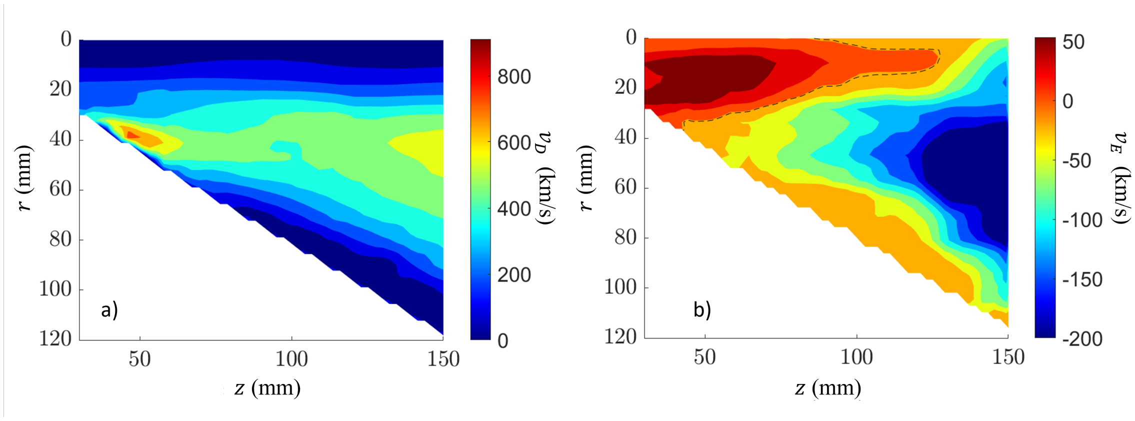

Figure 4.4: Azimuthal velocities induced by the a) diamagnetic drift and b) $E \times B$ drift.

dwarfed by that of the diamagnetic drift. We thus find that the electron drift maintains a diamagnetic character everywhere in the plume. We note that these results are commensurate with the diamagnetic loop measurements by Roberson [96], who similarly showed experimentally that the plasma currents on their device were universally diamagnetic.

We may next discuss the results of the ion saturation probes. With this in mind, we show in Fig. 4.5 examples of dispersion measurements in three directions $(\hat{r}, \hat{z}, \hat{\theta})$ at $(r, z) = (25, 50)$ mm. These results show the intensity of relative ion saturation fluctuations as a function of wavenumber normalized by the electron Larmor radius, $r_L = \frac{m_e v_{te}}{eB}$ (3 mm locally), and frequency normalized by the ion plasma frequency (4.4 MHz). Here we have corrected for an aliasing in wavenumber that stems from the finite distance between probe tips by following the procedure in Ref. [61] and concatenating the measured datasets, as described in Chap. III. This correction is the reason for the duplicate structures, such as the traces in the upper left and lower right of Fig. 4.5(b). The dispersion plots show that while there is little dispersion in the radial direction, there is an evident relationship between frequency and wave number in both the azimuthal and axial directions. This suggests the waves are propagating in both directions with frequencies extending up to the local ion plasma

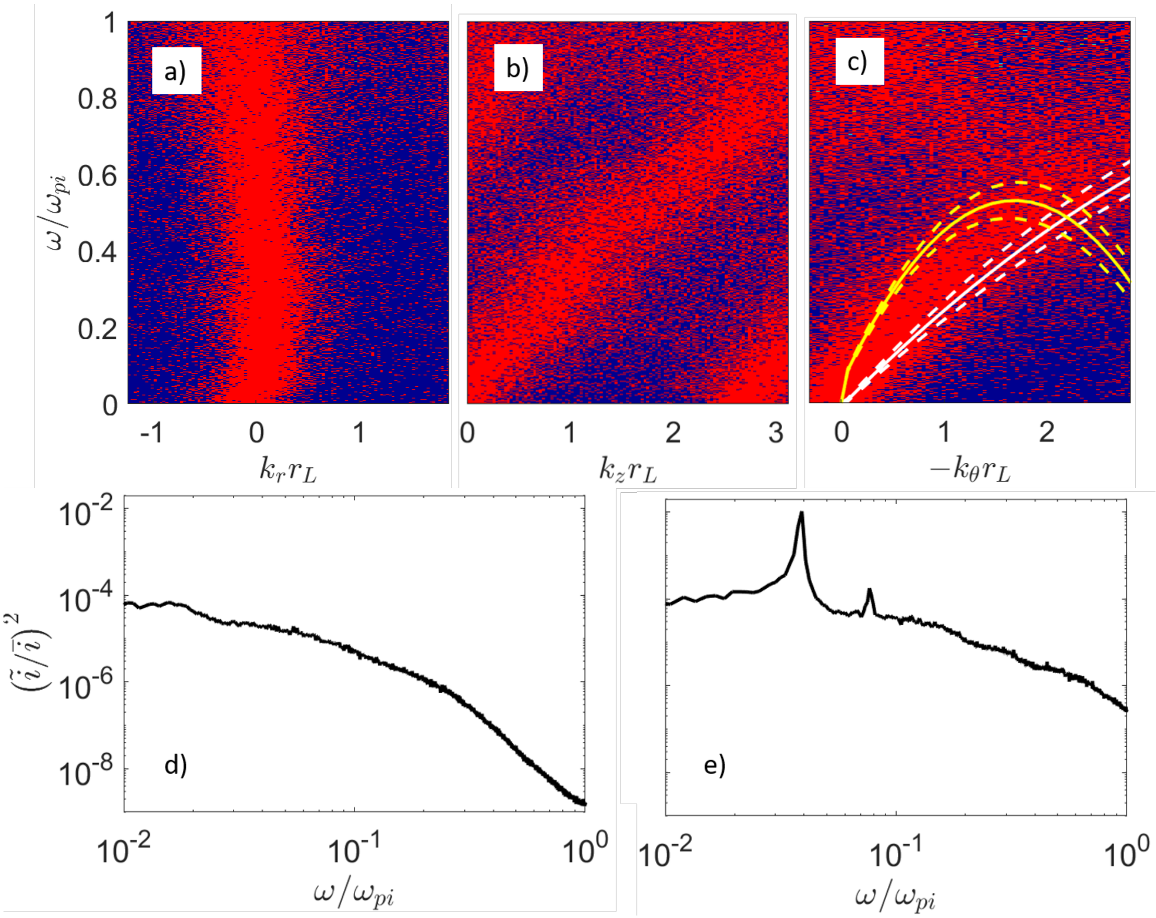

Figure 4.5: Measured dispersion relation in the (a) radial, (b) axial, and (c) azimuthal directions at the location z = 50 mm and r = 25 mm where the plot color scale has been saturated to illustrate the trends. (d) The power spectral density at the same point as (a)-(c), and (e) the power spectral density at z = 110 m and r = 50 mm. The white and yellow lines in (c) are the theoretical real solution and 10× the growth rate, respectively, of Eqn. 4.3 with confidence bars represented by dashed lines. Each plot presents frequencies and wavenumbers normalized to the plasma frequency and Larmor radius, respectively (left, bottom axes) as well as physical values (right, top axes).

frequency. These characteristics are consistent with the physical interpretation that instabilities can be driven unstable by gradient-driven electron drift in these devices.

Figure 4.5d shows the power spectrum corresponding to the dispersion plots in Fig. 4.5(a)-(c). These results indicate that these oscillations are broadband and turbulent in nature characterized by an inverse power law decay with frequency. We note that although we found that these azimuthal broadband modes persisted throughout the measurement domain, at the downstream edge ($z > 70$ mm), we also observed a more coherent oscillation superimposed on the power spectrum at approximately 13 kHz and a harmonic at 26 kHz (c.f. Fig. 4.5e). There were no unambiguous trends in dispersion for these modes, though similar low-frequency oscillations have been observed before in MNs and attributed to longitudinal ion acoustic or ionization waves [36, 1]. We return to a further discussion of these modes in Chap. VI. As the low frequency modes we measured did not appear everywhere and were not unambiguously azimuthal, we focus here instead on a more detailed analysis of the broadband oscillations in the drift direction.

To this end, we can interpret the dispersion measurements in the context of the linear theory for drift-driven waves in low temperature plasmas. First, we note that the azimuthal current is universally in the same direction as the diamagnetic current. This suggests at least by correlation that the diagmagnetic drift is the dominant energy source, since a wave connected to the $E \times B$ drift would change directions with this drift according to Fig. 4.4b. Second, Fig. 4.5a-c shows that the perpendicular wavelength is comparable to the electron Larmor radius. This implies that the wave is characterized by finite Larmor radius (FLR) effects and is therefore likely kinetic in nature. Finally, we measure finite propagation parallel to the magnetic field, implying that electron motion along the fields during an oscillation

Taken together, these features of the dispersion suggest that the observed mode may be a lower hybrid drift instability (LHDI) with finite parallel propagation [67, 21, 58]. As we explained in Chap. I, the LHDI with parallel propagation is driven unstable by an electron pressure gradient; it propagates in the direction of the electron diamagnetic drift velocity [67, 22]; it is characterized by FLR effects; and in low temperature, partially magnetized plasmas, it has been observed to exhibit a broadband power spectrum [22]. Moreover, the LHDI previously has been proposed as a dominant instability in higher power, fully-magnetized nozzles [92, 49] and appears prominently in magnetic reconnection transport studies [33, 57, 97, 90, 21, 22, 12].

To analyze the LHDI in our MN, we consider a dispersion relation adapted from the form derived by Carter et al. [22] in which they assumed a Maxwellian distribution of electron speeds in Cartesian coordinates, allowed for finite propagation parallel to the magnetic field and FLR. We presented this equation in Eqn. 2.115 but repeat it here for completeness:

$$0 = 1 - \frac{\omega_{pi}^2}{(\omega + k_\perp v_E)^2} + \frac{1}{k^2\lambda_D^2}\Bigg[1 + \frac{\omega - k_\perp v_D}{k_\| v_{te}} e^{-k_\perp^2 r_L^2/2} I_0\left(\frac{k_\perp^2 r_L^2}{2}\right) Z\left(\frac{\omega}{k_\| v_{te}}\right)\Bigg], \tag{4.3}$$

where $v_{te} = \sqrt{2T_e/m_e}$ is the electron thermal velocity, I indicates a modified Bessel function of the first kind, and Z is the plasma dispersion function. Here we have made the assumption that ions are much colder than electrons, $T_i \ll T_e$ and that the phase velocity component in the parallel direction is larger than the parallel electron drift, $\omega/k_\| \gg v_{e\|}$. This latter criterion is valid provided the electron drift speed is ambipolar (i.e. comparable to the ion drift speed)[56, 85].

In order to compare the theoretical result to our measurements, we use the probe results to estimate the terms in Eqn. 4.3. To estimate the field-aligned wavenumber ($k_\|$), we first fit lines to the wave intensity measurements in each direction. In doing so, we approximately define a phase velocity as the slope in each direction, $v_{\phi,(r,z,\theta)} = \omega/k_{(r,z,\theta)}$. We then project the resulting wavevector onto the local magnetic field, which results in the relation $k_\|/k_\theta = v_{\phi,\theta} B(v_{\phi,z}B_z + v_{\phi,r}B_r)^{-1}$. This approximation allows us to evaluate the relation between number density and plasma potential (Eqn. 4.3).

With these estimates, we then solve Eqn. 4.3 numerically for both real and imaginary components of the frequency as a function of perpendicular wavenumber, $\omega(k_\perp)$. Fig. 4.5 shows the result along with estimated confidence intervals. We generated these trends by assuming the uncertainty in the plasma measurements (according to Ref. [79]) is normally distributed, randomly sampling from these distributions, and re-calculating the dispersion. The indicated results reveal that the real component of the solution matches the measured dispersion within uncertainty. It is particularly notable that the change in slope with wavenumber is also reflected by the theoretical result. Moreover, the imaginary component of the frequency is positive for all wavenumbers in the observed propagation direction, indicating that LHDI waves are unstable and can spontaneously onset for these plasma conditions. Coupled with the marked agreement with the real dispersion, this fact suggests that the wave is likely LHDI.

We may repeat this measurement for every point in the plume at which we have wave measurements. We present in Fig. 4.6 the resulting wave intensity plots with an upper frequency cutoff of 400 kHz. We also show the radial and axial wave intensity measurements in Figs. 4.7 and 4.8, respectively. Fitting lines to each of these points and projecting the result onto the local magnetic field lines provides $k_\parallel$, which is necessary to solve Eqn. 4.3. We present the resulting map of $k_\parallel/k_\theta$ in Fig. 4.9.

With all of these values measured at every location, we are then prepared to evaluate the LHDI dispersion relation throughout the plume. We present the real solutions at each point as a white plot on each graph in Fig. 4.6. The growth rate (not shown for clarity) was universally comparable to that depicted in Fig. 4.5c.

In repeating this analysis throughout the plume, we found that the LHDI was unstable at all locations in the plasma and that the real component of the predicted relation matched the shape and direction of the measured dispersion everywhere. With that said, there were some regions where the magnitude of the predicted frequency differed by up to a factor of four from measurements. These areas were concentrated

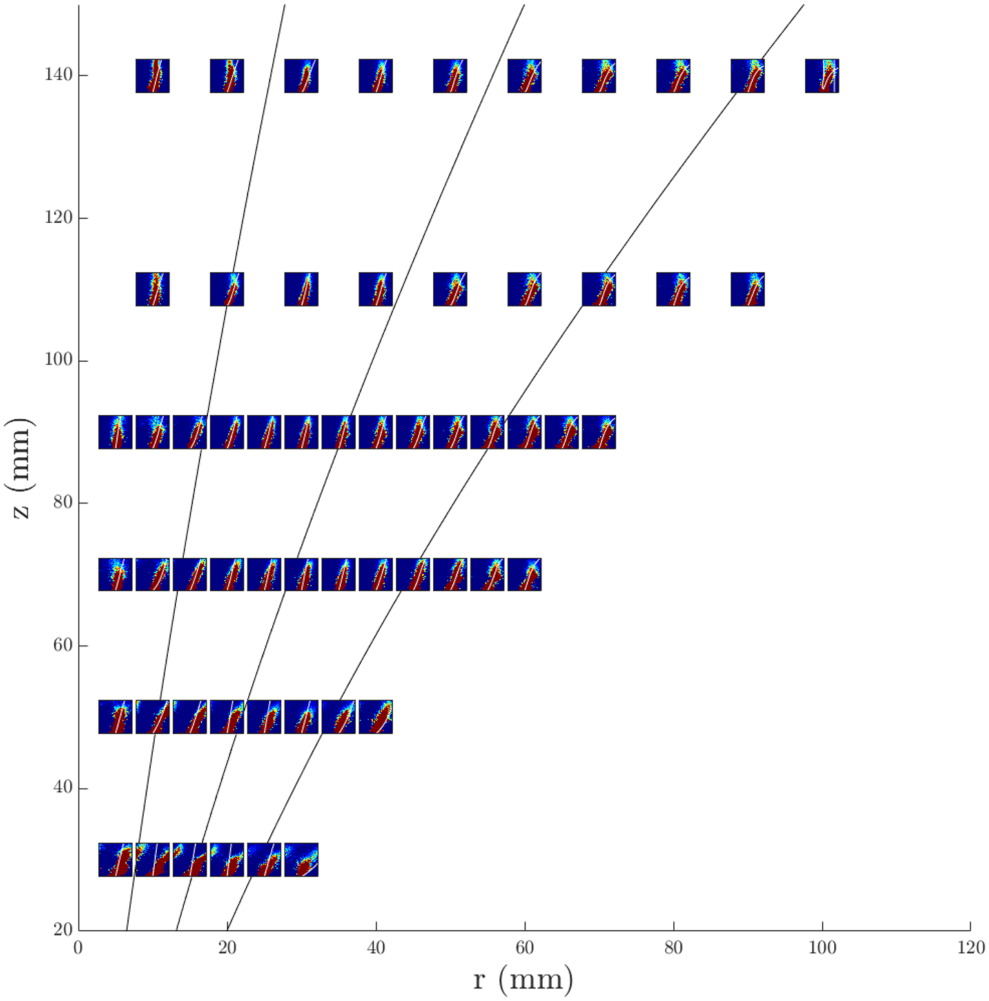

Figure 4.6: Beall measurements for each point in the plume with white plot overlay showing the real component of the solution to the LHDI dispersion relation (Eqn. 4.3). On each graph, propagation to the right indicates $+\theta$. The black lines behind the intensity plots represent magnetic field lines with the outermost line representing the last that originates in the discharge region.

off center and upstream ($r \gtrsim 20\text{mm}, z \lesssim 70\text{mm}$). This is not unexpected, however, given the number of simplifying assumptions we employed Eqn. 4.3. For example, these periphery regions near the vacuum interface have been shown to be characterized by effects not included in this derivation such as departures from quasineutrality

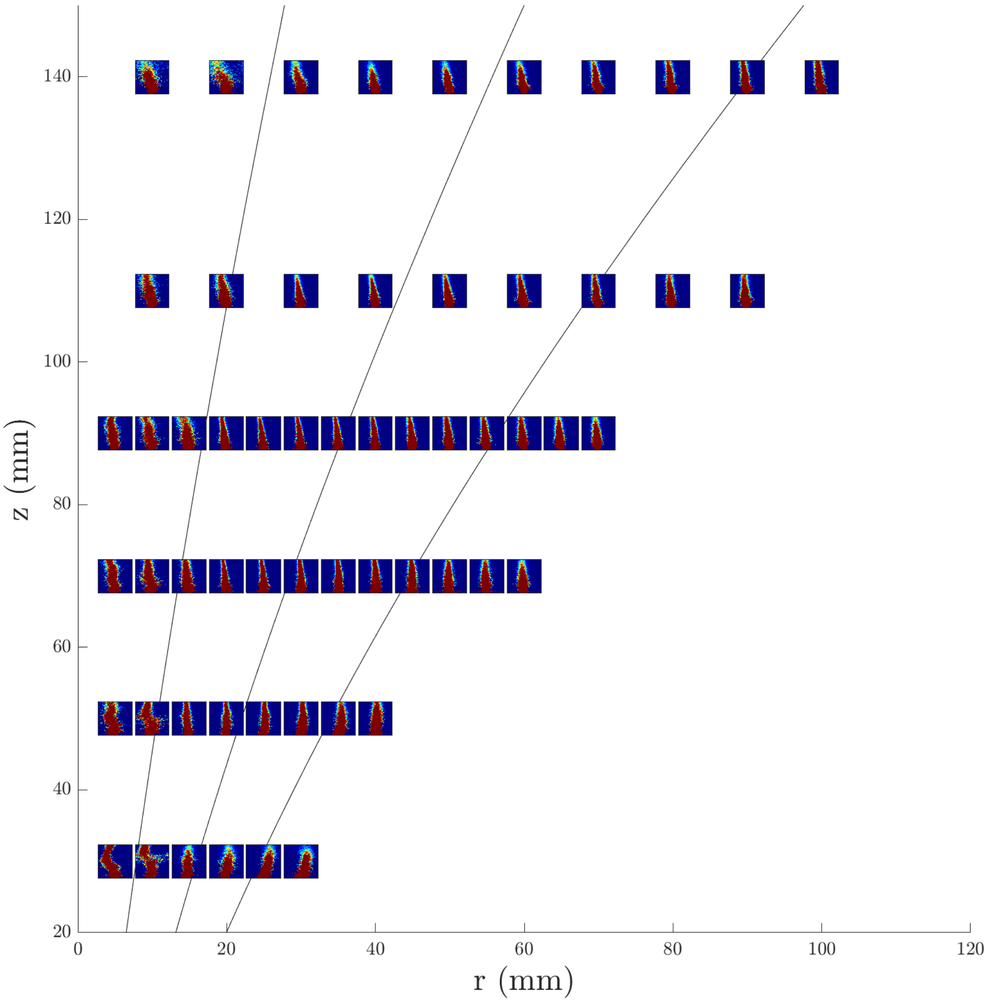

Figure 4.7: Radial wave intensity plots for each point in the plume. On each graph, propagation to the right indicates $+r$. The black lines behind the intensity plots represent magnetic field lines with the outermost line representing the last that originates in the discharge region.

[77]. The fact that we see marked agreement over the majority of the plume is quite notable considering the simplifications made in deriving Eqn. 1.

Given the evidence that the observed modes are LHDI, we finally can turn to the central question regarding its role in electron transport in the MN plume. Indeed, the growth of the LHDI has already been linked to enhanced cross-field motion in a

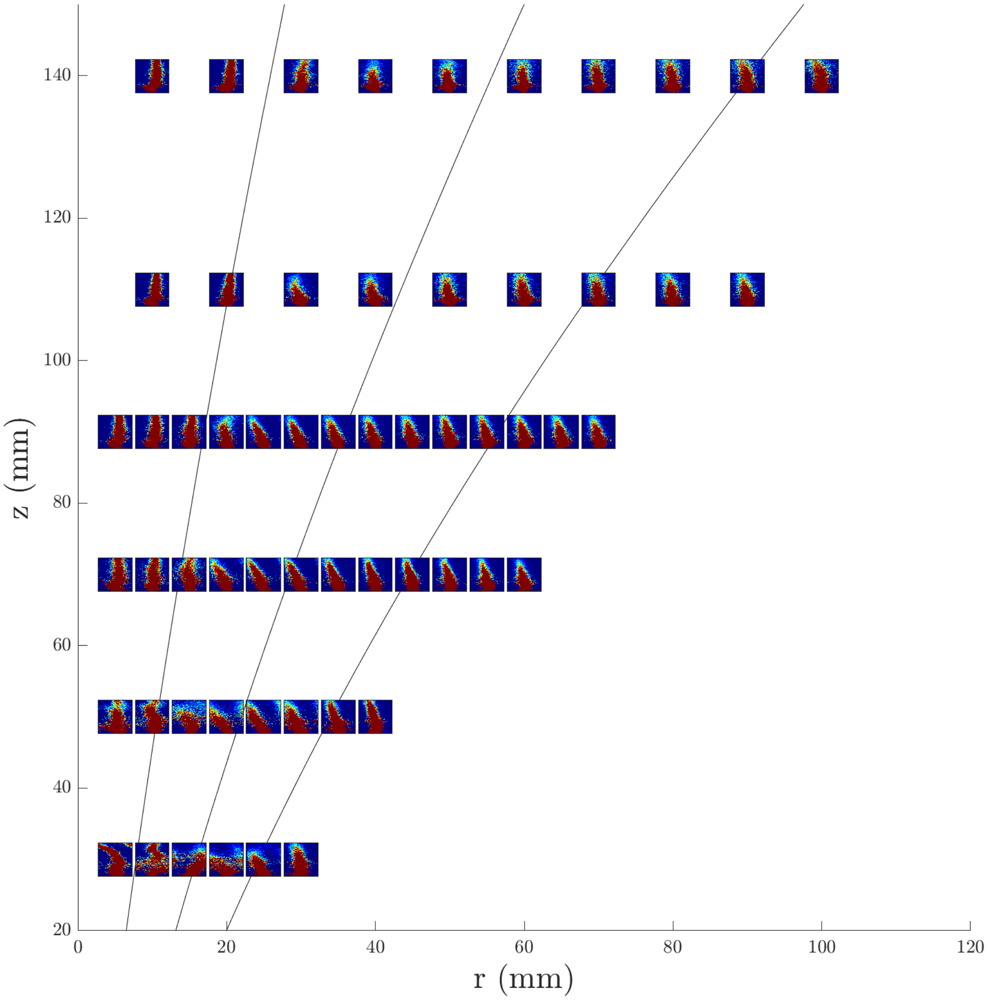

Figure 4.8: Axial wave intensity plots for each point in the plume. On each graph, propagation to the right indicates $+z$. The black lines behind the intensity plots represent magnetic field lines with the outermost line representing the last that originates in the discharge region.

number of other plasma configurations [22, 87, 54]. To evaluate its potential impact for our system, we adopt a quasilinear approach in which we introduce a transport coefficient, an effective collision frequency, attributed to the LHDI. Physically, this coefficient represents the rate at which the wave grows at the expense of the electron momentum. As the electrons lose energy to the wave growth, they slow down in a

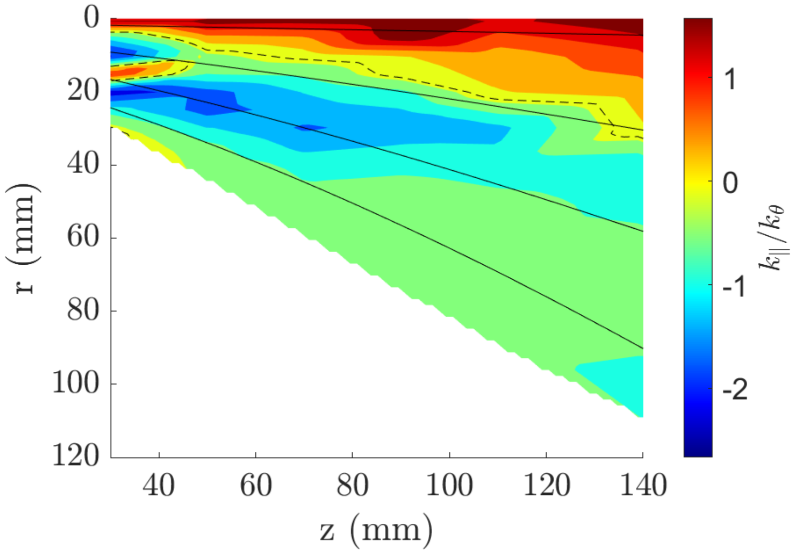

Figure 4.9: Ratio of parallel to perpendicular wavenumber $k_{\|}/k_{\theta}$. Black lines represent magnetic field lines originating from the discharge region. Positive values represent downstream propagation.

manner that manifests as a resistive drag force. This drag coupled with the background magnetic field facilitates a cross-field ($\hat{\perp}$) motion of the electrons. Following Refs. [35] and [22] as described in Chap. II, the quasilinear form for the effective collision frequency from the LHDI can be expressed as $\nu_{eff} = \frac{q}{n_e m_e v_{e_\theta}} < \delta E_\theta \delta n >$, where δ indicates an oscillating property and angle brackets imply a phase average. We use the theoretical expressions for these perturbed quantities from Eqns. 2.55, 2.105, and 2.59 to find

$$\nu_{eff,\theta} = \frac{v_{th,e}^2}{2(v_D + v_E)} \mathrm{Im}\Bigg\{ \sum_{\omega} \left(\frac{\tilde{n}_\omega}{n}\right)^2 \frac{k_\theta}{k^2} \Big[1 + (\omega - k_\perp v_D) \times$$

$$\frac{1}{k_\parallel v_{th,e}} Z(\frac{\omega}{k_\parallel v_{t,e}}) e^{-(k_\theta r_L)^2/2} \mathrm{I}_0((k_\theta r_L)^2/2)\Big]^{-1} \Bigg\}, \tag{4.4}$$

where $k = \sqrt{k_\perp^2 + k_\parallel^2}$ is the total wavenumber, $\tilde{n}_\omega$ denotes the density fluctuation for the component of the LHDI spectrum oscillating at frequency ω, and the summation is over all frequencies in the spectrum. To evaluate Eqn. 4.4, we use the measured values of the plasma properties inferred from Fig. 4.3 and the linear dispersion (Eqn. 2.115) to relate ω and $k_\perp$. For the density fluctuations at each frequency, we make the approximation that the measured ion saturation current scales with the density fluctuations, $\tilde{i}_{sat}/\bar{i}_{sat} = \tilde{n}_i/n_i \approx \tilde{n}_e/n_e$ as described in Chap. III [61, 48].

The effective collision frequency by itself, however, does not reveal much about the evolution of the plasma. To this end, we introduce the Hall parameter,

$$\Omega_e = \frac{\Omega_{c,e}}{\nu}, \tag{4.5}$$

as the ratio of the cyclotron frequency to the collision frequency. This value is a relative measure of the magnetization of a particle and indicates the number of orbits the particle will undergo before experiencing an effective collision event.

Following this approach, we show the resulting Hall parameter using effective collisions in Fig. 4.10b. For comparison, we also show the Hall parameter due to the classical electron-ion collision frequency (Ref. [105]), defined in this situation to be $2.18 \times 10^{-11} n T_e^{-3/2}$ for singly-charged xenon ions in Fig. 4.10a.

The resulting spatial plots illustrate that the Hall parameter attributed to the LHDI is orders of magnitude lower than its classical equivalent, indicating that it has a non-negligible impact on electron transport. Indeed, in the downstream region

($z > 100$ mm), the Hall parameter drops below 100, whereas classically, the Hall parameter is over 10,000. While this decrease in Hall parameter is substantial, values of 100 may still seem to imply confinement– electrons should not be able to cross field lines if they orbit hundreds of times before a collision event. However, we note that similar values have been determined to be sufficient to alter electron streamlines substantially in other crossed-field low temperature plasmas [15]. Moreover, if we assume an electron velocity in the $r - z$ plane that is comparable to the ion velocity [6] (around 10 km/s, estimated from a previous experiment on this thruster [122]), we can calculate a mean free path corresponding to the effective collision frequency. This value is around a centimeter, which is less than the thruster diameter and much less than the transit length through the plume, implying that electrons are affected by these effective collisions.

Furthermore, we may directly relate these results to previous studies on cross-field electron transport in magnetic nozzles. A recent study by Little and Choueiri [77] determined the impact of the electron inertia detachment mechanism (Chap. I) on inducing cross-field transport. They devised a metric for determining the electron detachment point based on the disappearance of the aforementioned off-axis potential well, indicating that electrons were able to cross field lines to even out the electric field. They then devised an estimate based on the electron inertia theory to predict this value, finding agreement between the theorized and measured points to within uncertainty. They further discussed the applicability of the field line stretching and finite collisionality theories, concluding that classical collisions would need to be two orders of magnitude more frequent to be significant in determining detachment. Our results show that, at least for our device, the role of instabilities may account for this two order of magnitude shortfall (Fig. 4.10). In light of these previous observations, our results in Fig. 4.10 suggest that the role of wave-driven resistive effects in electron transport cannot be ignored. [3, 77].

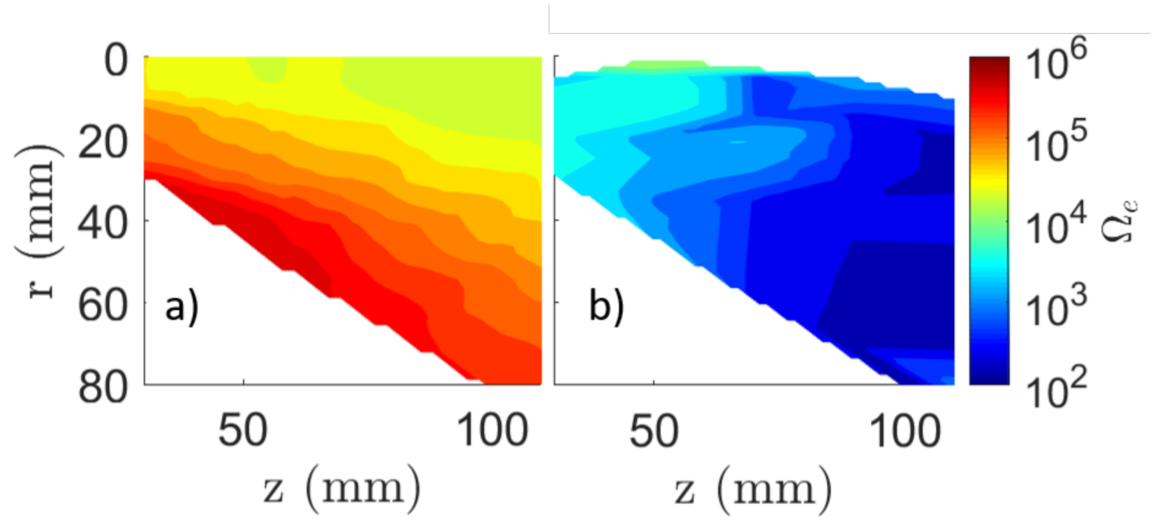

Figure 4.10: Spatial dependence of the Hall parameter for assuming (a) classical and (b) wave-driven collision frequencies. The axial origin ($z = 0$) is defined to be at the exit of the discharge chamber.

With this in mind, this non-classical resistivity will have a direct impact on the electron trajectories and thruster performance. To understand how, we may return to the discussion in Chap. I, where we established the link between direction of the azimuthal drift and the direction of transport. In the resistive case, an azimuthal drift dominated by the diamagnetic drift will induce divergent transport, whereas the opposite is true if the $E \times B$ drift dominates. As we have established in the results from Fig. 4.4, the diamagnetic drift dominates universally.

Since the electron motion is diamagnetic, as the LHDI grows at the expense of this drift, the effective azimuthal drag on the electrons combined with the magnetic field will push the electron trajectories radially outward and down the pressure gradient. This notably is in the same direction as predicted from FLR detachment [5, 77]. As discussed in these previous works, the increased divergence of the electrons drives a radially directed ambipolar field that pulls the ions away from thruster centerline. Even the ions close to centerline that are confined by the off-axis potential peak (Fig. 4.3(b)) are likely affected, as increased radial transport of electrons would lower this barrier, allowing ions to expand as well. Although, the effect is likely smaller for this population. The net effect qualitatively is an increased divergence and lower thrust. However, we cannot quantify the degree to which this effect will adversely impact thrust as we do not have a direct measurement of the ion and electron trajectories. We also note that while the LHDI will drive divergent electron detachment, it cannot be the only detachment mechanism for the electrons. Indeed, for the MN ultimately to produce thrust, the electrons must detach inward to follow the more convergent ions and maintain quasineutrality. This is in the opposite direction of motion that we anticipate based on the non-classical, wave-driven effect. Thus, while we anticipate based on our results that non-classical effects cannot be ignored in addressing the electron dynamics of our MN, the problem of global detachment and subsequent recombination of the species downstream remains an open question.

4.4 Conclusion

In summary, we have observed in this study azimuthally propagating waves in a low temperature, partially magnetized MN subject to an expanding magnetic field. We have determined based on linear dispersion relations that the observed instability is likely an LHDI, and we have discussed the implications of this mode on the macroscopic transport properties of the nozzle. While we have only considered the LHDI dispersion relation under the simplifying assumption of a uniform magnetic field, we show here that this linear relation still appears to be valid–agreeing quantitatively with wave measurements—in our expanding geometry. We have further explored the effect that the LHDI has on electron transport and concluded that it can enhance the effect of resistive transport by two orders of magnitude and in turn may lead to divergence. The discovery of non-classical transport in this class of low temperature plasma has broad implications in the field. Indeed, while turbulence-driven cross-field transport is a well established phenomenon in large scale, higher energy plasmas such as those encountered in energy research [30] and astrophysical systems, we have shown here that this effect is dominant in a lower temperature device. This suggests that classical theory for transport may need to be revisited in a wider range of low temperature plasma systems such as in probe analysis techniques [65, 106] and confined plasmas employed for plasma material interactions [119]. For MNs in particular, our finding that non-classical transport may dominate the electron dynamics is a paradigm shifting result for the understanding of electron detachment where historically such resistive effects have been neglected. In the next section, we expand our analysis of the LHDI to determine its effects on the electron energy balance.

CHAPTER V

Impact on Heat Transport from a Lower Hybrid Drift Instability

5.1 Introduction

In this section, we discuss the influence of the lower hybrid drift instability on electron thermodynamics. We first summarize the relevant conclusions from Chap. II and discuss in broad terms the influence of waves on heat flux and polytropic index. We next present the results of the background plasma measurements in the quasi-one dimensional sense. We then show the results from the wave-induced, field-aligned collision frequency calculations and differentiate them from those calculated in Chap. IV. We finally show the relevant results from the quasi-one dimensional energy equation, including heat flux based on a Fourier law, Ohmic heating, and wave heating.

5.2 Theory

Before presenting results, we will first show the final expressions for the values for each wave-driven term in the energy equation that we will use in this analysis. From Eqn. 2.63, there are three terms in this category– heat flux, resonant heating, and Ohmic heating.

To calculate heat flux based on a Fourier law, we require a form for the effective collision frequency. We return to Eqn. 4.4 but specify it to the value in the field-aligned direction. To this end, we must replace the azimuthal wavenumber with the parallel wavenumber and the azimuthal electron drift with the relative velocity between electrons and ions parallel to the applied field. The result takes the form

$$\nu_{eff,\parallel} = \frac{v_{th,e}^2}{2(u_{e,\parallel} - u_{i,\parallel})}\mathrm{Im}\Bigg\{ \sum_{\omega} \left(\frac{\tilde{n}_\omega}{n}\right)^2 \frac{k_\parallel}{k^2}\Big[1 + (\omega - k_\perp v_D)\times \frac{1}{k_\parallel v_{th,e}} Z\left(\frac{\omega}{k_\parallel v_{t,e}}\right) e^{-(k_\theta r_L)^2/2}\mathrm{I}_0((k_\theta r_L)^2/2)\Big]^{-1}\Bigg\}. \tag{5.1}$$

Evaluating Eqn. 5.1 provides a new difficulty not present determining the azimuthal component. Namely, while we were safely able to assume that the relative velocity between electrons and ions was the electron azimuthal drift, the field-aligned velocity is more difficult to evaluate. Ideally, direct measurement of the velocity distribution functions for electrons and ions would provide this value. However, as these were not available to us at the time of the experiment, we must make do with an approximation.

To provide such an estimate, we recount several aspects of magnetic nozzle operation previously illustrated in Chap. I. The first concept is that of ambipolar flow. While it is well understood that the electron and ion streamlines are likely not equal at every point in the plume [3], the total flow of each species out of the system must be equal to maintain charge balance. In the event that this ambipolarity does not hold, the thruster will immediately charge. As a result, the charge species that was escaping faster will be pulled back until balance is attained. For this reason, we begin with the assumption that the velocities are equal as they exit the nozzle. Since we do not have measurements at the exit plane, We will choose the point of this equality to be our most upstream measurement point, $z = 3$ cm.

We will then incorporate two concepts to predict the evolution of the velocity of each species. For electrons, we recall that their progression downstream may be modeled by an equation of continuity,

$$(n_e u_e A_e)' = 0, \tag{5.2}$$

which may in turn be integrated to find

$$u_e(z) = u_{e,0} \frac{\bar{n}_{e,0} \bar{u}_{e,0} A_{e,0}}{\bar{n_e} A}. \tag{5.3}$$

We further assume that the expansion area A is the effective area of the magnetic nozzle. This assumption is valid neglecting significant cross-field transport, but may break down if electrons separate from field lines. We will return to this assumption in Sct. 5.4.

For the ions, we recall that the only significant force on this species is the electric field. The equation of motion is

$$m_i u_i \frac{\partial u_i}{\partial z} = -q_i \frac{\partial \phi}{\partial z}. \tag{5.4}$$

We may then solve Eqn. 5.4 to find

$$u_i(z) = \sqrt{u_{i,0}^2 + 2\frac{q}{m}(\phi_0 - \phi(z))}. \tag{5.5}$$

This relation simply describes an exchange of energy between the plasma potential and the ion population.

Finally, we must invoke one further assumption to determine a boundary condition. To this end, we reference the work by Wachs and Jorns [122], who directly and noninvasively measured the ion velocity using laser diagnostics on the same device used in the present work. They found a downstream velocity of $\approx$ 10 km/s, which we assume as an exit velocity for this work. With this assumption, we are able to estimate the velocities of both the electrons and ions in this system.

The wave resonant term can be evaluated using the definition for $u_\parallel$ (Eqn. 2.108),

$$
\begin{aligned}
&n_e q_e m_e \langle \tilde{E}_\parallel \cdot u_{e,\parallel} \rangle = \\
&\qquad \int n_e \frac{m_e v_{t,e}^2}{4} \left(\frac{\tilde{n}_e}{n_e} \right)_\omega^2 (\omega - k_\theta v_{D,e}) \exp\left(-\frac{k_\theta^2 v_{t,e}^2}{2\Omega_{c,e}} \right) I_0 \left(\frac{k_\theta^2 v_{t,e}^2}{2\Omega_{c,e}} \right) Z' \left(\frac{\omega}{k_\parallel v_{t,e}} \right) d\omega.
\end{aligned}
\tag{5.6}
$$

In deriving Eqn. 5.6, we have made the approximation that $\tilde{\phi} \approx T_e \frac{\tilde{n}_e}{n_e}$. While this simplification is not strictly necessary as we could use Eqn. 2.105 to substitute $\tilde{\phi}$ for $\tilde{n}_e$ instead, this form is more tractable and will suffice for an estimate to the nearest order of magnitude. We will shortly see that this term is insignificant in the energy equation, and any correction that we may be missing is not enough to allow the wave resonant term to contribute to the energy balance.

Finally, to calculate ohmic heating, we directly apply the collision frequency results from Fig. 4.10 to determine the effective resistivity and take the product with the total azimuthal velocity,

$$
\mathbf{u} \cdot \mathbf{R}_{eff} \approx m_e n_e (v_D + v_E)^2 \nu_{eff,\theta}. \tag{5.7}
$$

Here we neglect the resistivity in the field-aligned direction, since the relative velocity is several orders of magnitude less than the azimuthal. We have further neglected any ion swirl that may be present, which is likely valid given the large mass of this species.

5.3 Results

Now that we have specified the forms required to calculate the appropriate terms in the energy equation, we next present the results of this analysis. We first present the magnetic field and steady-state plasma properties in the quasi-one dimensional paradigm then show each wave-driven term. We then predict γ based on the estimated heat flux value.

5.3.1 Magnetic field

To define the magnetic nozzle area, we may alternatively describe the magnetic field profile by a streamfunction. This substitution is valid assuming that the currents present do not influence the magnetic field. Under this assumption, Ampere's law reads

$$\nabla \times \mathbf{B} = 0. \tag{5.8}$$

We may also use the concept that the curl of a gradient is zero to define

$$\mathbf{B} = \nabla\psi \tag{5.9}$$

where we define ψ as the magnetic streamfunction. Assuming azimuthal symmetry, we find the partial derivatives of ψ as

$$B_r = -\frac{1}{r}\frac{\partial\psi}{\partial z} \tag{5.10}$$

$$B_z = \frac{1}{r}\frac{\partial\psi}{\partial r}, \tag{5.11}$$

with the boundary condition $\psi(r = 0, z) = 0$ [3, 76] and we have arbitrarily assigned the sign convention such that ψ grows away from centerline and $\nabla\psi \cdot \mathbf{B} = 0$. This

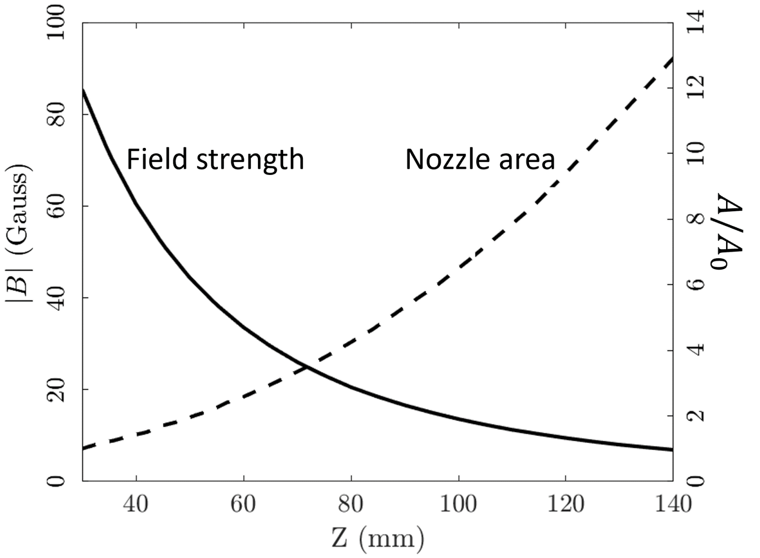

Figure 5.1: Area-averaged magnetic field strength (solid) and effective nozzle area (dashed) over the measurement domain.

latter relation implies that ψ is constant along a field line, allowing us to use its value to define the shape of the nuzzle. Given these characteristics, we may define the nozzle area as the region with $\psi < \psi_0$, where ψ_0 is the streamfunction value at the edge of the exit plane, $(r, z) = (12.5, 0)$ mm. Figure 5.1 presents the area-averaged magnetic field and the nozzle area. Since the magnetic field must maintain zero divergence, we have in the quasi-1D sense $(B_z A)' = 0$. Figure 5.1 shows that these two values indeed vary inversely to each other according to this law.

5.3.2 Steady-state plasma values

With a definition of the expansion area, we are prepared to determine the background plasma characteristics from the Langmuir probe in this paradigm. To find these measurements, we take area-averages of the results in Fig. 5.2 over the magnetic

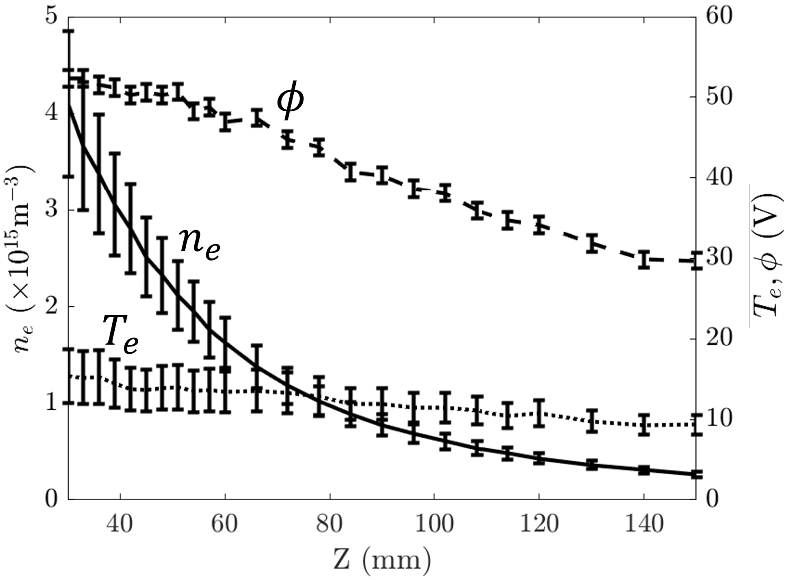

Figure 5.2: One-dimensional plasma properties.

nozzle area. This equivalence is found by

$$\bar{n}_e(z) = \frac{\int_0^R(z)2\pi r n_e r, zdr}{A(z)} \tag{5.12}$$

where R is the maximum radius of the magnetic nozzle at an axial distance z. We repeat the same calculation for the electron temperature and plasma potential to find $\bar{T}_e$ and $\bar{\phi}$. Figure 5.2 presents the results of this calculation. In this graph, error bars are found by standard error propagation techniques [79].

We next present the results of the velocity estimates from Eqns. 5.5 and 5.3 in Fig. 5.3. The ion velocity increases downstream, as is expected given the decrease in plasma potential. The electrons similarly accelerate as they expand, but to a lesser extent. This discrepancy may appear to indicate that total current ambipolarity is not conserved universally. However, this discrepancy can be resolved in two ways. First, it is possible that the effective area that we have used to define the electron expansion is not in fact the one they follow. If cross-field transport occurs, the electron streamlines will be different than the magnetic field, and the effective area would change. Given these results, it appears that the area would have to be smaller than the area of the magnetic nozzle. However, even if the area of electron expansion corresponds to the magnetic field perfectly, the difference between these velocities can expected given the ways in which we have defined them. Namely, while the electron velocity can be interpreted as an average velocity through the streamtube, the ion velocity is instead *effective*, merely approximated by the area-averaged potential drop, and thus may not correspond to the actual average. We take this value here to be representative in determining the general velocity difference between electrons and ions. An alternate scheme may be used to enforce current ambipolarity, but these require a full two-dimensional treatment to find the relative velocity everywhere, which is outside of the scope of the present work.

5.3.3 Effective collision frequency

Having defined the background plasma characteristics, we first discuss the field-aligned, effective collision frequency used in the Fourier law to calculate heat flux. To this end, we first calculate the local value of $\nu_{eff,\|}$ everywhere in the plume, then area-average them to find $\bar{\nu}_{eff,\|}$ as per Eqn. 5.12. We further calculate the classical equivalent representing small angle collisions between electrons and singly-charged ions,

$$\overline{\nu}_{e,i} = 2.18 \times 10^{-11} \frac{\overline{n}_e}{\overline{T}_e^{3/2}}. \tag{5.13}$$

Once we have performed this calculation, we are able to estimate the downstream heat flux. Figure 5.4 presents the total heat flux downstream qA for both classical and wave-driven collisions with the reference value of 17 W representing the total amount of power delivered to the thruster. We first observe that classical collisions predict heat flux roughly four orders of magnitude greater throughout the measure-

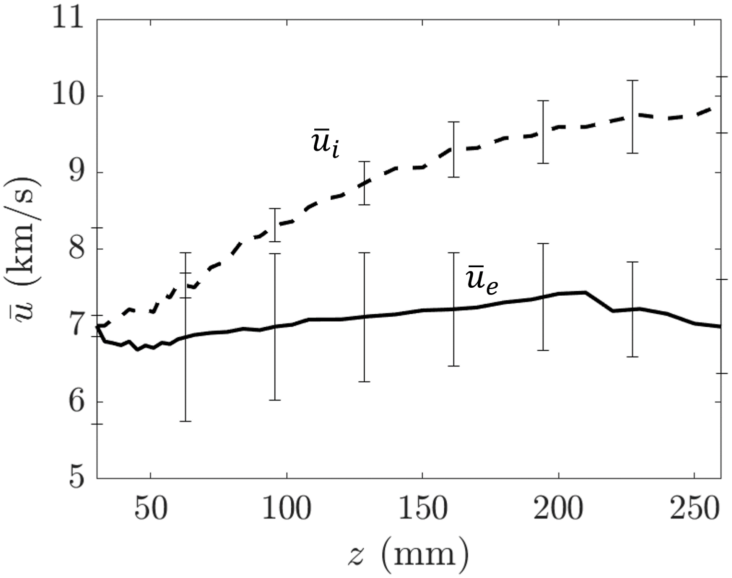

Figure 5.3: Ion (dashed) and electron (solid) velocities in the measurement domain.

ment domain. This trend is the result of relatively low densities and high electron temperatures, implying that the classical collision frequency is low. Wave-driven collisions, however, predict a total heat flux comparable to the total power available. Indeed, the prediction upstream is lower than 17 W, representing a physically possible value. As it increases downstream with the increased relative electron-ion velocity, it grows to roughly a factor of 5 higher than the delivered power, although the measured value is still within uncertainty. This analysis thus represents a drastic improvement over the classical prediction.

5.3.4 Wave-driven energy terms

After determining the heat flux, we may discuss its applicability to Eqn. 2.63 in relation to the other wave-heating terms. We present the area-averaged value of each term in Fig. 5.5. These results show that the resonant heating term experiences a decrease downstream. More importantly, however, is the fact that it is dwarfed by several orders of magnitude by the heat flux term. The divergence of the heat flux is thus the dominant term on the right hand side. For this reason, we will neglect

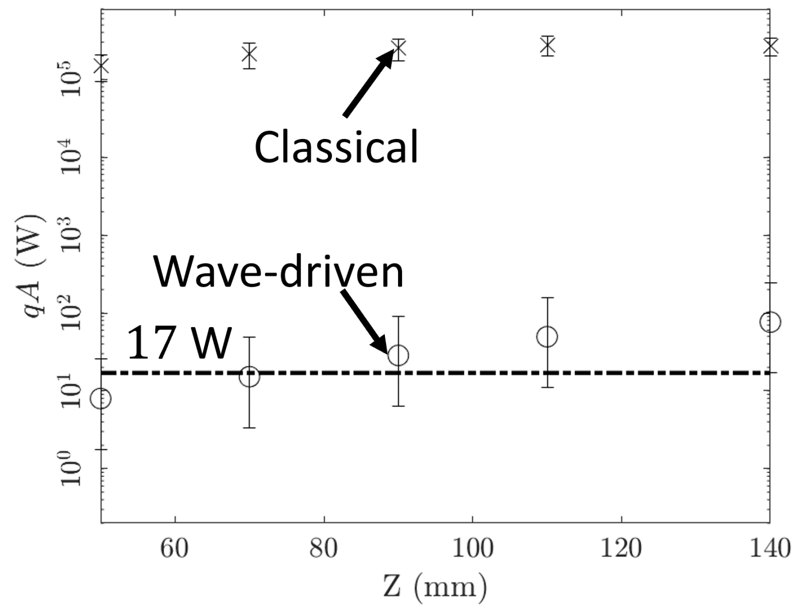

Figure 5.4: Heat flux as predicted by a Fourier law with classical, electron-ion collisions (x) and wave-driven, effective collisions (o). The dash-dotted line represents the total power delivered to the thruster during this experiment (17 W).

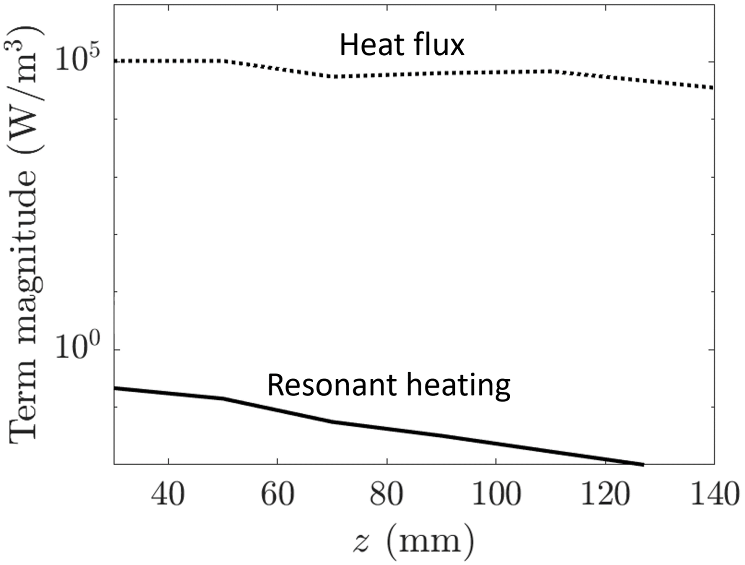

Figure 5.5: Area-averaged wave heating (solid) and heat flux term (dotted) as applied to the quasi-1D energy equation.

resonant heating in the remainder of the analysis in this section.

Having defined the significant contributions of the wave presence to energy bal-

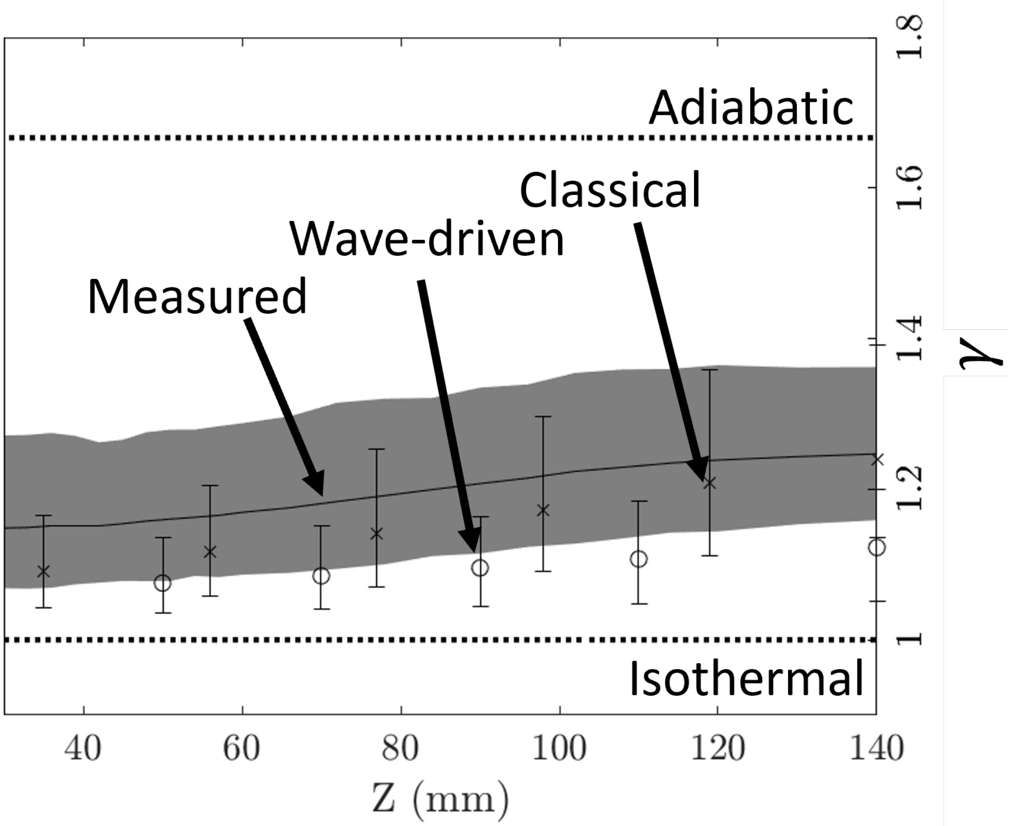

Figure 5.6: Gamma as directly measured with the Langmuir probe (solid, error in grey), as predicted by classical theory (x), and as predicted by wave-driven theory (o).

ance, we may determine how this value impacts γ. We return to Eqn. 2.74 to find γ, repeated here for convenience:

$$\gamma = 1 + \frac{\frac{m_e u_e \nu_e}{\alpha T_e} + \frac{T_e'}{T_e}}{\frac{3}{2}\frac{m_e u_e \nu_e}{\alpha T_e} - \frac{A'}{A} - \frac{T_e'}{T_e} + \frac{\nu_e'}{\nu_e} - \frac{T_e''}{T_e'}}. \tag{5.14}$$

We can again perform this calculation for both classical and wave-driven collisions and further compare it to the directly measured value, $\gamma = 1 + \ln(T_e)'/\ln(n_e)'$ [7]. For the measured and predicted values of γ, we define errors by repeating the analysis with randomly selected plasma values within error bars. The uncertainties presented represent the 5th and 95th percentiles of the resulting distributions.

We present the results in Fig. 5.6. Here, the solid line represents the measured value, and the shaded region is the uncertainty. The uncertainty of the predicted values are shown as standard error bars. The value that we measure begins as ≈ 1.15, then gradually increases to 1.3. These values fall well within the range of previously measured values [116]. The scaling of classical collisions predicts values within a few percent of the measured values. This result is expected, as it has been seen in previous work [75]. This results primarily from the collision frequency derivative term in Eqn. 5.14, as the term involving the magnitude of classical collisions itself is insignificant. The wave-induced collision frequency predicts a value slightly lower than the measured one, maintaining a value of ≈ 1.1 with only a slight increase downstream, although the error bars overlap with those of the measured values.

In these results, we confirm a finding of Ref. [75]. Namely, in predicting γ, it is generally not the magnitude of the collision frequency that matters, but rather the trends. In referencing Eqn. 5.14, the term involving the gradients dominates the result. Indeed, it takes more than an extra order of magnitude over the effective collision frequency everywhere to change the prediction of γ by more than a percent. The simple, Spitzer-Harm scaling of $\nu \propto n/T_e^{3/2}$ accurately matches the trend in observation, but the relatively stronger trend downward in the effective collision frequency decreases correlation with the observed value.

5.4 Discussion

We have seen so far that incorporating effective collisions predicts a physical heat flux and γ that agree with measurements within uncertainty. However, we must address several approximations that we have made in determining the Fourier law used to determine these values. First, a low frequency mode appears downstream that may affect these results (c.f. Fig. 3e of Ref. [52]). This mode has been considered as an ion acoustic mode in the past [36], but the conditions for this mode to arise have yet to be observed directly. Downstream, while the total energy of the incoherent mode falls, the energy of the low frequency mode increases. Indeed, it attains power spectral densities two or three orders of magnitude higher than the surrounding incoherent mode. Thus, it is possible that this mode, once thoroughly identified, will decrease this heat flux prediction further. It is moreover possible that its rise will soften the decay in ν_{eff}, increasing the prediction for γ.

The second error source involves the assumed relative velocity between electrons and ions. We have assumed thus far that the ions accelerate down the potential well, while the electrons expand based on continuity. However, the control volume (i.e. the area used in the continuity equation) was based solely on the boundary magnetic field. This assumption assumes zero cross-field transport; however, this is likely not true [3, 52]. Indeed, given that current-free thrusters based on these geometries produce thrust, electrons *must* eventually separate inwards. This fact results from the current-free nature in which ions only escape the inherently closed field if electrons do as well. Thus, the actual area that should be defined for electron expansion is somewhat indeterminate, but must approach that of the ions downstream, likely lowering the relative velocity. Our assumption of continuity thus likely underestimates the effective collision frequency and overestimates the heat flux.

To explore this last possible error source, we return to the α parameter that was previously defined. As we decrease α (thus decreasing the assumed relative velocity), the heat conduction decreases linearly. Indeed, including such a parameter at 10 predicts a downstream heat flux less than the thruster power. While this is not definitive proof, both of these error sources imply that we may be underestimating the effects of instabilities.

A final potential variation of this theory lies in the assumed closure scheme. When discussing heat conduction as restricted by classical collisions, the details of the closure scheme predict a factor, typically of order unity [24], by which the standard Fourier law must be multiplied. In this work, we have assumed this value to be unity.

However, a more thorough theoretical description of this phenomenon will determine what the factor in fact should be. Indeed, it is likely that this source of error will increase the predicted heat flux by a relatively small amount. This scheme would likely implement a Chapmann-Enskog closure scheme on the wave collision operator. However, such a theoretical undertaking is outside the scope of the present work.

5.5 Conclusion

In summary, we have formulated a Fourier law based on an anomalous collision frequency to explain heat conduction in an expanding magnetic field. We have determined that the field-aligned propagation present in the incoherent lower hybrid drift instability induces a parallel collision frequency significantly greater than the classical equivalent. We have further determined that this effective collision frequency restricts heat conduction to the point where less heat is flowing than is being delivered to the thruster. This comparison is true with respect to the mean prediction upstream, but is still true to within uncertainty downstream. This result differs notably from previous work analyzing a classical Fourier law on a similar system [75], where the heat flux was predicted to be an order of magnitude higher than the total power available. We further explored several sources of uncertainty in our analysis. One factor that we did not include in the heat flux determination was the low frequency mode, which grows downstream and reaches power spectral densities two orders of magnitude higher than the incoherent mode. Moreover, the relative velocity that we have assumed between the electrons and ions may differ. Indeed, given that the electron and ions should not deviate in particle flux away from the thruster to conserve global current ambipolarity (as we predict using our analysis represented in Fig. 5.3), it is possible that the relative velocity is significantly lower, which in turn implies a lower heat flux. Taken together, it appears that the presence of instabilities is likely significant in determining the thermodynamics of these systems.

CHAPTER VI

Identification of the Coherent, Low-Frequency Mode

6.1 Introduction

In this chapter, we return to the low frequency wave that was observed in previous chapters. We designed an experiment using high speed imagery based on the analysis of Sct. 3.8 to analyze this mode in more detail. We are particularly interested in determining if the mode sustains any global characteristics in the discharge region. To this end, we first introduce the experimental apparatus used for this test in 6.2. We then present the results of the high speed imagery for multiple flow conditions in Sct. 6.3. We analyze potential dispersion relations for the modes we observe in Sct. 6.4 and discuss our findings in the context of the downstream measurements of Chaps. IV-V. Finally, we discuss the potential implications of these findings in the context of thruster operation and previous research on the topic.

6.2 Experimental configuration

For this experiment, we operated on the second version of the ECR thruster discussed in Sct. 3.2. We operated the thruster at a constant 25 W of delivered power and varied the flow rate, taking measurements at 1, 2, and 4 sccm-Xe. These

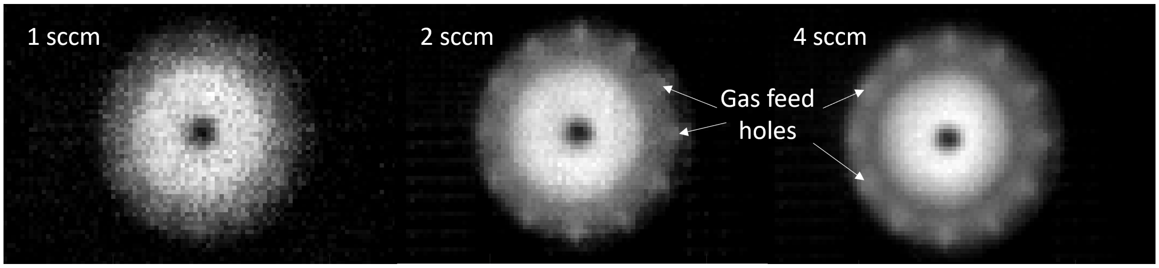

Figure 6.1: Example still images sampled at 300,000 samples/s from each operating condition.

corresponded to operating pressures in Junior of $7.11\times10^{-7}, 1.15 \times 10^{-6}$, and 2.03×10^{-6} Torr-Xe. We mounted the camera to a tripod and attached a zoom lens to focus on the thruster. For this test, we focused specifically on the end of the antenna, which maintained focus on the entirety of the discharge chamber. We covered the camera and viewport in a shroud to stop background light from affecting the image. We monitored the thruster visually through a second viewport and recorded imagery from the camera using Photron Fastcam Viewer. We took imagery at 300 kfps for a total of one second. Figure 3.14 presents the general arrangement of this experiment.

Figure 6.1 presents an example still in grayscale at each condition. At the higher flow conditions, the gas feeds are individually visible. This is likely a result of the elevated neutral pressure in those regions. In each of these conditions, it appears that the data we are able to resolve is primarily in the discharge chamber itself. The reason we claim this is that we make out very little light radially outside of the gas feed inlets. If we were able to see the expanding plume, we would have visible plasma in that region, but readings in that area are dominated by the noise. We thus make the assumption for the remainder of this analysis that the region we are analyzing is in the plasma generation region.

6.3 Results

In this section, will present the results of the Fastcam analysis of each flow condition in turn. For each of these results, we will present a total power spectrum as measured by averaging the individual power spectra of each pixel in the plume. We note that these values are left in arbitrary units. The reason for this is that the measurements are inherently line-averaged. The magnitudes of the oscillations are thus likely lower as recorded by the camera, but it is not possible in the current experiment to determine the extent. We then present the phase offset and amplitude graphs for each condition as discussed in Sct. 3.8.

6.3.1 1 sccm

We begin by analyzing the low flow condition. The initial spectral analysis on the modes present reveals two clear oscillations, as we show in Fig. 6.2. The first is dominant and coherent and appears at 12 kHz. The second is less coherent but still maintains a clear peak at 23 kHz. As the second mode is close to twice the initial mode, it may appear that it is simply a harmonic of the first. A harmonic may appear if a wave at a given frequency is not purely sinusoidal. In this case, the Fourier analysis will return a summation of the fundamental mode and its even multiples. However, harmonics are likely to maintain the coherency of the fundamental mode. In this case, the 23 kHz wave is less coherent than the 12 kHz mode, and thus may be a separate mode entirely.

Analysis of the phase offset and amplitude may provide further insight on this question. After measuring the raw imagery, we apply the analysis discussed in Sct. 3.8 to determine these properties. We present the results of these analyses in Fig. 6.2b-c for the low frequency mode and Fig. 6.2d-e for the higher frequency.

At 12 kHz, we observe that the oscillation is global, exhibiting no propagation in r or θ and indeed taking the same phase throughout the plasma. It may propa-

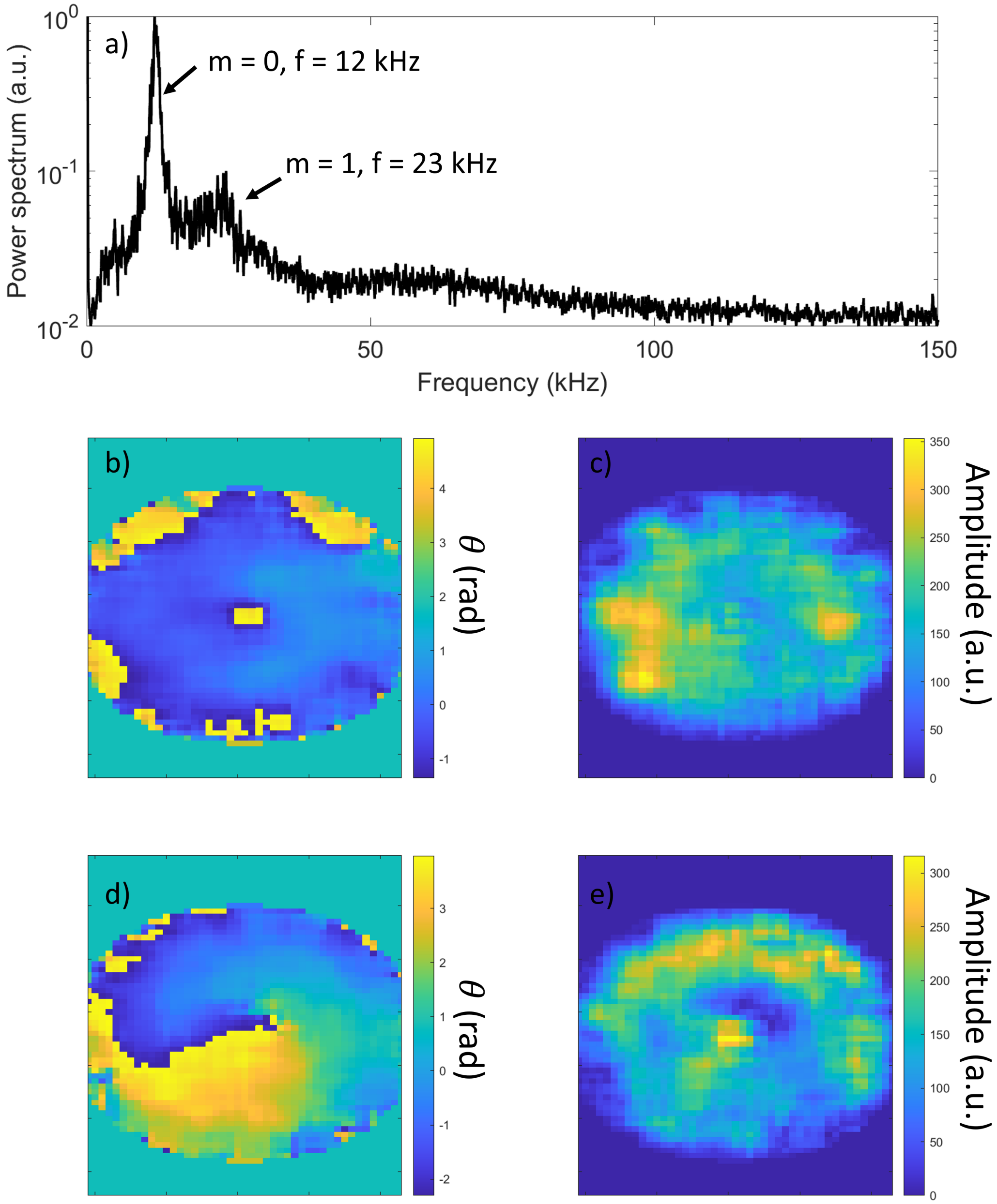

Figure 6.2: Results of high speed imagery analysis for 1 sccm-Xe flow rate. a) Power spectrum indicating two prominent modes. b) Phase analysis of the 12 kHz mode with c) the corresponding relative amplitude. d) Phase analysis of the 23 kHz mode with e) the corresponding amplitude.

gate axially, but we are unable to observe this property using these measurements. The amplitude graph shows no real trends other than a possible slight increase in magnitude halfway between the central antenna and the walls, although this trend is faint.

The propagation characteristics are different for the 23 kHz wave. Namely, as per Fig. 6.2d, there is a clear, $m = 1$ azimuthal mode that propagates in the clockwise direction. This characteristic is similar to the oscillations observed on similar geometries by Refs. [73, 62, 61, 53]. We may thus conclude that the drastic change in propagation characteristic implies that the 23 kHz mode is not a harmonic of 12 kHz, but rather a separate wave entirely.

6.3.2 2 sccm

When we increased the flow rate to 2 sccm, the propagation shifted significantly. The low frequency mode disappeared entirely, but the less coherent mode remained. However, its prominent frequency decreased to 18 kHz. We present these results in the same way in Fig. 6.3. We show the resulting power spectrum in Fig. 6.3a, and 6.3b shows the resulting phase data. This mode exhibits a similar $m = 1$ characteristic, although its phase is less well defined.

6.3.3 4 sccm

Finally, we present in Fig. 6.4 the results from the high flow condition. In this case, the $m = 1$ mode remains and further decreases in frequency to 4.6 kHz. Moreover, it assumes a stronger coherency than the first two cases. Indeed, it takes a similar character to the $m = 0$ mode in the low flow condition. Figure 6.4b shows that the oscillation is fully coherent, and we further observe in Fig. 6.4c that the magnitude of the oscillation maintains a clear peak roughly halfway between the center and the wall.

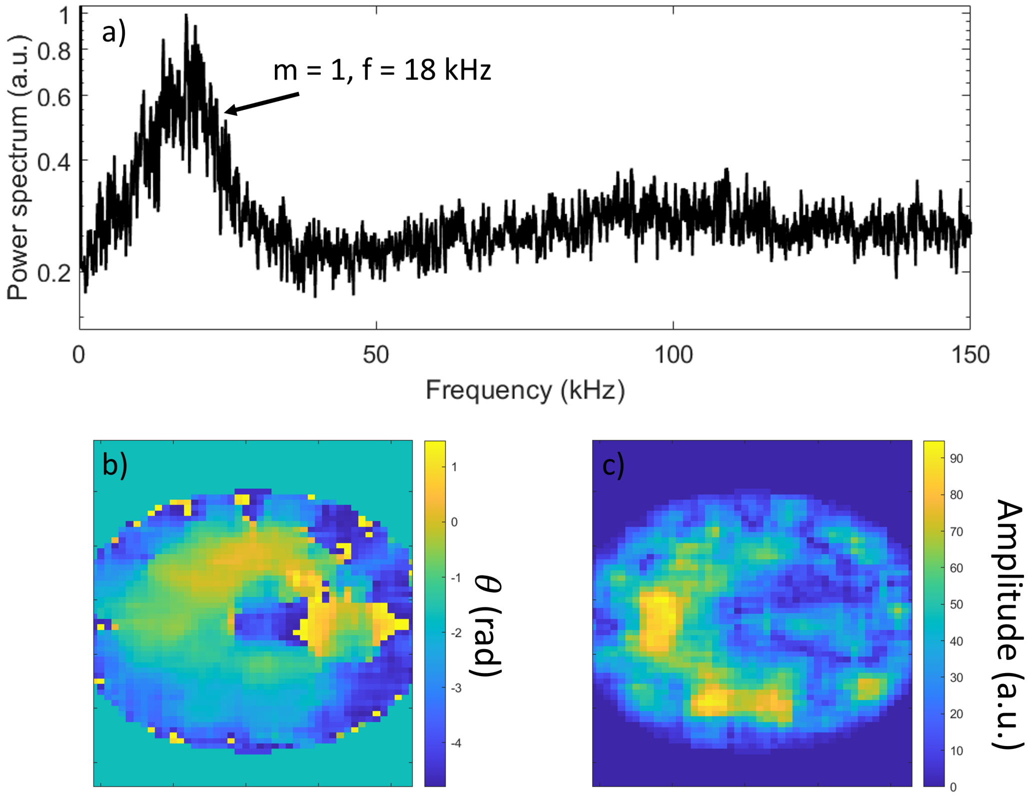

Figure 6.3: Results of high speed imagery analysis for 2 sccm-Xe flow rate. a) Power spectrum indicating the prominent modes at 18 kHz. b) Phase analysis of the 18 kHz mode with c) the corresponding relative amplitude.

6.4 Mode identification

We now proceed to identify the two distinct modes that we have seen. We first discuss the low frequency mode that we observe in the 1 sccm flow case as a potential ionization mode. We then identify the $m = 1$ mode as an anti-drift mode and discuss its characteristics, namely how the dominant frequency changes with flow rate.

6.4.1 Ionization mode

Ionization modes have been known to cause such low frequency oscillations in laboratory plasmas. Indeed, these types of oscillations have been theorized to cause

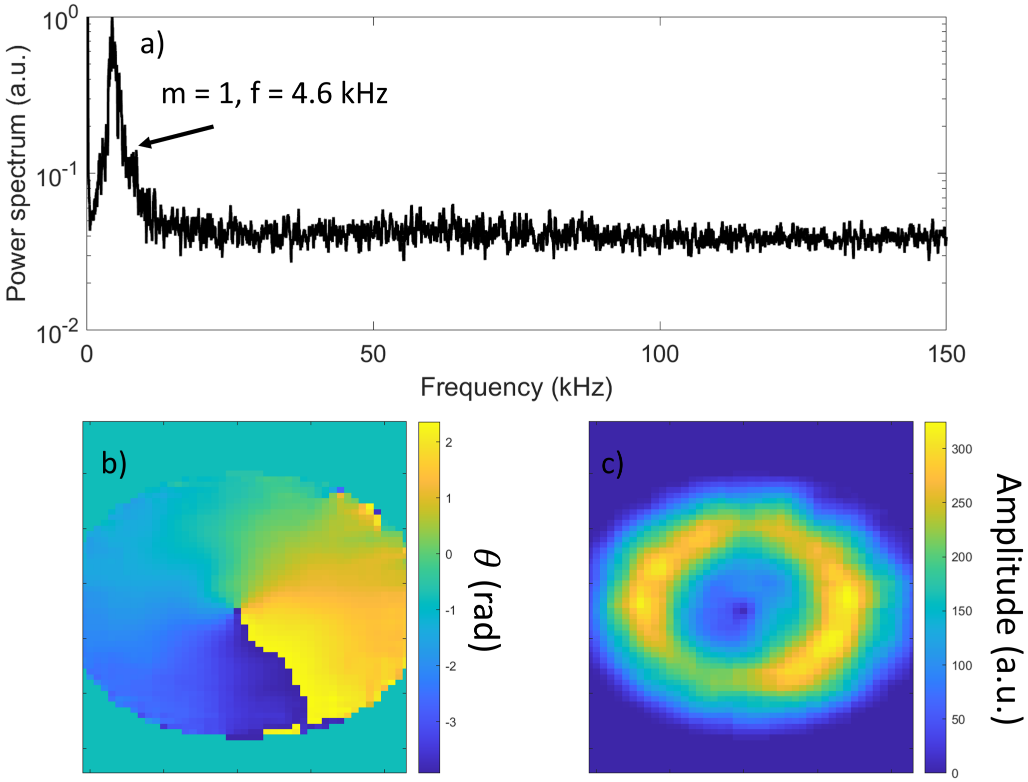

Figure 6.4: Results of high speed imagery analysis for 4 sccm-Xe flow rate. a) Power spectrum indicating the prominent modes at 4.6 kHz. b) Phase analysis of the 4.6 kHz mode with c) the corresponding relative amplitude.

the breathing mode in Hall thrusters [51] and are present in hollow cathodes [48]. One such mode has been previously investigated in Ref. [1] in the context of a magnetic nozzle. This prior work observed that a low frequency mode that they theorized was such an ionization wave, but that its instability relied on the presence of an electron population flowing upstream. Such a population was later found to not be present in that thruster [111].

Fundamentally, an ionization mode can be understood from a global analysis of the continuity equations for ions and neutrals. In this paradigm, we assume constant values of n and u for both species and integrate over the discharge volume. After assuming quasineutrality, this results in the following:

$$\frac{\partial n_i}{\partial t} + \frac{u_i n_i}{L} == n_n n_e \xi(T_e) \tag{6.1}$$

$$\frac{\partial n_n}{\partial t} + \frac{u_n n_n}{L} == -n_n n_e \xi(T_e). \tag{6.2}$$

Here, we have defined $\xi(T_e)$ as the ionization rate coefficient, which is typically considered a function of the electron temperature [50]. Applying the familiar perturbation analysis in time alone by setting $n_e \to n_{e,0}+n_1$, we may readily solve for the oscillation frequency of such a mode as

$$\omega = \frac{\sqrt{u_i u_n}}{L}. \tag{6.3}$$

As an estimate, we may approximate the resulting frequency by assuming that the ions exit the thruster with a velocity on the order of 3 km/s as per previous experimental evidence [121, 32] and that the neutrals flow at their thermal speed at room temperature ($\approx$ 300 K), u_n = 200 km/s. This cursory analysis predicts a frequency of 4 kHz. While what we observe is a factor of 3 higher than this value, the fact that this first approximation yields a value on the same order of magnitude implies that a further investigation of such a mode warrants further research.

One factor ignored by the prior work, however, was Ohmic heating. This effect has been discussed in the context of an ionization mode hollow cathode [47], in which effective resistivity from an ion acoustic wave drove the mode unstable. Physically, the electrons are heated by the acoustic mode to the point of further ionizing the background neutrals. As the neutrals were then depleted, electrons were continually energized, inducing a rise in temperature. Neutral density fluctuations mediated this process, and with sufficient heating the oscillation could be driven unstable.

An ionization mode could likely be driven unstable from heating in a magnetic nozzle as well. This effect would be most prominent upstream, where we have a simple source of heating– the antenna. Indeed, it is likely that, especially at low flow rates where temperature is high and neutral densities are low, we will see exactly this mode. To evaluate the applicability of this theory, however, a more thorough theoretical analysis would be necessary. As this mode only appears in one operating condition, we leave this effort to future work.

We may, however, evaluate the other modes that we see in this device. We proceed to do so in the following section.

6.4.2 Drift-driven mode

We consider the $m = 1$ mode to be a drift-driven instability. These modes can be described locally using the continuity and momentum equations for electrons and ions. For this mode, we will assume a slab-like geometry, with a constant magnetic field in the $\hat{z}$ direction, gradients in the $\hat{x}$ direction, and symmetry in the $\hat{y}$ direction, but are ultimately driven by the electron diamagnetic drift. These modes have been extensively studied in a variety of contexts [43, 98, 62, 53] and typically assume cold ions and electrons with no inertia. We must further assume quasineutrality ($n_i \approx n_e \approx n$), neglect higher charge states, and use conservation of momentum between species to let $\mathbf{R}_{e,i} = -\mathbf{R}_{i,e} = m_e n \nu_e (\mathbf{u}_e - \mathbf{u}_i)$. For our analysis, we will further assume that the ions are unmagnetized. In this context, we have the following fluid equations:

$$0 = \frac{\partial n_{e,i}}{\partial t} + \frac{\partial}{\partial \mathbf{x}} \left(n_{e,i} \mathbf{u}_{e,i}\right) \tag{6.4}$$

$$m_i n_i \left(\frac{\partial}{\partial t} + \mathbf{u}_i \cdot \frac{\partial}{\partial \mathbf{x}} \right) \mathbf{u} = -q_i \frac{\partial \phi}{\partial \mathbf{x}} - m_e \nu_e n \left(\mathbf{u}_e - \mathbf{u}_i\right) \tag{6.5}$$

$$0 = e \frac{\partial \phi}{\partial \mathbf{x}} - e \mathbf{u}_e \times \mathbf{B} - T_e \frac{\partial n}{\partial \mathbf{x}} - m_e n \nu_e \left(\mathbf{u}_e - \mathbf{u}_i\right). \tag{6.6}$$

In magnetic nozzles, collisions are typically assumed to be negligible. The reasoning behind this stems from the high ($\sim$ 20 eV) electron temperature and relatively low

$\sim 10^{15}$) number density. While collisions with neutrals have further been proposed as a source of collisionality in magnetic nozzles [29], ECR sources with hot electrons are likely almost fully ionized, and these collisions can be neglected [46].

With this understanding, we first simplify Eqns. 6.6 by neglecting collisions. Following a standard perturbation analysis, we find the dispersion relation to be [98]

$$\frac{k_y v_D}{\omega - k_y v_E} = \frac{T_e}{m_i}\left(\frac{k^2}{\omega^2}\right). \tag{6.7}$$

This mode is known as the modified Simon-Hoh instability, named after a similar wave with magnetized ions that was independently discovered by Simon [102] and Hoh [55]. This modified version was first investigated by Sakawa [98]. The solution to 6.7 can then be separated into its real and imaginary components,

$$\begin{aligned} \omega_r &= \frac{k_y c_s^2}{2 v_D} \\ \gamma &= k_y \sqrt{c_s^2 \frac{v_E}{v_D} - \frac{c_s^4 k_y^2}{4 v_D^2}}. \end{aligned} \tag{6.8}$$

Eqns. 6.8 reveal several fundamental characteristics of the modified Simon Hoh instability. First, its real frequency scales inversely with the electron drift. We alluded to this relation in Sct. 1.4.1 where we discussed this class of anti-drift modes. The growth rate further elucidates its mechanism for growth. As the second term is strictly positive, for the growth rate to be real (and, thus, for the wave to grow), the sign of v_E/v_D must be positive. In other words, the electric field and pressure gradients must be in the same direction.

However, we discussed in Sct. 1.2 that these drifts are likely in opposite directions in a global sense. That being said, that former analysis relies on the expansion into *vacuum*– the radial boundary condition for both potential and density was zero. The case may be different upstream, where a floating, conducting wall forms the boundary condition. In this case, given that the magnetic field is mostly axial, particle flux to the wall may be dominated by the unmagnetized ions, which would charge the thruster positive and impose a potential well close to centerline, implying an electric field co-aligned with the pressure gradient. Indeed, this idea corroborates the upstream potential well that we observed in the two-dimensional potential map that we presented in Fig. 5.2. While this is not proof that this pattern is present upstream in the current experiment, we will allow this trend to be present in our analysis.

We may further evaluate Eqns. 6.8 numerically with a the background plasma parameters. While we would ideally have these values measured directly, we do not have access to the parameters inside of the discharge. For this purpose, we will assume a few characteristics based on general geometry. First, we will let v_E and v_D be diamagnetic in accordance with typical magnetic nozzle operation. We will let v_E vary as a free parameter between 0 and v_D in accordance to Fig. 4.4. We will allow v_D to vary between values of $100, 150$, and 200 km/s, and assume an electron temperature of 20 eV. Finally, in reference to Fgi. 6.4b, we will assume the wave to be an $m = 1$ mode oscillating half way between the center pin and the thruster wall. This assumption results in a wavenumber $k_y = m/R = 160\ \mathrm{m}^{-1}$.

With the assumption of $v_E \parallel v_D$ implying that the wave may be unstable, we may further evaluate the applicability of this mode by analyzing the real frequency. As we have measured the frequencies present in each system, we may use them to solve for the diamagnetic drift velocity using the dispersion relation. Substituting in the definition of the diamagnetic drift, we find

$$\omega_r = \frac{ek_yB}{2}L_n \tag{6.9}$$

where we have defined the characteristic number density gradient length scale $L_n = n(\partial n/\partial x)^{-1}$. Since we analyzing the upstream region of the thruster, we may assume that the number density falls to zero at the thruster walls and take L_n to be the radius of the thruster. With $k_y = 160\text{m}^{-1}$ and B taken to be the resonant frequency of 875 Gauss, we find a predicted oscillation at 11 kHz. This prediction, albeit crude, lies well within the range of values that we observe, thus implying that the modified Simon-Hoh may be the wave that we have detected.

However, one immediate shortfall appears in this analysis. Namely, as we increase flow rate, we observe the frequency fall. Our analysis in Eqn. 6.9 implies that the observed frequency should be strictly a function of geometry– none of the parameters involved change between operating conditions. Finding the proper dispersion relation would likely involve a real frequency whose value changes based on the background plasma parameters.

There are a multitude of possible reasons that this theory may not match the observations perfectly. Any of the assumptions that we have made may be relaxed, and any one of these might modify the predicted frequency. It further may be that the magnetic field where the instability is being excited is not the resonant frequency, or that the mode is primarily growing at regions of the plasma where the number density gradient varies from the globally-averaged value that we have approximated. Indeed, while we have taken these global values in predicting the frequency, it may be that the growth of the wave occurs based on local parameters.

One further assumption that may need to be relaxed is that of zero collision frequency. We will now explore this last possibility in more detail. We may generalize the dispersion relation by incorporating collisions and parallel propagation. The result is a similar anti-drift mode [62, 42],

$$\frac{k_y v_D + i\frac{k_z^2 T_e}{m_e \nu_{e,z}}}{\omega - k_y v_E + i\frac{k_z^2 T_e}{m_e \nu_{e,z}}} = \frac{T_e}{m_i}\left(\frac{k^2}{\omega^2}\right). \tag{6.10}$$

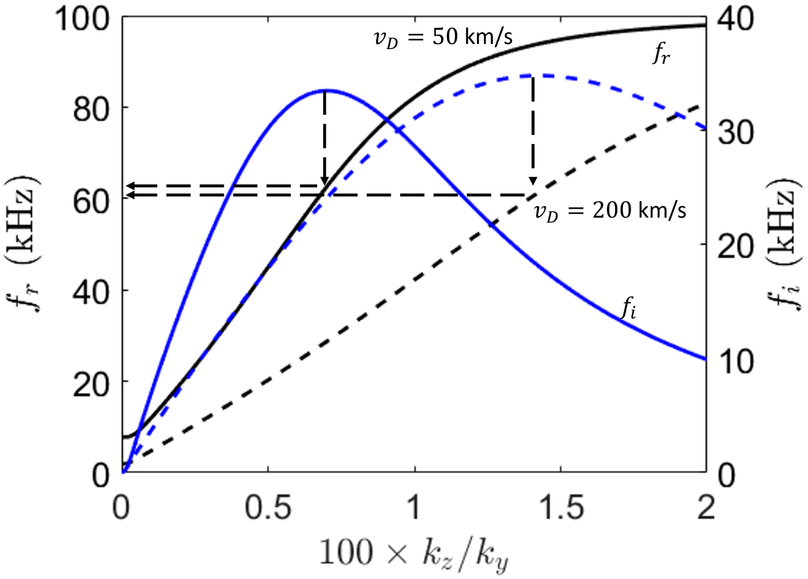

Figure 6.5: Example solutions for the collision-driven anti-drift instability with assumed parameters $\nu_e = 10^5$, $v_E = 0$,

We note here a new mechanism for instability. Namely, a finite collision frequency in the presence of propagation parallel to the magnetic field may drive an unstable mode in this system, which might appear even in the absence of the former requirement of $v_D \parallel v_E$. To analyze the applicability of this wave without direct measurements of the plasma in the discharge, we must vary several parameters. Namely, k_z, T_e, ν_e, v_D, and v_E are all free parameters. We may simplify this system initially by removing k_z as a free parameter through analysis of the growth rate. We expect that the visible wave is the one with the highest growth rate. For every case, therefore, we may choose k_z that maximizes growth rate. We show an example of this process in Fig. 6.5.

After reducing the problem by selecting k_z based on growth rate, will present the real frequency that we predict through this analysis. We will assume throughout that $v_E = 0$, since the aligned drifts are not the mechanism that we wish to investigate. We may further simplify by again expanding $v_D = \frac{T_e}{enBL_n}$ and repeating the assumption that L_n is equal to the thruster radius. In doing so, we reduce the problem to varying

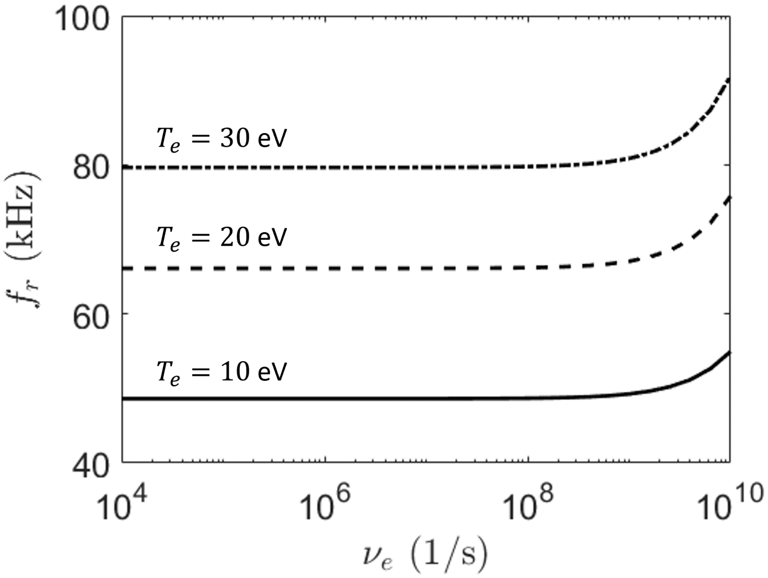

Figure 6.6: Example solutions for the collision-driven anti-drift instability with assumed parameters $\nu_e = 10^5$, $v_E = 0$,

only T_e and ν_e. For the temperature, we may allow for a fairly limited range. Given our experimental evidence in Chap. IV corroborated by previous measurements of electron temperature on similar devices (see Ref. [19]), we may allow the temperature to vary between 10 and 30 eV. We may then plot the solution for several select values as a function of collision frequency. Figure 6.6 presents the results of this analysis for electron temperatures of 10, 20, and 30 eV.

Two characteristics of these results are significant for our current discussion. First, we observe that the collision frequency does not significantly affect the real value of the solution. Indeed, until values over 10^8, the resulting frequency takes a constant value ±100 Hz, before finally sharply increasing. The second characteristic is the steady increase in predicted frequency with electron temperature. This second trend carries direct implications when comparing to our results. Namely, we observe an increase in observed frequencies at lower flow rates that may be connected to this trend.

Microwave plasma sources are known to sustain increased temperatures at lower flow rates [46, 19]. The physical reasoning behind this trend lies in the extent to which the gas flow is ionized. With a low ionization fraction, as the electrons gain energy from the ECR wave, they quickly lose it again to ionization collisions. Alternatively, when there are insufficient neutral particles, the electrons are able to energize unimpeded and achieve higher temperatures. This trend has further been observed directly in the plume of an ECR magnetic nozzle [32].

With this understanding, we may correlate the increase in flow rate in this experiment to a decrease in electron temperature. As the flow rate increases, the electron temperature likely decreases, and the observed frequency decreases as well. Thus, the collision-driven anti-drift instability accurately predicts the trends we see experimentally. However, it is clear that the magnitude of the predicted frequency is several times higher than our observations. While incorporating an $E \times B$ velocity in the same direction as the diamagnetic drift would fully account for this discrepancy as per the modified Simon-Hoh instability, one further possibility exists that does not rely on a radially-increasing plasma potential.

The other possibility to explain this difference is the incorporation of axial plasma velocity. Thus far, we have assumed that the ions are fully stationary and that the electrons only exhibit motion in the azimuthal direction. Relaxing this assumption allows for a Doppler shift of the predicted frequency into the lab frame. To establish the details of this idea, we will first recall the required global ambipolarity of the nozzle discharge. Assuming quasineutrality, we may thus take $u_{e,z} = u_{i,z} \equiv u_z$. The Doppler shift changes the resulting observed frequency to

$$\omega_r \rightarrow \omega_r + k_z u_z. \tag{6.11}$$

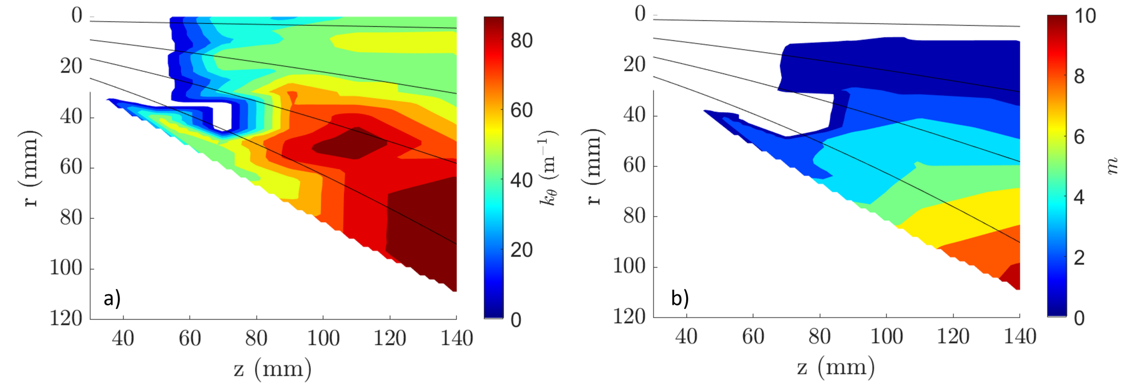

Figure 6.7: a) k_θ for the low frequency mode as measured with the ion saturation probes, and b) the corresponding azimuthal mode number with magnetic field line overlay.

This relation can further be understood in the context of the dispersion relation as

$$\frac{k_y v_D + i\frac{k_z^2 T_e}{m_e \nu_{e,z}}}{\omega - k_z u_z - k_y v_E + i\frac{k_z^2 T_e}{m_e \nu_{e,z}}} = \frac{T_e}{m_i}\left(\frac{k^2}{(\omega - k_z u_z)^2}\right). \tag{6.12}$$

Approximating an axial wavenumber of 10 m^{-1}, we see that we would only need an axial plasma velocity of a few km/s to reconcile this theory with what we observe. Thus, with significant parallel propagation, a Doppler shifted anti-drift wave may yield the oscillation that we observe.

6.5 Presence in the downstream measurements

As we noted in Chap. IV, we observed a low frequency mode akin to what we have discussed here using the ion saturation probe technique. This mode exhibited clear propagation in the azimuthal direction, and as such we theorize that it originated as a drift-driven mode. We present the results of this measurement in Fig. 6.7. As this low frequency mode did not universally appear, white space in this graph indicates that we did not observe the wave at that location. The frequency was universally 14 ±1 kHz, so we do not include these results in such a map.

Figure 6.7 presents a wave that propagates in the $+\theta$, or diamagnetic, direction but does not appear upstream in our measurements. It maintains a rotational character that may correlate with the theory of the drift-driven mode. It falls in the frequency range that we have seen with the high-speed imagery and maintains the same frequency ±1 kHz everywhere. However, we note that this wave does not appear to take the same $m = 1$ character downstream. This fact can be understood with the definition of $m = k_\theta r$. While the wavenumber indeed increases with radius, this increase is not linear. Instead, the effective mode then take values of up to 9. This trend appears to be a discrepancy with what we have observed with the high speed imagery.

We now introduce a few possibilities to resolve these apparent conflicts. First, the disappearance of the wave upstream may be a consequence of the lower hybrid mode. The strength of the latter mode is stronger upstream, and it may introduce effective noise that drowns the coherent mode. We may evaluate this possibility by showing several plots at the same radial location progressing downstream. Figure 6.8 presents such a result, where we show the power spectral densities at $r = 20$ mm and $z = 30, 50, 70,$ and 90 mm. With the first three points, we see indeed that the coherent mode is only able to appear as the magnitude of the LHDI decreases. The fourth data point does not support this hypothesis– its magnitude is far stronger than the LHDI at the upstream points. This fact implies that the wave may in fact be growing as it propagates downstream.

The reason for the breakdown in $m = 1$ character is less clear. It is worth noting that we do not have upstream measurements for this operating condition– perhaps the mode upstream is higher in this case. However, given that none of our imagery indicates such a mode makes this possibility unlikely. A more likely possibility is that the wave start acting locally instead of globally as the plasma expands. As the plasma expands and the collision frequency decreases, it is possible that $k_z \rightarrow 0$, which invalidates the local approximation required to understand the wave in the context of 6.10. In this case, assuming that an $m = 1$ mode appears in the condition for which we have downstream measurements, it is clear that the propagation characteristics change significantly downstream.

Now having observed downstream growth of this mode, we may discuss what may cause it to grow downstream. Recalling that it does not change frequency, it is likely that the mode originates upstream. Indeed, given the dependence of frequency on multiple plasma parameters in Eqn. 6.10, it is unlikely that the mode is driven the most unstable at precisely the same frequency everywhere. However, a wave originating upstream and propagating into the plume may maintain the same frequency.

Out of the mechanisms that we have discussed, the only one applicable to downstream growth is collisionality. Given that the drifts are in opposite directions downstream (cf. Fig. 4.4), the mechanism of the modified Simon-Hoh cannot cause growth in this mode. Moreover, the ionization mode is unlikely to be unstable in this operating condition. We have already seen in Fig. 6.3 that this global mode does not appear at 25 W and 2 sccm. If it indeed grows with the lack of neutral particles at high electron temperatures, it is unlikely to grow at the same flow rate and lower power. Furthermore, it does not predict the azimuthal character that we observe.

With this analysis taken together, it appears that the dominant low frequency mode in these plasmas is a form of anti-drift mode that originates upstream and propagates downstream at the same frequency. It then likely grows as it progresses due to similar processes. We now discuss these results in the context of thruster operation.

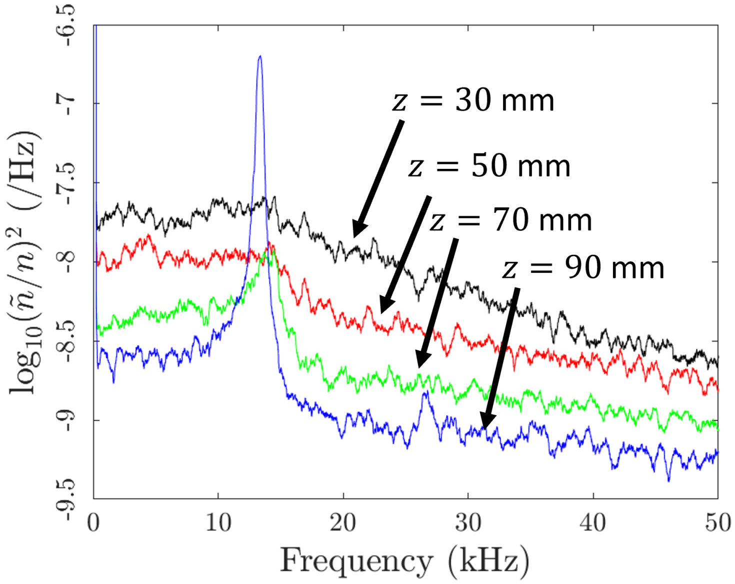

Figure 6.8: Power spectral densities at $r = 20$ mm and z ranging from 30 to 90 mm.

6.6 Impact on thruster operation

We have determined in this work that a coherent, low frequency mode is ubiquitous in this plasma. The dominant mode appears to take a global character at low flow rates, but an anti-drift mode appears as the flow rate increases. However, we have yet to determine the impact of this wave on thruster operation. As we have already discussed the significance of waves on plume dynamics in Chaps. IV and V, we focus our discussion here on the presence of a mode upstream.

Upstream azimuthal instabilities are likely to induce enhanced, effective resistivity that causes cross-field electron transport. Similar to how these waves cause electrons to diverge downstream, they likely do the same upstream since they propagate in the direction of the diamagnetic electron drift. However, instead of inducing a divergence loss, an electron impacting the wall is likely to neutralize [72]. These wall losses are likely a dominant source of energy loss in magnetic nozzles [69]. The extent to which this transport occurs is difficult to determine from these measurements. As previously stated, the reason for this is the inherent line-integrated nature of the measurement inhibiting us from acquiring an accurate value for its magnitude.

A global mode such as the ionization mode we have discussed here does not impact electron cross-field transport. The reason for this is that transport arises from effective resistivity perpendicular to the magnetic field. A global mode does not exhibit such behavior, but may induce field-aligned resistivity. To evaluate this directly, we require measurements of axial propagation in the source region. The impact of such an effect on thruster operation is similar to that produced by the field-aligned component of the LHDI discussed in Chap. V− namely, heat flux is likely inhibited, negatively impacting performance by restricting energy available to the ions downstream. We thus may conclude that both of these instabilities hinder thruster performance. However, further study is needed to determine the magnitude of this impact.

6.7 Conclusion

In this work, we have determined the presence of two modes in the discharge region of a magnetic nozzle. One, apparent only at low flow rates, takes a global character and may be an ionization mode akin to those observed in hollow cathodes [47]. The other, apparently ubiquitous, takes an $m = 1$ character upstream, but may . This mode is likely an anti-drift mode that is driven unstable either from a Simon-Hoh mechanism or from a finite collision frequency parallel to the magnetic field. From analyzing downstream measurements, we have determined that the low frequency mode observed in Chap. IV is likely a similar anti-drift mode. However, this mode likely originates upstream, as the dominant frequency does not change. The presence of such a mode likely induces wall losses upstream, as they propagate in the diamagnetic direction, so the resulting effective resistivity induces outward transport of the electrons. Moreover, the global mode may further inhibit heat conduction out of the source, which also hinders thruster performance.

CHAPTER VII

Conclusions and Future Work

7.1 Summary

Magnetic nozzles are strong candidates as long-duration propulsion devices due to their ability to run simply on exotic propellants, particularly those that may corrode similar devices with electrodes in contact with the plasma. Furthermore, their scalability implies that they may be applied to missions requiring both low and high powers. Despite their potential, they have only recently matured to the point of usability in space. Part of the reason behind this delay lies in the lack of understanding in several areas of how they operate, namely in the cross-field momentum transport of the electrons and the downstream heat flux. In this work, we have presented new understanding in how the plasmas in these devices operate throughout their expansion.

This work has aimed to address several questions pertaining to their operation from the perspective of an investigation into unstable modes. In particular, we have discussed four primary questions:

1. What instabilities may be present in the plume of a magnetic nozzle?
2. What role do these have in inducing cross-field transport?
3. To what extent do they inhibit downstream heat flux?

4. What modes may be present in the discharge region?

We have approached these questions both theoretically and experimentally. We began by building up the theory for a lower hybrid drift instability after previous work, then finding expressions for its effective resistivity. We then applied the concept of an effective collision frequency which transfers momentum between electrons and ions to a Fourier law to approximate its impact on inhibiting field-aligned heat flux. Finally, we investigated the presence of a coherent, upstream mode noninvasively.

7.2 Primary Findings

We first applied a set of ion saturation probes to the plume of a magnetic nozzle to measure number density oscillations directly. This analysis revealed a primarily azimuthal mode with wavenumber comparable to the electron Larmor radius that maintained finite propagation parallel to the applied magnetic field. Based on measurements of background, steady-state plasma values we theorized that this mode is likely a lower hybrid drift instability. We found that the dispersion for the LHDI was indeed unstable and predicted a dispersion relation that matched our observations.

We then applied quasilinear theory to determine the impact that these waves have on electron motion. We found that this mode likely induced cross-field transport at a rate several orders of magnitude higher than classical collisions, which is likely to be significant compared to other transport theories. We further determined that the direction of transport was divergent, implying that the electrons would expand more rapidly than the magnetic field. This effect would induce a radial electric field, which would in turn cause ions to diverge. This effect ultimately implies a divergence efficiency loss and negatively impacts thruster performance.

We next applied the effective collision frequency in the field-aligned direction to a Fourier law to determine the impact of the LHDI on heat conduction. We found this theory to predict heat flux orders of magnitude smaller than classical collisions might. Indeed, while Coulombic collisions predicted a heat flux that was orders of magnitude higher than the total power delivered to the thruster, effective collisions from the LHDI predicted values comparable to this number everywhere. We again concluded, since heat flux has been shown to be beneficial to thruster performance, that the field-aligned propagation of the LHDI is harmful to thruster performance.

Finally, we collected imagery at high speed of the discharge region to determine wave presence there. We found two coherent modes that were present. The first was a global mode that only appeared at a low flow rate. We theorized that this mode is likely an ionization mode akin to those seen previously on hollow cathodes. We further measured the presence of an $m = 1$ mode that was present at all flow rates, but was most coherent at high flow. We theorized that this is likely an anti-drift mode, which is driven unstable either by an electric field that is colinear with the pressure gradient or by a field-aligned collision frequency.

Ultimately, we have found that instabilities are likely harmful to thruster performance. Given the predominance of the diamagnetic drift, enhanced resistivity to the azimuthal electron motion induces outward transport. The resulting charge separation generates an electric field that will pull the ions outwards too, resulting in a divergence efficiency loss. Moreover, the presence of significant propagation parallel to the magnetic field inhibits heat flux. This phenomenon results in less total energy downstream available to accelerate the ions and hurts performance. Lastly, the presence of coherent modes upstream induce similar effects. While the magnitude of these effects currently remains unknown, an azimuthal mode may enhance plasma transport to the walls, reducing ionization efficiency, and an axial mode may further impede heat flux from the source region. Taken together, thruster designs should work to minimize the presence of all of these modes.

While we hope to have answered our research questions, this work has further prompted more potential projects. In the next section, we present several thoughts for what future work may entail.

7.3 Future Work

Our findings in this work prompt several further theoretical and experimental projects. The first question we would see addressed is that of the extent to which electron streamlines deviate from the applied field as a result of the LHDI. While we have theorized that the effect of these modes may be significant in inducing cross-field transport, the extent to which this occurs is still unknown. This question may be answered from two primary perspectives. First, wave-driven effects may be incorporated into simulation. While instabilities have been included in simulations recently [99], this work only applied them as a scaling factor. A full analysis may include the LHDI dispersion with saturation amplitudes to predict resistivity.

Momentum transport may also be investigated experimentally. One potential avenue for this investigation is a Thomson scattering diagnostic. This non invasive technique has the potential to record the velocity distribution functions of the electrons directly through the application of a laser. However, this diagnostic may be difficult to apply in the case of low electron bulk velocity. In the absence of this technique, other non invasive diagnostics may be used. In particular, it may be productive to measure the azimuthal ion velocity instead. This may be done using laser-induced fluorescence, which can selectively energize electronic transitions in a xenon ion. The Doppler shift in this process is often used to determine the velocity of an ion population. However, it may also be used to measure the effective resistivity. This idea results from the lack of other forces acting on the ions to influence them in the azimuthal direction. Measuring the evolution of the azimuthal ion velocity through the plume will provide an idea of the magnitude of resistive forces acting between electrons and ions, including any wave-driven effects. In the absence of direct measurement of electron cross-field velocity, the azimuthal resistivity may be used to approximate it using direct measurements.

Further work may also better determine the role of instabilities in determining downstream heat flux. From a theoretical perspective, one might follow the process of Chapman and Enskog [24] to find the true value of heat flux that might be present in the presence of waves. The original work performed a perturbative analysis on a steady-state Maxwellian distribution function. Through an expansion of Sonine polynomials, they were able to determine that the heat flux was simply a measure of the temperature gradient and the interaction time between particles– the Fourier law. However, to find a full form of the heat flux as inhibited by wave-driven effects, the wave collision operator $q\langle \tilde{\mathbf{E}} \cdot \partial f / \partial \mathbf{v} \rangle$ should undergo a similar treatment.

Heat flux may also be measured using noninvasive diagnostics. Namely, Thomson scattering may provide the electron velocity distribution function along field lines. With this value measured, one might integrate the second moment of the result to find the heat flux. This direct result may then be compared to that predicted by the instability theory to determine whether wave-driven effects are in fact dominant in determining its value.

In this work, we have presented the first identification of an unstable mode in the plume of a magnetic nozzle and contributed to the understanding of low frequency modes originating in the source region. While we have theorized as to how they might impact momentum and heat transport of the electrons, an ideal continuation of this work would further develop the theory behind these predictions and further support the theory with direct measurements of the electron velocities.

BIBLIOGRAPHY

BIBLIOGRAPHY

[1] Aanesland, A., C. Charles, M. A. Lieberman, and R. W. Boswell (2006), Upstream ionization instability associated with a current-free double layer, *Phys. Rev. Lett.*, *97*(075003), doi:10.1103/PhysRevLett.97.075003.

[2] Ad Astra (2021), VASIMR® VX-200SS plasma rocket completes record 88-hour high power endurance test, *Tech. rep.*

[3] Ahedo, E., and M. Merino (2010), Two-dimensional supersonic plasma acceleration in a magnetic nozzle, *Phys. Plasmas*, *17*(17), 7.

[4] Ahedo, E., and M. Merino (2011), On plasma detachment in propulsive magnetic nozzles, *Phys. Plasmas*, *18*(5), doi:10.1063/1.3589268.

[5] Ahedo, E., and M. Merino (2011), On electron inertia and current ambipolarity in magnetic nozzle models, in *International Electric Propulsion Conference*, IEPC-2011-050, Wiesbaden, Germany.

[6] Ahedo, E., and M. Merino (2012), Two-dimensional plasma expansion in a magnetic nozzle: Separation due to electron inertia, *Phys. Plasmas*, *19*(083501), 43,504, doi:10.1063/1.4739791.

[7] Ahedo, E., S. Correyero, J. Navarro, and M. Merino (2020), Macroscopic and parametric study of a kinetic plasma expansion in a paraxial magnetic nozzle, *Plasma Sources Sci. Technol.*, *29*(4), 045,017, doi:10.1088/1361-6595/ab7855.

[8] Anderson, J. D. (1990), *Modern Compressible Flow: With Historical Perspective*, vol. 12 ed., McGraw-Hill, New York.

[9] Arefiev, A. V., and B. N. Breizman (2004), Theoretical components of the VASIMR plasma propulsion concept, *Phys. Plasmas*, *11*(5), doi:10.1063/1.1666328.

[10] Arefiev, A. V., and B. N. Breizman (2005), Magnetohydrodynamic scenario of plasma detachment in a magnetic nozzle, *Phys. Plasmas*, *12*(043504).

[11] Arefiev, A. V., and B. N. Breizman (2008), Ambipolar acceleration of ions in a magnetic nozzle, *Phys. Plasmas*, *15*(4), doi:10.1063/1.2907786.

[12] Bale, S. D., F. S. Mozer, and T. Phan (2002), Observation of lower hybrid drift instability in the diffusion region at a reconnecting magnetopause, *Geophys. Res. Lett.*, *29*(24), doi:10.1029/2002gl016113.

[13] Beall, J. M., Y. C. Kim, and E. J. Powers (1982), Estimation of wavenumber and frequency spectra using fixed probe pairs, *J. Appl. Phys.*, *53*(6), doi:10.1063/1.331279.

[14] Bellan, P. M. (2008), *Fundamentals of Plasma Physics*, Cambridge University Press.

[15] Boeuf, J. P., and L. Garrigues (2018), E x B electron drift instability in Hall thrusters: Particle-in-cell simulations vs. theory, *Phys. Plasmas*, *25*(061204), doi:10.1063/1.5017033.

[16] Boswell, R. W., K. Takahashi, C. Charles, and I. D. Kaganovich (2015), Non-local electron energy probability function in a plasma expanding along a magnetic nozzlen, *Frontiers in Physics*, *3*, doi:10.3389/fphy.2015.00014.

[17] Braginskii, S. I. (1965), Transport processes in a plasma, *Reviews of plasma physics, 1*.

[18] Brown, Z. A., and B. A. Jorns (2019), Spatial evolution of small wavelength fluctuations in a Hall Thruster, *Physics of Plasmas*, *26*(11), 113,504, doi:10.1063/1.5116708.

[19] Cannat, F., T. Lafleur, J. Jarrige, P. Chabert, P. Elias, and D. Packan (2015), Optimization of a coaxial electron cyclotron resonance plasma thruster with an analytical model, *Phys. Plasmas*, *22*(053503), doi:10.1063/1.3442736doi.org/10.1063/1.4920966.

[20] Caponi, M. Z., and N. A. Krall (1975), Anomalous heat conduction along the field lines for turbulently heated plasmas, *Phys. Fluids*, *18*(6), 699–709, doi:10.1063/1.861194.

[21] Carter, T. A., H. Ji, F. Trintchouk, M. Yamada, and R. M. Kulsrud (2002), Measurement of lower-hybrid drift turbulence in a reconnecting current sheet, *Phys. Rev. Lett.*, *88*(1), doi:10.1103/PhysRevLett.88.015001.

[22] Carter, T. A., M. Yamada, H. Ji, R. M. Kulsrud, and F. Trintchouk (2002), Experimental study of lower-hybrid drift turbulence in a reconnecting current sheet, *Phys. Plasmas*, *9*(8), 3272, doi:10.1063/1.1494433.

[23] Cavalier, J., N. Lemoine, G. Bonhomme, S. Tsikata, C. Honoré, D. Grésillon, C. Honor, and D. Gr Esillon (2013), Hall thruster plasma fluctuations identified as the electron drift instability: Modeling and fitting on experimental data, *Phys. Plasmas*, *20*(082107), doi:10.1063/1.4817743.

[24] Chapman, S., and T. Cowling (1970), *The Mathematical Theory of Non-Uniform Gases*, Cambridge University Press, London, doi:10.1016/0021-9169(71)90189-9.

[25] Charles, C., K. Takahashi, and R. W. Boswell (2012), Axial force imparted by a conical radiofrequency magneto-plasma thruster, *Appl. Phys. Lett.*, *100*(11), 113,504, doi:10.1063/1.3694281.

[26] Chen, F. (1984), *Introduction to Plasma Physics and Controlled Fusion*, 2 ed., Plenum Press, New York, NY, doi:10.1007/978-3-319-22309-4.

[27] Chen, F. F., J. D. Evans, and G. R. Tynan (2015), Helicon discharges and sources: a review, doi:10.1088/0963-0252/24/1/014001.

[28] Collard, T. A., and B. A. Jorns (2019), Magnetic nozzle efficiency in a low power inductive plasma source, *Plasma Sources Sci. Technol.*, *28*(105019), doi:10.1088/1361-6595/ab2d7d.

[29] Collard, T. A., M. P. Byrne, S. T. Hepner, C. J. Durot, and B. A. Jorns (2017), Investigation of detachment in a miniature magnetic nozzle source, in *35th International Electric Propulsion Conference*, IEPC-2017-335, Atlanta, Georgia, USA.

[30] Cook, J. W. S., S. C. Chapman, R. O. Dendy, and C. S. Brady (2011), Self-consistent kinetic simulations of lower hybrid drift instability resulting in electron current driven by fusion products in tokamak plasmas, *Plasma Phys. Control. Fusion*, *53*(065006), doi:10.1088/0741-3335/53/6/065006.

[31] Correyero, S. (2019), Plasma beam characterization along the magnetic nozzle of an ECR thruster, *Plasma Sources Sci. Technol.*, *28*(095004).

[32] Correyero, S., J. Jarrige, and D. Packan (2017), Measurement of anisotropic plasma properties along the magnetic nozzle expansion of an electron cyclotron resonance thruster, in *35th International Electric Propulsion Conference*, IEPC-2017-437.

[33] Daughton, W., G. Lapenta, and P. Ricci (2004), Nonlinear evolution of the lower-hybrid drift instability in a current sheet, *Phys. Rev. Lett.*, *93*(10), doi:10.1103/PhysRevLett.93.105004.

[34] Davidson, R., and N. Krall (1977), Anomalous transport in high-temperature plasmas with applications to solenoidal fusion systems, *Nucl. Fusion*, *17*.

[35] Davidson, R. C., and N. T. Gladd (1975), Anomalous transport properties associated with the lower-hybrid-drift instability, *Phys. Fluids*, *18*(1327), doi:10.1063/1.861021.

[36] Doyle, S. J., A. Bennet, D. Tsifakis, J. P. Dedrick, R. W. Boswell, and C. Charles (2020), Characterization and control of an ion-acoustic plasma instability downstream of a diverging magnetic nozzle, *Front. Phys.*, *8*(24), doi: 10.3389/fphy.2020.00024.

[37] Druyvesteyn, M. J., and F. M. Penning (1940), The mechanism of electrical discharges in gases of low pressure, *Reviews of Modern Physics*, *12*(2).

[38] Ducrocq, A., J. C. Adam, A. Héron, and G. Laval (2006), High-frequency electron drift instability in the cross-field configuration of Hall thrusters, *Phys. Plasmas*, *13*(102111), doi:10.1063/1.2359718.

[39] Dum, C. T. (1978), Anomalous electron transport equations for ion sound and related turbulent spectra, *Phys. Fluids*, *21*(6), 956–969, doi:10.1063/1.862339.

[40] Emoto, K., K. Takahashi, and Y. Takao (2021), Numerical investigation of internal plasma currents in a magnetic nozzle, *Phys. Plasmas*, *28*(93506), doi: 10.1063/5.0053336.

[41] Foust, J. (2021), Phase Four launches first plasma propulsion systems.

[42] Frias, W., A. I. Smolyakov, I. D. Kaganovich, and Y. Raitses (2012), Long wavelength gradient drift instability in Hall plasma devices. I. Fluid theory, *Physics of Plasmas II. Applications Physics of Plasmas Journal of Applied Physics*, *19*(8), 72,112–52,108, doi:10.1063/1.4736997.

[43] Fridman, A. (1964), On the Phenomena of the Critical Magnetic Field and Anomalous Diffusion in Weakly Ionized Plasma, *Sov. Phys. Doklady*, *9*(1).

[44] Fried, B. D., and S. D. Conte (1961), *The Plasma Dispersion Function*, Academic Press, New York, doi:10.1016/C2013-0-12176-9.

[45] Fruchtman, A., K. Takahashi, and C. Charles (2012), A magnetic nozzle calculation of the force on a plasma, *Phys. Plasmas*, *19*, 33,507, doi:10.1063/1.3691650.

[46] Geller, R. (1996), *Electron Cyclotron Resonance Ion Sources and ECR Plasmas*, London.

[47] Georgin, M. P. (2020), Ionization instability of the hollow cathode plume, Ph.D. thesis, University of Michigan.

[48] Georgin, M. P., B. A. Jorns, and A. D. Gallimore (2019), Correlation of ion acoustic turbulence with self-organization in a low-temperature plasma, *Phys. Plasmas*, *26*(82308), doi:10.1063/1.5111552.

[49] Giambusso, M. (2018), Investigation of High Frequency Instabilities in the Plume of the VX-200 Magnetic Nozzle, Ph.D. thesis, University of Houston.

[50] Goebel, D. M., and I. Katz (2008), *Fundamentals of Electric Propulsion: Ion and Hall Thrusters.*

[51] Hara, K., M. J. Sekerak, I. D. Boyd, and A. D. Gallimore (2014), Perturbation analysis of ionization oscillations in Hall effect thrusters, *Phys. Plasmas*, *21*(12), doi:10.1063/1.4903843.

[52] Hepner, S., B. Wachs, and B. Jorns (2020), Wave-driven non-classical electron transport in a low temperature magnetically expanding plasma, *Appl. Phys. Lett*, *116*(263502), doi:10.1063/5.0012668.

[53] Hepner, S. T., E. Tang, E. T. Dale, and B. A. Jorns (2021), Rotational Waves in the Plume of an Externally-Mounted Hall Thruster Cathode, *AIAA Journal*, pp. 1–5, doi:10.2514/1.J060578.

[54] Hirose, A., and I. Alexeff (1972), Electrostatic instabilities driven by currents perpendicular to an external magnetic field, *Nucl. Fusion*, *12*, 315–323.

[55] Hoh, F. C. (1963), Instability of penning-type discharges, *Physics of Fluids*, *6*(8), 1184–1191, doi:10.1063/1.1706878.

[56] Hooper, E. B. (1993), Plasma detachment from a magnetic nozzle, *J Propul Power*, *9*(5), doi:10.2514/3.23686.

[57] Huang, F., Y. Chen, H.-O. Peng, J.-G. Zheng, G.-F. Shi, Z.-Q. Hu, and M. Y. Yu (2009), Lower hybrid drift instability in a neutral sheet with O + ions, *Phys. Rev. Lett.*, *80*(056401), doi:10.1103/PhysRevE.80.056401.

[58] Huba, J. D., N. T. Gladd, and K. Papadopoulos (1977), The lower-hybrid-drift instability as a source of anomalous resistivity for magnetic field line reconnection, *Geophysical Research Letters*, *4*(3), 125–128, doi: 10.1029/GL004i003p00125.

[59] Jahn, R. (1968), *Physics of Electric Propulsion*, McGraw-Hill, New York.

[60] Jorns, B. A., and R. R. Hofer (2014), Plasma oscillations in a 6-kW magnetically shielded Hall thruster, *Phys. Plasmas*, *21*(5), doi:10.1063/1.4879819.

[61] Jorns, B. A., I. G. Mikellides, and D. M. Goebel (2014), Ion acoustic turbulence in a 100-A LaB6 hollow cathode, *Phys. Rev. E.*, *90*(6), 1–10, doi: 10.1103/PhysRevE.90.063106.

[62] Jorns, B. A., S. E. Cusson, Z. Brown, and E. Dale (2020), Non-classical electron transport in the cathode plume of a Hall effect thruster, *Physics of Plasmas*, *27*(2), 022,311, doi:10.1063/1.5130680.

[63] Kim, J. Y., K. S. Chung, S. Kim, J. H. Ryu, K. J. Chung, and Y. S. Hwang (2018), Thermodynamics of a magnetically expanding plasma with isothermally behaving confined electrons, *New J. Phys.*, *20*(063033), doi:10.1088/1367-2630/aac877.

[64] Kim, J. Y., G. Go, Y. S. Hwang, and K.-J. Chung (2021), Dependence of the polytropic index of plasma on magnetic field, *New J. Phys.*, *23*(052001), doi: 10.1088/1367-2630/abfab1.

[65] Koo, B.-W., N. Hershkowitz, and M. Sarfaty (1999), Langmuir probe in low temperature, magnetized plasmas: Theory and experimental verification, *J. Appl. Phys.*, *86*(1999), 1213, doi:10.1063/1.370873.

[66] Kosmahl, H. G., D. B. Miller, and G. W. Bethke (1967), Plasma acceleration with microwaves near cyclotron resonance, *J. Appl. Phys.*, *38*(4576), doi: 10.1063/1.1709188.

[67] Krall, N. A., and P. C. Liewer (1971), Low-frequency instabilities in magnetic pulses, *Phys. Rev. Lett.*, *4*(5).

[68] Krall, N. A., and M. N. Rosenbluth (1962), Trapping instabilities in a slightly inhomogeneous plasma, *Phys. Fluids*, *5*, 1435, doi:10.1063/1.1706542.

[69] Lafleur, T. (2014), Helicon plasma thruster discharge model, *Phys. Plasmas*, *21*(043507), doi:10.1063/1.4972269.

[70] Lampe, M. (1972), Theory and simulation of the beam cyclotron instability, *Physics of Fluids*, *15*(4), doi:10.1063/1.1693961.

[71] Langmuir, I., and H. M. Mott-Smith (1924), Langmuir probe technique, *Gen. Elec. Rev*, *27*, 449.

[72] Lieberman, M. A., and A. J. Jichtenberg (2005), *Principles of Plasma Discharges and Materials Processing.*

[73] Light, M., F. F. Chen, and P. L. Colestock (2001), Low frequency electrostatic instability in a helicon plasma, *Phys. Plasmas*, *8*(10), doi:10.1063/1.1403415.

[74] Ling, J., M. D. West, T. Lafleur, C. Charles, and R. W. Boswell (2010), Thrust measurements in a low-magnetic field high-density mode in the helicon double layer thruster, *Journal of Physics D: Applied Physics*, *43*(30), 305,203, doi: 10.1088/0022-3727/43/30/305203.

[75] Little, J., and E. Choueiri (2016), Electron cooling in a magnetically expanding plasma, *Phys. Rev. Lett.*, *117*(225003).

[76] Little, J. M., and E. Y. Choueiri (2013), Thrust and efficiency model for electron-driven magnetic nozzles, *Phys. Plasmas*, *20*, 103,501, doi: 10.1063/1.4824613.

[77] Little, J. M., and E. Y. Choueiri (2019), Electron demagnetization in a magnetically expanding plasma, *Phys. Rev. Lett.*, *123*, 145,001, doi: 10.1103/PhysRevLett.123.145001.

[78] Litvinov, I. I. (1971), Stationary efflux into a vacuum by a dual-temperature fully ionized plasma, *J. Appl. Mech. Tech. Phys.*, *12*(6), 793–802.

[79] Lobbia, R. B., and B. E. Beal (2017), Recommended practice for use of Langmuir probes in electric propulsion testing, *J Propul Power*, *33*(3), 566–581, doi:10.2514/1.B35531.

[80] Longmier, B. W., et al. (2014), Improved efficiency and throttling range of the VX-200 magnetoplasma thruster, *J. Propuls. Power*, *30*(1), 123–132, doi:10.2514/1.B34801.

[81] Mcdonald, M. S., and A. D. Gallimore (2011), Rotating spoke instabilities in Hall thrusters, *IEEE T Plasma Sci.*, *39*(11), 2952–2953.

[82] Mcdonald, M. S., and A. D. Gallimore (2011), Parametric Investigation of the Rotating Spoke Instability in Hall Thrusters, in *32nd International Electric Propulsion Conference*, IEPC-2011-242, Wiesbaden, Germany.

[83] Merino, M., and E. Ahedo (2013), Influence of electron and ion thermodynamics on the magnetic nozzle plasma expansion, in *33rd International Electric Propulsion Conference*, IEPC-2013-247, Washington D.C.

[84] Merino, M., and E. Ahedo (2015), Influence of electron and ion thermodynamics on the magnetic nozzle plasma expansion, *IEEE Transactions on Plasma Science*, *43*(1), 244–251, doi:10.1109/TPS.2014.2316020.

[85] Merino, M., and E. Ahedo (2016), Fully magnetized plasma flow in a magnetic nozzle, *Phys. Plasmas*, *23*, 42, doi:10.1063/1.4941975.

[86] Merino, M., F. Cichocki, E. Ahedo, and J. Mauriño (2018), Kinetic electron model for plasma thruster plumes, *Plasma Sources Sci. Technol*, *27*(035013), doi:10.1088/1361-6595/aab3a1.

[87] Migliuolo, S. (1985), Lower hybrid waves in finite-β plasmas destabilized by electron beams, *J. Geophys. Res.*, *90*(A1), 377–385, doi:10.1029/JA090iA01p00377.

[88] Miller, D., E. Gibbons, and G. Per (1963), Cyclotron resonance propulsion system, in *Electric Propulsion Conference*, American Institute of Aeronautics and Astronautics (AIAA), Colorado Springs, CO, USA, doi:10.2514/6.1963-2.

[89] Moses, R. W., R. A. Gerwin, and K. F. Schoenberg (1992), Resistive plasma detachment in nozzle based coaxial thrusters, in *Proc. 9th Symp. Space Nucl. Power Syst. AIP Conf.*, vol. 246, pp. 1293–1303.

[90] Nakamura, T. K. M., T. Umeda, R. Nakamura, H. S. Fu, and M. Oka (2019), Disturbance of the front region of magnetic reconnection outflow jets due to the lower-hybrid drift instability, *Phys. Rev. Lett.*, *123*(235101), doi:10.1103/PhysRevLett.123.235101.

[91] Olsen, C. S. (2013), Experimental Characterization of Plasma Detachment from Magnetic Nozzles, Ph.D. thesis, Rice University.

[92] Olsen, C. S., et al. (2015), Investigation of plasma detachment from a magnetic nozzle in the plume of the VX-200 magnetoplasma thruster, *IEEE T Plasma Sci.*, *43*(1), doi:10.1109/TPS.2014.2321257.

[93] Packan, D., et al. (2019), H2020 MINOTOR: Magnetic nozzle electron cyclotron resonance thruster, in *International Electric Propulsion Conference*, pp. IEPC–2019–875.

[94] Polzin, K., C. Hill, P. Turchi, R. Burton, S. Messer, R. Lovberg, and A. Hallock (), Recommended practice for use of inductive magnetic field probes in electric propulsion testing, *J. Propul. Power.*, *33*(3), doi:10.2514/1.B35406.

[95] Ramos, J. J., M. Merino, E. Ahedo, J. Us, and J. Ramos (2018), Three dimensional fluid-kinetic model of a magnetically guided plasma jet, *Phys. Plasmas*, *25*, 61,206, doi:10.1063/1.5026972.

[96] Roberson, B. R., R. Winglee, and J. Prager (2011), Enhanced diamagnetic perturbations and electric currents observed downstream of the high power helicon, *Phys. Plasmas*, *18*(053505), doi:10.1063/1.3574753.

[97] Roytershteyn, V., W. Daughton, H. Karimabadi, and F. S. Mozer (2012), Influence of the lower-hybrid drift instability on magnetic reconnection in asymmetric configurations, *Phys. Rev. Lett.*, *108*(185001), doi:10.1103/PhysRevLett.108.185001.

[98] Sakawa, Y., C. Joshi, P. K. Kaw, F. F. Chen, and V. K. Jain (1993), Excitation of the Modified Simon Hoh Instability in an Electron Beam Produced Plasma, *Physics of Fluids B: Plasma Physics*, *5*(6), doi:10.1063/1.4972269.

[99] Sanchez-Villar, A., J. Zhou, E. Ahedo, and M. Merino (2021), Coupled plasma transport and electromagnetic wave simulation of an ECR thruster, *Plasma Sources Science and Technology*, doi:10.1088/1361-6595/abde20.

[100] Sheehan, J. P., et al. (2014), Temperature gradients due to adiabatic plasma expansion in a magnetic nozzle, *Plasma Sources Sci. Technol.*, *23*(4), 045,014, doi:10.1088/0963-0252/23/4/045014.

[101] Siddiqui, M. U., and C. Cretel (2018), Updated performance measurements and analysis of the phase four RF thruster, *2018 Joint Propulsion Conference*, doi:10.2514/6.2018-4817.

[102] Simon, A. (1963), Instability of a Partially Ionized Plasma in Crossed Electric and Magnetic Fields, *The Physics of Fluids II*, *61*(10), 1184–11,101, doi:10.1063/1.1706743.

[103] Smolyakov, A. I., A. Sabo, P. Yushmanov, and S. Putvinskii (2021), On quasineutral plasma flow in the magnetic nozzle, *Phys. Plasmas*, *28*(6), doi: 10.1063/5.0050226.

[104] Smolyakov, A. I., et al. (2017), Fluid theory and simulations of instabilities, turbulent transport and coherent structures in partially-magnetized plasmas of ExB discharges, *Tech. rep.*

[105] Spitzer, L., and R. Haem (1953), Transport phenomena in a completely ionized gas, *Phys. Rev.*, *89*(5), 977–981.

[106] Stangeby, P. C. (1982), Effect of bias on trapping probes and bolometers for tokamak edge diagnosis, *J. Pys. D*, *15*, 1007.

[107] Stix, T. H. (1962), *The Theory of Plasma Waves*, McGraw-Hill, New York.

[108] Swanson, D. G. (2003), Plasma Waves (2nd edition), *Plasma Physics and Controlled Fusion*, *45*(6), 1069–1069, doi:10.1088/0741-3335/45/6/701.

[109] Takahashi, K. (2021), Magnetic nozzle radiofrequency plasma thruster approaching twenty percent thruster efficiency, *Scientific Reports 11:1*, *11*(1), 1–12, doi:10.1038/s41598-021-82471-2.

[110] Takahashi, K., and A. Ando (2017), Laboratory observation of a plasma-flow-state transition from diverging to stretching a magnetic nozzle, *Phys. Rev. Lett.*, *118*(225002).

[111] Takahashi, K., C. Charles, R. Boswell, and R. Hatakeyama (2008), Radial characterization of the electron energy distribution in a helicon source terminated by a double layer, *Phys. Plasmas*, *15*(074505), doi:10.1063/1.2959137.

[112] Takahashi, K., T. Lafleur, C. Charles, P. Alexander, and R. W. Boswell (2011), Electron Diamagnetic Effect on Axial Force in an Expanding Plasma: Experiments and Theory, *Phys. Rev. Lett.*, *107*(235001), doi: 10.1103/PhysRevLett.107.235001.

[113] Takahashi, K., C. Charles, and R. W. Boswell (2013), Approaching the Theoretical Limit of Diamagnetic-Induced Momentum in a Rapidly Diverging Magnetic Nozzle, *Phys. Rev. Lett.*, *110*(195003), doi:10.1103/PhysRevLett.110.195003.

[114] Takahashi, K., A. Chiba, A. Komuro, and A. Ando (2016), Experimental identification of an azimuthal current in a magnetic nozzle of a radiofrequency plasma thruster, *Plasma Sources Science and Technology*, *25*(055011), doi: 10.1088/0963-0252/25/5/055011.

[115] Takahashi, K., C. Charles, R. Boswell, and A. Ando (2018), Adiabatic Expansion of Electron Gas in a Magnetic Nozzle, *Phys. Rev. Lett.*, *120*, doi: 10.1103/PhysRevLett.120.045001.

[116] Takahashi, K., C. Charles, R. W. Boswell, and A. Ando (2020), Thermodynamic Analogy for Electrons Interacting with a Magnetic Nozzle, *Phys. Rev. Lett.*, *125*(16), 165,001, doi:10.1103/PhysRevLett.125.165001.

[117] Tsikata, S., and T. Minea (2015), Modulated Electron Cyclotron Drift Instability in a High-Power Pulsed Magnetron Discharge, *Phys. Rev. Lett.*, *114*(185001), doi:10.1103/PhysRevLett.114.185001.

[118] Van Doorsselaere, T., N. Wardle, G. Del Zanna, K. Jansari, E. Verwichte, and V. M. Nakariakov (2011), The first measurement of the adiabatic index in the solar corona using time-dependent spectroscopy of Hinode/Eis observations, *Astrophys. J. Lett.*, *727*(L32), 4.

[119] Varhue, W., J. Burroughs, and W. Mlynko (1992), Electron cyclotron resonance plasma etching of photoresist at cryogenic temperatures, *J. Appl. Phys.*, *72*, 3050, doi:10.1063/1.351462.

[120] Vialis, T., and J. Jarrige (2018), Direct thrust measurement of an electron cyclotron resonance plasma thruster, *J Propul Power*, *34*(5), doi:10.2514/1.B37036.

[121] Wachs, B., and B. Jorns (2018), Effect of background pressure on ion dynamics in an electron cyclotron resonance thruster, in *2018 Joint Propulsion Conference*, Cincinnati, doi:10.2514/6.2018-4585.

[122] Wachs, B., and B. Jorns (2020), Background pressure effects on ion dynamics in a low-power magnetic nozzle thruster, *Plasma Sources Sci. Technol.*, *29*(045002), 45,002, doi:10.1088/1361-6595/ab74b6.

[123] Watson, G. N. (1922), *A treatise on the theory of Bessel functions*, Cambridge University Press.

[124] West, M. D., C. Charles, and R. W. Boswell (2007), Testing a helicon double layer thruster immersed in a space-simulation chamber, *J. Propul. Power*, *24*(1), doi:10.2514/1.31414.

[125] Winglee, R., T. Ziemba, L. Giersch, J. Prager, J. Carscadden, and B. R. Roberson (2007), Simulation and laboratory validation of magnetic nozzle effects for the high power helicon thruster, *Phys. Plasmas*, *14*, 63,501, doi:10.1063/1.2734184.

[126] Zhang, Y., C. Charles, and R. Boswell (2016), Measurement of bi-directional ion acceleration along a convergent-divergent magnetic nozzle, *Appl. Phys. Lett.*, *108*(10), 104,101, doi:10.1063/1.4943583.

[127] Zhang, Y., C. Charles, and R. Boswell (2016), Thermodynamic Study on Plasma Expansion along a Divergent Magnetic Field, *Phys. Rev. Lett.*, *116*(2), 025,001, doi:10.1103/PhysRevLett.116.025001.